Ingeborg Nævra Prestholdt

Strain mapping based on scanning (precession) electron diffraction of heterostructured semiconductor nanowires: set-up and analysis

Master's thesis in Nanotechnology
Supervisor: Antonius T. J. van Helvoort
Co-supervisor: Dipanwita Chatterjee
July 2021

Master's thesis

NTNU
Norwegian University of Science and Technology
Faculty of Natural Sciences
Department of Physics

NTNU
Norwegian University of
Science and Technology

Ingeborg Nævra Prestholdt

Strain mapping based on scanning (precession) electron diffraction of heterostructured semiconductor nanowires: set-up and analysis

Master's thesis in Nanotechnology
Supervisor: Antonius T. J. van Helvoort
Co-supervisor: Dipanwita Chatterjee
July 2021

Norwegian University of Science and Technology
Faculty of Natural Sciences
Department of Physics

NTNU
Norwegian University of
Science and Technology

Abstract

Strain is an important property for the mechanical, electrical and optical properties of materials. As electronic devices constantly are getting smaller and more complex, and strain at the nm-scale becomes a part of the design, strain becomes increasingly important. However, for strain analysis at such small scales it is necessary to have techniques with sufficiently high spatial resolution. Strain can be measured in multiple ways, but for high resolution strain mapping, transmission electron microscopy (TEM) based techniques are most commonly used. For desired strain analysis with high spatial resolution and potentially large area coverage, scanning (precession) electron diffraction (S(P)ED) is one of the most convenient methods. Here a stack of diffraction patterns (DPs) is collected by scanning across an electron transparent thin specimen, using a nm-sized electron beam probe. The resulting four dimensional data set can be analysed for strain using automatic strain mapping routines, e.g. ones available from open-source libraries. This gives the possibility to automatically analyse strain over larger areas. Precessing the beam gives more stable and kinematic-like patterns that could give better strain analysis results. Advances in electron detector technologies and strain measuring routines means that there is a need to investigate the importance of different experimental parameters related to the S(P)ED data collection process, in order to gain the most out of the new technologies. Here in this study, the effect of experimental set-up and data analysis is systematically studied

An example of structures in which strain can be found at the nm-scale, are heterostructured semiconductor nanowires (NWs), where strain can be used to for example tune the band gap of the material. In this thesis, strain was investigated in two GaAs NWs with an axially inserted heterostructure of GaAsSb. The NWs were initially characterised with conventional TEM, using techniques including high-resolution TEM imaging, bright-field and dark-field imaging, and selected area electron diffraction. S(P)ED data was then collected from the same NWs with varying experimental parameters such as with and without precession of the beam, two different convergence angles, two different regions on a low-index zone, two different camera lengths and two different pixel bit depths. Strain measurements from the recorded data were performed using three different strain mapping algorithms (cross-correlation, center of mass and Gaussian fitting) available in the open source Python library pyXem. It was found that SPED data collected with smaller convergence angle (to avoid DP disk overlap) and larger pixel depth (to avoid oversaturation of the data) produced the most consistent results. It was also found that data taken with a direct electron detector produced visibly better strain mapping results than data taken with old detector technology (i.e. optical imaging of the fluorescent viewing screen). The cross-correlation method was found to be the most robust and accurate method for data with lower signal-to-noise ratios. Especially the Gaussian fitting method depended on high quality patterns. Pre-processing of the data, e.g. background subtraction, can improve the strain analysis and the three strain mapping routines produced very similar results when pre-processing was done. It was found that the 3D geometry of the NW and how accurate the alignment on zone was affects the measured 2D strain projection. For the NWs analysis, strain variations in the zinc blende $[2\,\overline{1}\,\overline{1}]$ orientation could be resolved that have not been seen previously. For all three methods, bending of the NW limit the area that can be analysed. Furthermore, choice of which part is aligned on zone and the choice of reference area need to be taken with care. The best is to have a relatively large reference area with minimal variations, and both reference area and region of interest on zone. A best-practice guide for set-up for collection and data analysis of S(P)ED data is created. This study demonstrates that new detector technology and open-source data processing have the potential to do large area strain analysis with nm-scale spatial resolution generically applicable.

Sammendrag

Tøyning er en viktig egenskap for materialers mekaniske, elektriske og optiske egenskaper. Ettersom elektroniske enheter stadig blir mindre og mer komplekse, og tøyning på nm-skalaen blir en del av designet, blir tøyning stadig viktigere. Imidlertid, for tøyningsanalyse i så små skalaer er det nødvendig å ha teknikker med tilstrekkelig høy romlig oppløsning. Tøyning kan måles på flere måter, men for tøyningskartlegging med høy oppløsning brukes oftest transmisjonselektronmikroskopi (TEM) -baserte teknikker. For ønsket tøyningsanalyse med høy romlig oppløsning og potensielt stor arealdekning er skanning (presesjon) elektrondiffraksjon (S(P)ED) en av de mest praktiske metodene. Her samles en bunke med diffraksjonsmønstre (DPs) ved å skanne over en elektrongjennomsiktig tynn prøve, ved hjelp av en nm-stor elektronstråle. Det resulterende firedimensjonale datasettet kan analyseres for tøyning ved bruk av automatiske algoritmer for tøyningskartlegging, f.eks. tilgjengelige fra åpne biblioteker. Dette gir muligheten til å automatisk analysere tøyning over større områder. Presesjon av elektronstrålen gir mer stabile og kinematisklignende mønstre som kan gi bedre resultater av tøyningsanalysen. Fremskritt innen elektrondetektorteknologier og tøyningsmålingsalgoritmer betyr at det er behov for å undersøke viktigheten av forskjellige eksperimentelle parametere relatert til S(P)ED-datainnsamlings- prosessen, for å få mest mulig ut av de nye teknologiene. I denne oppgaven undersøkes effekten av eksperimentelt oppsett og dataanalyse.

Et eksempel på strukturer med nm-skala tøyning, er heterostrukturerte halvledernanotråder. I disse kan tøyning brukes til for eksempel å variere båndgapet til materialet. I denne oppgaven ble tøyning i to GaAs nanotråder undersøkt med en aksielt innsatt heterostruktur av GaAsSb. Nanotrådene ble opprinnelig karakterisert med konvensjonell TEM, ved hjelp av teknikker som inkluderer høyoppløsnings TEM, lysfelt- og mørkfeltavbildning, og selektivt område elektrondiffraksjon. S(P)ED-data ble deretter innsamlet fra de samme nanotrådene med varierende eksperimentelle parametere; med og uten strålepresesjon, to forskjellige konvergensvinkler, to forskjellige regioner på en lavindekssone, to forskjellige kameralengder og to forskjellige pikseldybder. Tøyningsmålinger fra de registrerte dataene ble utført ved hjelp av tre forskjellige algoritmer for tøyningskartlegging (tverrkorrelasjon, massesenter og Gaussisk tilpasning) tilgjengelig i det åpne Python-biblioteket pyXem. Det ble funnet at SPED-data samlet med mindre konvergensvinkel (for å unngå diskoverlapping i diffraksjonsmønsteret) og større pikseldybde (for å unngå overmetting av dataene) ga de mest konsistente resultatene. Det ble også funnet at data tatt med en direkte elektrondetektor produserte synlig bedre resultater for tøyningskartlegging enn data tatt med en gammel detektorteknologi (dvs. optisk avbildning av den fluoriserende visningsskjermen). Tverrkorrelasjonsmetoden ble funnet å være den mest robuste og nøyaktige metoden for data med lavere signal-til-støy-forhold. Spesielt den Gaussiske tilpasningsmetoden var avhengig av mønstre med høy kvalitet. Forbehandling av dataene, som for eksempel bakgrunnssubtraksjon, kan forbedre tøyningsanalysen og de tre algoritmene ga veldig like resultater når forbehandling ble gjort. Det ble funnet at 3D-geometrien til nanotrådene og nøyaktig hvor innstillingen på sonen var, påvirket den målte 2D-tøyningsprojeksjonen. For nanotrådanalysen kunne tøyningsvariasjoner i sinkblende $[2\,\bar{1}\,\bar{1}]$ -orienteringen sees, som ikke har blitt observert tidligere. For alle tre metodene begrenser bøying av nanotråden området som kan analyseres. Videre må valg av hvilket område som er innstilt på sonen og valg av referanseområde tas med omhu. Det beste er å ha et relativt stort referanseområde med minimale variasjoner, og både referanseområde og interesseområde på sone. En veiledning for god praksis for innsamling og dataanalyse av S(P)ED-data har blitt laget. Denne oppgaven viser at ny detektorteknologi og databehandling med åpen kildekode har potensial til å gjøre store tøyningsanalyser med romlig oppløsning på nm-skala på en generelt anvendbar måte.

Preface

This is a thesis for the conclusion of my MSc in Nanotechnology at the Norwegian University for Science and Technology (NTNU), done January-June 2021. All work is done by me, including data processing, unless specifically mentioned otherwise. Parts of the theory are based on an earlier report of mine [1]. In Appendix C, an abstract for a paper to be published in the journal Symmetry partly based on the work done in this thesis.

Table of Contents

Abbreviations

1D one-dimensional
2D two-dimensional
3D three-dimensional
4D four-dimensional
AEM analytical electron microscopy
AP aperture
BF bright-field
BFP back focal plane
BLO binary large object
CBED convergent beam electron diffraction
CCD charge-coupled device
CoM center of mass
DF dark-field
DFT discrete fourier transform
DP diffraction pattern
ED electron diffraction
EDX energy-dispersive x-ray spectroscopy
EM electromagnetic
fcc face centered cubic
FFT fast fourier transform
FE finite elements
FEG field-emission gun
HAADF high-angle annular dark-field
hcp hexagonal close packed
HDF5 hierarchical data format 5
HRTEM high-resolution transmission electron microscopy
LED light emitting diode
MOSFET metal oxide semiconductor field-effect transistor
NBD nanobeam diffraction
NW nanowire
ROI region of interest
SAED selected area electron diffraction
SED scanning electron diffraction
SPED scanning precession electron diffraction
STEM scanning transmission electron microscopy
TEM transmission electron microscope
TIFF tag image file format
UHV ultra-high vacuum
VBF virtual bright-field
VDF virtual dark-field
WZ wurtzite
ZB zinc blende

1 Introduction

Our society is based in information and communication. For further growth and progress the downsizing and performance requirements of electronic components and devices are constantly being raised. The number of transistors per mm^2 in an integrated circuit chip today is approximately 173 million, giving a transistor size of about $6 \, nm^2$ [2]. This size is constantly being challenged as new fabrication methods are developed and applied. However, with the increased downscaling and complexity of the electronic devices, new challenges arise. At the nm-scale, controlling the crystal structure is important. However, also local strain, i.e. the relative changes in dimensions or lattice spacings, in nanoscale structures affects both electrical and optical properties [3] of semiconductors, as well as the band gap. This can be taken advantage of to improve the performance of microelectronic devices such as metal oxide semiconductor field-effect transistors (MOSFETs) [4]. Strain can also be used to obtain different quantum dot sizes. and thus tune the emitted wavelength [5]. When taking advantage of these properties of strain, it is important to be able to measure strain at the nm-scale. Because of the small spatial length scale, transmission electron microscopy (TEM) is a helpful tool. However, even with TEM there are multiple ways to measure strain, and how to choose the right one and optimise it for precision and accuracy needs consideration.

Two-dimensional (2D) strain can be measured in multiple ways, but for high resolution strain mapping, electron beam based methods are the most widely used, either in imaging mode or in diffraction mode. In order to measure strain from an electron microscopy image, either the atom positions have to be measured directly [6, 7] or through a Fourier transform [8] using lattice imaging. These approaches for strain analysis in TEM are most commonly used. However, in both cases, the lattice image has to be taken at very high resolution and completely on zone, which can both be complicated to obtain and only covers a relatively small area of the material at a time ($\sim 100 \, nm \times 100 \, nm$ for high resolution transmission electron microscopy, HRTEM [9]). Diffraction-based strain mapping techniques, on the other hand, do not rely on high resolution imaging, but rather on collection of diffraction patterns (DPs) with sufficient step size. In addition, the DPs do not suffer from lens distortions [10] or scan distortions that need to be corrected [11]. There are other approaches such as dark-field electron holography [12] that can analyse larger areas, but these require additional hardware (eg. bi-prisms).

When collecting many DPs over a large area, it is desirable to use an automatic data collection approach. A convenient way to do this is with scanning electron diffraction (SED). In conventional selected area electron diffraction (SAED), a larger area (hundreds of nanometers) of the specimen is illuminated with the parallel electron beam and all of this area contributes to the data gathered. The spatial resolution on the specimen by SAED approach is ca. $100 \, nm$ [10], and all data is collected manually. Another way is to use a convergent beam for diffraction (CBED) [13], which has a spatial resolution in the order of nms. Strain analysis can be accurate when features such as HOLZ lines in the diffraction discs are used. However, for this analysis dynamic simulations are needed. Even if data collection can be automated [14], the analysis proven non-trivial and the technique is not commonly used. In SED on the other hand, the electron beam is focused into a probe that only hits a very small point (0.5 - 2 nm) on the sample, and only this small area contributes to the data gathered. By scanning this probe across the sample, a stack of DPs are created (i.e. a four-dimensional (4D) data set with dimensions x, y, k_x, and k_y). The relative change in d-spacings, i.e. strain, across the scanned area can then be deduced by automatic routines which later can be analyzed using computer algorithms [15]. Thus, in theory, larger areas can be scanned and analyzed automatically, making for a more efficient characterization process.

However, electrons interact strongly with matter and the kinematic diffraction assumption is a lim-

ited description for the intensity distribution in DPs, even for thin specimens, in both conventional TEM and SED. Intensity variations due to dynamical diffraction effects complicate data interpretation, both manual and by algorithms. Kinematic-like patterns can be obtained by introducing a precession of the incident electron beam in a cone whose center is along the zone axis [16, 17]. By using precession, varying intensity effects of reflections are averaged out, and thus more stable patterns are obtained. This alternative probe illumination can be done point by point by scanning across the sample just like SED [18]. The resulting technique is called scanning precession electron diffraction (SPED), and produces a more averaged DP in each probe point. This approach is made commercially available. Comparative studies show that precession increases the quality, i.e. accuracy and precision, and robustness of the electron diffraction strain analysis [19], and should be preferred over lattice-based approaches and dark-field electron holography.

An example of structures in which strain can be used to tune the material properties are semiconductor nanowires (NWs). They have many uses, such as improving light extraction efficiency and emission wavelength coverage in light emitting diodes (LEDs) [20], lowering cost to efficiency ratios in solar cell technology [21, 22], and allowing for further miniaturisation and improved performance of MOSFETs [23]. III-V compound semiconductors in particular have a wide application in high-performance optoelectric devices owing to their high electron mobility, direct bandgap and low exciton binding energy [24]. A lot of research and progress has been made on the growth and properties of III-V compound NWs, and the effects of strain.

It possible to induce strain in a III-V compound semiconductor by replacing some of the group III atoms with atoms from a different group III. An example is GaAs, where some of the As lattice sites can be taken by Sb atoms. GaSb has a larger lattice constant ($\sim$6.095 Å) than GaAs ($\sim$5.65 Å), which means that the replacement of As atoms with Sb atoms introduces strain into the structure. This affects the band gap of the material. In direct III-V compound semiconductors, positive strain (tension) reduces the band gap, while negative strain (compression) increases the band gap [25]. Thus, the band gap of the GaAsSb insert can be tuned between that of GaAs (1.47 eV) and GaSb (0.73 eV) by adjusting the Sb concentration [26]. By introducing the Sb during growth of a segment within a GaAs NW and then discontinuing this Sb supply, a unique heterostructure can be formed, which is an important aspect if they are to be used in optoelectronic devices [27]. Going further into detail, although so far only analyzed for thin film rather than NW geometry, it turns out that the strain affects the composition-bandgap relation [28]. Using such a NW for the measurement of strain is beneficial because the structure is already electron transparent. In bulk and thin film cases, the material has to be thinned to electron transparency. This could lead to strain relaxation or artefacts introduced by the thinning process.

In order to be able to measure strain for larger areas, it is desirable to have an algorithm that can calculate the strain efficiently and accurately from the S(P)ED data. Since the strain values in such structures typically are small (typically less than 10 %, for example 4.3 % as reported in [29]), it is important that the algorithms can detect the placement and shift of DP peaks with very high precision, and that the analysis gives accurate results. In S(P)ED DPs, due to the small probe size of the electron beam, the DP peaks are recorded as disks instead of spots. This means that algorithms that can detect the position of disks of intensity in an efficient and robust manner are needed. To make the algorithm able to cope with different pattern appearances (i.e. large or small disks, noise levels and other dependencies on how data is collected), and to optimize for a given data set, the code with algorithms should be transparent and adjustable. Open-source packages, such as the Python library pyXem [30], provide strain mapping algorithms that can freely be used. Although a default set-up and example is given, new developments in pyXem and in strain mapping on SED data make exploring the opportunities for strain mapping useful to obtain an overview of

what strain mapping accuracy and precision is obtainable.

The aim of this project is to compare different S(P)ED based strain measuring routines, identify which routine is most suited and accurate for strain measurements in nm-scale semiconducting heterostructures. This also requires that the experimental illumination, specimen and collection parameters are screened. Two GaAs/GaAsSb NWs were characterised using conventional TEM, and S(P)ED data was gathered from the NWs around the heterostructure, with varying experimental parameters. Three different algorithms to extract strain, to be specific center of mass, cross correlation and Gaussian fitting, were compared. The target is finding the best practice and a guideline for the study of strain with nm-spatial resolution based on scanning electron diffraction data.

In chapter two basic theory on crystallography, diffraction, TEM, S(P)ED, strain and strain measurement routines is given. Chapter three presents experimental details of the work. The results are presented in chapter four and discussed in chapter five, and chapter six gives the conclusions. Finally, chapter seven contains suggestions for further work. In the appendix, beside background and supporting information, a tutorial code is given based on the results and conclusions of the present work. Also an abstract of a paper that will be written on the subject is included.

2 Theory[1]

2.1 Crystalline lattice structures

Unless otherwise stated, the text in this section is based on an introductory text book on solid state physics by Kittel [31]. In three dimensions there are 14 different lattice types, which are divided into 7 systems, see Table 1. In this table the structures are defined by three lattice vectors, $\boldsymbol{a_1}$, $\boldsymbol{a_2}$ and $\boldsymbol{a_3}$. The position, r_i, of a point within one of these lattice structures can be described in terms of the lattice vectors and the atomic coordinates x_i, y_i, z_i:

$$r_i = x_i\boldsymbol{a_1} + y_i\boldsymbol{a_2} + z_i\boldsymbol{a_3} \tag{2.1}$$

Table 1: The 14 lattice types in three dimensions

System	Number of lattices	Restrictions on conventional cell axes ($a_{1,2,3}$) and angles (α, β, γ)
Triclinic	1	$\|\boldsymbol{a_1}\| \neq \|\boldsymbol{a_2}\| \neq \|\boldsymbol{a_3}\|$ $\alpha \neq \beta \neq \gamma$
Monoclinic	2	$\|\boldsymbol{a_1}\| \neq \|\boldsymbol{a_2}\| \neq \|\boldsymbol{a_3}\|$ $\alpha = \gamma = 90° \neq \beta$
Orthorombic	4	$\|\boldsymbol{a_1}\| \neq \|\boldsymbol{a_2}\| \neq \|\boldsymbol{a_3}\|$ $\alpha = \beta = \gamma = 90°$
Tetragonal	2	$\|\boldsymbol{a_1}\| = \|\boldsymbol{a_2}\| \neq \|\boldsymbol{a_3}\|$ $\alpha = \beta = \gamma = 90°$
Cubic	3	$\|\boldsymbol{a_1}\| = \|\boldsymbol{a_2}\| = \|\boldsymbol{a_3}\|$ $\alpha = \beta = \gamma = 90°$
Trigonal	1	$\|\boldsymbol{a_1}\| = \|\boldsymbol{a_2}\| = \|\boldsymbol{a_3}\|$ $\alpha = \beta = \gamma < 120°, \neq 90°$
Hexagonal	1	$\|\boldsymbol{a_1}\| = \|\boldsymbol{a_2}\| \neq \|\boldsymbol{a_3}\|$ $\alpha = \beta = 90°$ $\gamma = 120°$

In this thesis nanowires (NWs) of GaAs/GaAsSb are studied. A NW is a one-dimensional (1D) structure with a high aspect ratio. Typical semiconductors nanowires are 10-200 nm in diameter and several µm long. The studied NWs are found in the hexagonal and the cubic systems. The unit cell of the cubic lattice structure with the lattice vectors can be seen in Figure 2.1(a). In this system, the lattice vectors are all of equal length, $|\boldsymbol{a_1}| = |\boldsymbol{a_2}| = |\boldsymbol{a_3}| = a$ and perpendicular to each other. The unit cell of the hexagonal lattice structure with the lattice vectors can be seen in Figure 2.1(b). In this system two lattice vectors are of equal length, $|\boldsymbol{a_1}| = |\boldsymbol{a_2}| = a$, with an angle $\gamma = 120°$ between them, while the last axis is perpendicular to the other axes and of a different length, $|\boldsymbol{a_3}| = c$.

Both the cubic and the hexagonal structure can be defined with three lattice vectors, however it is common to describe the hexagonal structure using four. This is due to the symmetry in the hexagonal structure, and makes describing the crystal orientations more convenient. The fourth lattice vector is defined as $\boldsymbol{a_4} = -(\boldsymbol{a_1} + \boldsymbol{a_2})$, and it is marked in pale blue in Figure 2.1.

---

[1]The theory of this thesis is partly based on a previous report by the author [1].
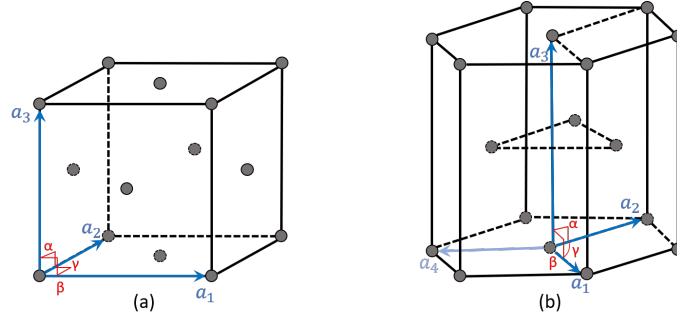
Figure 2.1: (a) Unit cell of a cubic lattice structure, specifically fcc. (b) Unit cell of a hexagonal lattice structure, specifically hcp. Angles are shown in red, lattice vectors are shown in blue. For the hexagonal lattice structure in (b), the fourth lattice vector a_4 is shown in pale blue.

The orientation of a crystal plane is described by the Miller indices. They are determined by finding the points where the plane intercepts the crystal axes of a unit cell in terms of the lattice constants, and taking the reciprocals of these numbers. The Miller indices are then the smallest integers that have the same ratio as the reciprocals. A cubic crystal structure is described by three crystal axes, and thus the indices of a plane in a cubic crystal is on the form $(h\,k\,l)$. While a single plane is denoted as $(h\,k\,l)$, a set of planes equivalent by symmetry may be denoted as $\{h\,k\,l\}$, and a specific direction in the crystal is denoted as $[h\,k\,l]$. In cubic crystals, the direction $[h\,k\,l]$ is perpendicular to a plane $(h\,k\,l)$ with the same indices. For a hexagonal crystal structure described by four crystal axes, the Miller indices of a plane are on the form $(h\,k\,i\,l)$, where $i = \overline{(h+k)}$. Using four indices instead of three is convenient when looking at planes equivalent by symmetry. For example, with three crystal axes the planes in Figure 2.2(a) are denoted $(0\,1\,0)$ and $(1\,\bar{1}\,0)$, and it is not directly obvious from their indices that they are symmetrically equivalent. However, with four crystal axes, as seen in Figure 2.2(b), the indices become $(0\,1\,\bar{1}\,0)$ and $(1\,\bar{1}\,0\,0)$, making the symmetrical relationship much clearer.
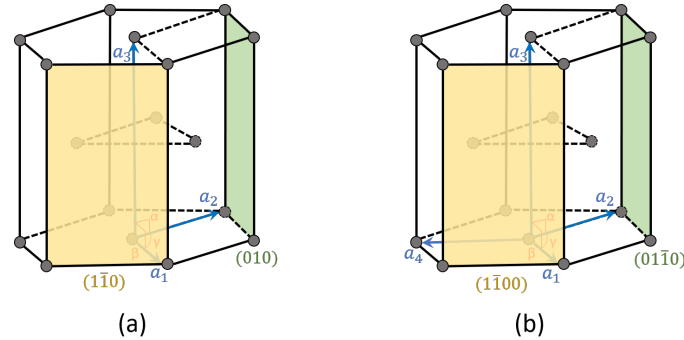
Figure 2.2: An example of how plane symmetry that is hidden when looking at (a) three Miller indices $(h\,k\,l)$ can become apparent when looking at (b) the equivalent four Miller indices $(h\,k\,i\,l)$.

The distance d_{hkl} between planes is important when studying crystal structures, and can be calculated using the Miller indices (hkl) of the plane. For a cubic structure, the distance can be calculated through the equation:

$$\frac{1}{d_{hkl}^2} = \frac{h^2 + k^2 + l^2}{a^2} \tag{2.2}$$

where a is the lattice constant.

For the hexagonal structure, the distance between the planes can be calculated as:

$$\frac{1}{d_{hkl}^2} = \frac{4}{3}\left(\frac{h^2 + hk + k^2}{a}\right) + \frac{l^2}{c^2}$$ (2.3)

where a and c are lattice constants.

The angle φ_{12} between directions and planes in a crystal can also be calculated using the Miller indices. For a cubic structure, the angle between direction 1 and 2 can be calculated through the equation:

$$cos\varphi_{12} = \frac{h_1 h_2 + k_1 k_2 + l_1 l_2}{\sqrt{h_1^2 + k_1^2 + l_1^2}\sqrt{h_2^2 + k_2^2 + l_2^2}}$$ (2.4)

while, for the hexagonal structure, the equation becomes:

$$cos\varphi_{12} = \frac{h_1 h_2 + k_1 k_2 + i_1 i_2 + \lambda l_1 l_2}{\sqrt{h_1^2 + k_1^2 + i_1^2 + \lambda^2 l_1^2}\sqrt{h_2^2 + k_2^2 + i_2^2 + \lambda^2 l_2^2}}$$ (2.5)

where $\lambda = \frac{2c^2}{3a^2}$ [32]. For correct indexing of diffraction patterns (DPs), which will be further discussed in section 2.7, both angles and d-spacings should be verified.

2.2 Crystal phases

A sub-category in both the cubic and hexagonal systems can be derived from the optimal packing of hard spheres. In the plane the most efficient way of packing spheres is the hexagonal pattern, as can be seen in Figure 2.3. Moving into the third dimension by adding another layer of spheres, there are two equivalent options of placing the second hexagonal layer. The third layer, however, has two different possible positions, either directly above the first or slightly translated with respect to both the first and the second layer. If the position of the first layer is denoted A, while the position of the second layer is denoted B, the third layer can be in position A again, or the new position C (see Figure 2.3). In the first case, a stacking in the form ABABABAB... is achieved, and the structure is called *hexagonal close packed* (hcp) (Figure 2.1(b)). In the second case, a stacking in the form ABCABCABC... is achieved, and the structure is called *face centred cubic* (fcc) (Figure 2.1(a)). Both structures have 8 tetrahedral and 4 octahedral holes per unit cell.
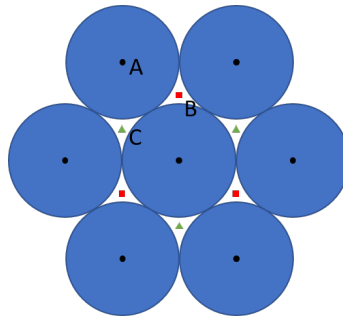
Figure 2.3: A close-packed layer of hard spheres, with center points marked as A. A second layer can be placed on top with spheres in position B (which is equivalent to position C). If the third layer atoms are placed in position A, an ABABAB... stacking sequence is created, making the structure hcp. If the third layer atoms are placed in position C, an ABCABC... stacking sequence is created, making the structure fcc.

An example of a material with an fcc structure is pure Al. There are four atoms in the fcc unit cell, and the position of the atoms are: $r_1 = (0, 0, 0)$, $r_2 = (0, 1/2, 1/2)$, $r_3 = (1/2, 0, 1/2)$, and $r_4 = (1/2, 1/2, 0)$.

III-V compound materials consists of two types of atoms, type a which is a group III atom, and type b which is a group V atom. When the III-V NWs crystallise, the b atoms either form a hcp or a fcc structure, and the a atoms occupy half of the tetrahedral holes. If the structure is fcc with half of its tetrahedral holes filled, it is called zinc-blende (ZB). This structure may also be viewed as two fcc structures, one made up of atom a and the other made up of atom b, with b displaced by $(1/4, 1/4, 1/4)$ relative to a. The position of the atoms in the ZB structure are:

a: $r_1 = (0, 0, 0)$ $r_2 = (0, 1/2, 1/2)$ $r_3 = (1/2, 0, 1/2)$ $r_4 = (1/2, 1/2, 0)$
b: $r_5 = (1/4, 1/4, 1/4)$ $r_6 = (1/4, 3/4, 3/4)$ $r_7 = (3/4, 1/4, 3/4)$ $r_8 = (3/4, 3/4, 1/4)$

A more compact way of defining the ZB structure is as belonging to space group $F\overline{4}3m$ with atoms in Wyckoff positions a and b with the coordinates $(0, 0, 0)$ and $(1/4, 1/4, 1/4)$ respectively [33]. A model of the ZB structure can be seen in Figure 2.4 (a).
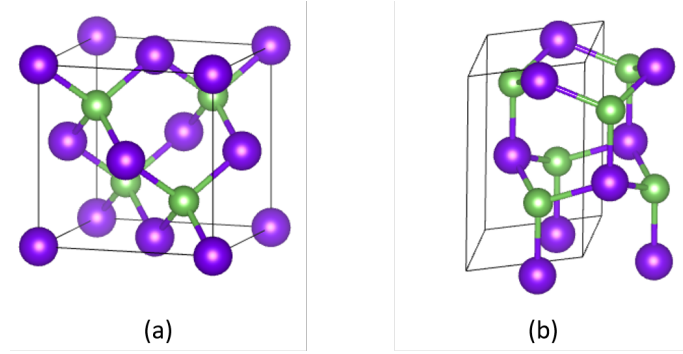
Figure 2.4: (a) Model of the atom positions in the ZB crystal structure of GaAs. (b) Model of the atom positions in the WZ crystal structure of GaAs. Ga atoms are green, As atoms are purple. The unit cells are indicated with black lines.

However, if the III-V atoms form a hcp structure with half of its tetrahedral holes filled, it is called wurtzite (WZ). Also this structure can be viewed as two structures, this time two hcp structures. The first is filled with a atoms and placed at position $(1/3, 2/3, 0)$, while the second is filled with b atoms and placed at position $(1/3, 2/3, u)$. Here u is a displacement along the [0001] direction (also known as the c-axis), and this constant is dependent on the material (for GaAs $u \approx 0.373$ [34]). Thus, the position of the atoms in the WZ unit cell are:

a: $r_1 = (1/3, 2/3, 0)$ $r_2 = (2/3, 1/3, 1/2)$
b: $r_3 = (1/3, 2/3, u)$ $r_4 = (2/3, 1/3, 1/2 + u)$

WZ can also be defined more succinctly by its space group, $P6_3mc$, with atoms in Wyckoff position b with the coordinates $(1/3, 2/3, 0)$ and $(1/3, 2/3, u)$ [33]. A model of the WZ structure can be seen in Figure 2.4 (b).

For the GaAs NWs in this thesis, $a =$ Ga and $b =$ As.

2.3   Defects

NWs typically don't contain misfit lattice defects due to lattice match with a carefully selected growth substrate and especially due to relaxation on the free surfaces. This is one of the main advantages of using NWs over thin film growth [20]. However, NWs made from III-V compounds often show unintended stacking sequences in the growth direction, randomly distributed throughout the NW, which at a high density could negatively affect the NW properties [35]. One such defect common in the ZB structure is called a twin plane. The stacking of atom layers in the ZB structure, as previously mentioned, is on the form ABCABCABC... However, sometimes a layer is misplaced during growth, causing the stacking sequence instead to become ABCACBA. The underlined A layer in this sequence then becomes the twin plane. As a consequence, the crystal structures on each side of the twin plane are rotated 120° about the growth direction, see Figure 2.5. Other forms of stacking faults may occur as well, eg. a sequence of WZ inside ZB (ABCACABC) or a sequence of ZB structure inside WZ (ABABCBC or ABABCBA). Longer sections of stacking faults can occur as well, but for more than a couple of repetitions of a different stacking sequence, it is considered to be a region with a different phase rather than a stacking fault.
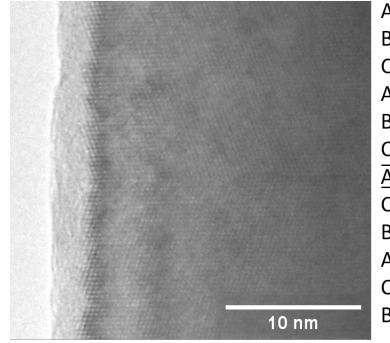
Figure 2.5: HRTEM image of a twin plane, with the stacking sequence illustrated by letters (not to scale) on the right.

2.4   Reciprocal space

Up to this point, the crystal structure has been discussed in terms of the physical position of the atoms; the real space crystal lattice. However, when talking about crystal structures it is useful to talk about the reciprocal lattice, especially when considering crystal diffraction (as will be described in section 2.5). The reciprocal lattice represents the Fourier transform of the real space lattice, and can be defined by the axis vectors $\boldsymbol{b_1}$, $\boldsymbol{b_2}$ and $\boldsymbol{b_3}$:

$$\boldsymbol{b_1} = 2\pi \frac{\boldsymbol{a_2} \times \boldsymbol{a_3}}{\boldsymbol{a_1} \cdot \boldsymbol{a_2} \times \boldsymbol{a_3}}, \quad \boldsymbol{b_2} = 2\pi \frac{\boldsymbol{a_3} \times \boldsymbol{a_1}}{\boldsymbol{a_1} \cdot \boldsymbol{a_2} \times \boldsymbol{a_3}}, \quad \boldsymbol{b_3} = 2\pi \frac{\boldsymbol{a_1} \times \boldsymbol{a_2}}{\boldsymbol{a_1} \cdot \boldsymbol{a_2} \times \boldsymbol{a_3}} \tag{2.6}$$

where $\boldsymbol{a_1}$, $\boldsymbol{a_2}$, and $\boldsymbol{a_3}$ are the axis vectors of the real space lattice, as given by equation (2.1).

All points in the reciprocal lattice corresponds to a crystal plane (h,k,l) in real space. The position of each for these points is given by the reciprocal lattice point vector, $\boldsymbol{g_{hkl}}$:

$$\boldsymbol{g_{hkl}} = h\boldsymbol{b_1} + k\boldsymbol{b_2} + l\boldsymbol{b_3} \tag{2.7}$$

where (h,k,l) are the Miller indices of a plane in real space. The reciprocal lattice point vector is perpendicular to the corresponding (h,k,l) plane, and is inversely proportional to the distance between planes in real space, d_{hkl} (see equations (2.2) and (2.3)):

$$|\boldsymbol{g}_{hkl}| = \frac{1}{d_{hkl}} \tag{2.8}$$

This vector is especially useful when interpreting DPs from a crystalline material, as will be presented in section 2.7.

2.5 Diffraction

A way to study crystal structure is through diffraction of photons, neutrons or electrons. When radiation hits a periodic structure with a spacing that is comparable or larger than the wavelength of said radiation, diffraction occurs. The wave is spread out from the small slits formed by the interatomic spacings, and interference occurs, creating a DP. Bragg's law provides a simple explanation of diffracted beams from a crystal. However, Bragg's law deals with reflections from the crystal planes rather than scattering from atoms. Suppose that the crystal planes act as semitransparent mirrors, that reflect only a fraction of the incident wave but at an equal angle (see Figure 2.6). The diffracted beams are found when the reflections from parallel atom planes interfere constructively. If the spacing between lattice planes is denoted d, the path difference of the reflected rays from parallel planes is equal to $2dsin\theta$, where θ is the angle of incidence measured from the plane. In order to then have constructive interference, this distance needs to equal an integer number of wavelength λ. Thus we get the Bragg law:

$$2dsin\theta_B = n\lambda \tag{2.9}$$

Here θ_B is called the Bragg angle, and n is an integer.
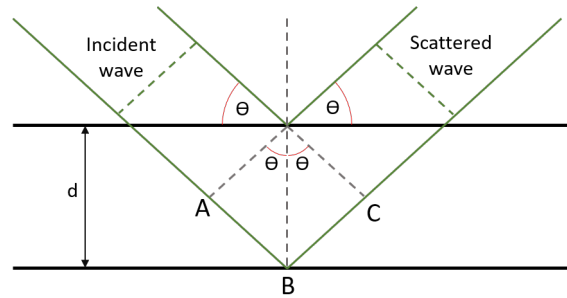
Figure 2.6: The Bragg description of diffraction. An incoming wave with wavelength λ is reflected from parallel planes with spacing d between them, resulting in a scattered wave. The path difference between the reflected waves is AB + BC.

The Bragg law can also be expressed in reciprocal space. When the Bragg condition is satisfied, we have a change in the wave vector that is

$$\boldsymbol{\Delta k} = \boldsymbol{k_{diff}} - \boldsymbol{k_{in}} = \boldsymbol{G} \tag{2.10}$$

where $\boldsymbol{G}$ is a vector in the reciprocal space of the crystal. Then, by taking the scalar product of 2.10 and the lattice vectors successively, we get the Laue equations:

$$\boldsymbol{a_1} \cdot \boldsymbol{\Delta k} = 2\pi h \;\; ; \;\;\;\; \boldsymbol{a_2} \cdot \boldsymbol{\Delta k} = 2\pi k \;\; ; \;\;\;\; \boldsymbol{a_3} \cdot \boldsymbol{\Delta k} = 2\pi l \tag{2.11}$$

Here (h,k,l) are integer numbers, and are equivalent to the Miller indices of the diffracting crystal plane. A reflection $\boldsymbol{\Delta k}$ must satisfy all three equations in order for a diffraction spot to appear.

A good way to illustrate this condition is with a construction known as the Ewald sphere. It is a sphere in reciprocal space with a radius of $1/\lambda$, where λ is the wavelength of the incoming radiation. This value is equal to the length of the k-vector of the radiation, see Figure 2.7. Only where the Ewald sphere intersects with reciprocal lattice points will the Bragg condition be satisfied. However, if this was the case, there would be no diffraction peaks if the beam was exactly aligned to a zone axis. This is not the case, and the reason for this is that a crystal has a finite physical size. Crystalline materials that have small dimensions in one or more directions will have extended reciprocal lattice points in the corresponding directions. The NWs studied in this project are thin in the direction of beam propagation, and thus the reciprocal lattice points are stretched into lines. These lines are known as reciprocal-lattice rods, or relrods for short [10]. The diffraction condition then becomes a matter of the Ewald sphere intersecting with a relrod, increasing the total number of $\boldsymbol{\Delta k}$ that fulfill the Bragg condition and may be visible in a DP. The deviation of this intersection from the center of the relrod, and thus the deviation from 2.10, can be described by a vector $\boldsymbol{s}$, known as the excitation error. The condition for diffraction then becomes:

$$\boldsymbol{\Delta k} = \boldsymbol{k_{diff}} - \boldsymbol{k_{in}} = \boldsymbol{G} + \boldsymbol{s} \tag{2.12}$$

When $\boldsymbol{s} = 0$, the Ewald sphere intersects the reciprocal lattice point at the center of a relrod. In this condition, the sample is said to be exactly on zone and a symmetric pattern can be observed.
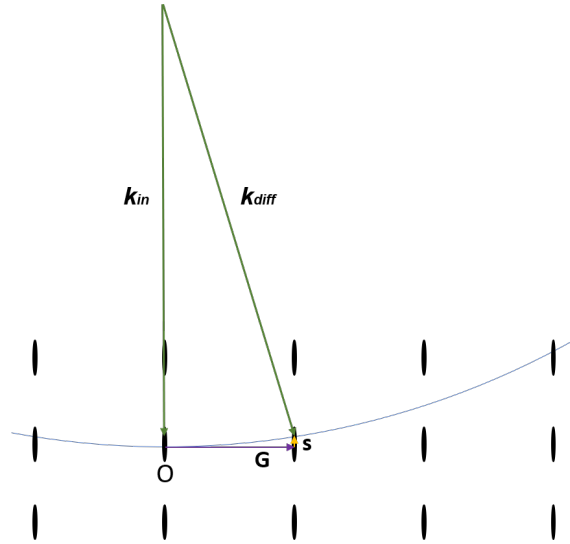
Figure 2.7: An illustration of a piece of the Ewald sphere in the reciprocal space of the crystal. Because of the size of the crystal, the lattice points appear as relrods.

2.6 TEM

Unless otherwise stated, the text in this section is based on a text book on TEM by Williams and Carter [10]. In this project a TEM is used to study the crystalline structure of GaAsSb NWs. In optical microscopy the resolution is limited by the wavelength of photons in the visible light spectrum ($\sim 500\,\text{nm}500\,\text{nm}$). The NWs have a diameter between 100-150 nm, making it impossible to study them using optical microscopy. TEM, on the other hand, makes use of electrons. The electrons are accellerated to a high kinetic energy (100 - 300 kV) in an electron gun and focused as a charged beam towards a sample. These beam electrons can achieve wavelengths that are much smaller than the distance between the atoms in the material. For example, at an acceleration voltage of 200 kV, the electron wavelength is approximately 2.5 pm. As a consequence, limited by aberration of the lenses used, the TEM can attain a very high resolution (about 2 Å at 200 kV) showing details down to an atomic scale. The resolution is limited by lens imperfections, specifically spherical aberrations. By using high energy radiation the TEM can achieve a variety of measurements, but the main principle is elastic coherent interaction, ie. diffraction (see section 2.5), which forms the basis for imaging and electron diffraction (ED). HRTEM provides imaging of the atomic structure of a sample in real space. The DP grants information on crystal structure, including orientation, lattice spacing, crystal phase of the material and strain variations. To be able to understand these measurements and how they are performed, some theory on the electron-specimen interactions is required.

2.6.1 Electron-specimen interactions

When a beam of electrons is directed towards the specimen in a TEM, a wide range of signals are generated, as shown in Figure 2.8(a). Many of these signals, such as inelastically scattered electrons, Auger electrons and characteristic X-rays, can be used in analytical electron microscopy (AEM) to give information about the chemical composition and other details about the sample. However, in TEM the most interesting signals are usually the elastically scattered electrons that do not diverge far from the incident beam direction, i.e. the electrons that are forward scattered. The TEM is built to mainly gather these electrons as they give important information about the internal structure of the specimen, and are the ones used in creating DPs and images.

Not all electrons that go through the specimen interacts with it. The probability of an electron interacting with, and scattering from, an atom is described by its scattering cross section σ_{atom}. This can be found by considering the differential scattering cross section of the atom $d\sigma/d\Omega$, which describes the angular distribution of scattering from an atom, see Figure 2.8(b). The differential scattering cross section for a single, isolated atom can be written as

$$\frac{d\sigma}{d\Omega} = \frac{1}{2\pi sin\theta}\frac{d\sigma}{d\theta} \tag{2.13}$$

The scattering cross section for a single atom, for scattering into all angles greater than θ, can then be calculated by integrating equation (2.13)

$$\sigma_{atom} = \int_{\theta}^{\pi} d\sigma = 2\pi \int_{\theta}^{\pi} \frac{d\sigma}{d\Omega} sin\theta d\theta \tag{2.14}$$

For a specimen with N number of atoms per unit volume, a total scattering cross section for the specimen can be calculated as

$$\sigma_{total} = N\sigma_{atom} \tag{2.15}$$

where $N = N_0 \rho / A$, N_0 being Avogadro's number, A being the atomic weight of the scattering atoms in the specimen and ρ being density of the specimen. The total scattering cross section for the specimen then becomes

$$\sigma_{total} = N\sigma_{atom} = \frac{N_0 \sigma_{atom} \rho}{A} \tag{2.16}$$

which is to say σ_{total} is the number of scattering events per unit distance that the electron travels through the specimen. If the specimen has thickness t, the probability of scattering from the specimen can be found by multiplying equation (2.16) by the thickness t. The scattering cross section decreases with increasing θ showing, as mentioned above, that most of the electrons are scattered at a small angle.

Another important parameter when describing the elastic electron-specimen interaction is the atomic-scattering factor $f(\theta)$. It is related to equation (2.13) by the following equation

$$|f(\theta)|^2 = \frac{d\sigma(\theta)}{d\Omega} \tag{2.17}$$

Here, $f(\theta)$ is a measure of the amplitude of a scattered electron wave, while $|f(\theta)|^2$ is proportional to the scattered intensity.
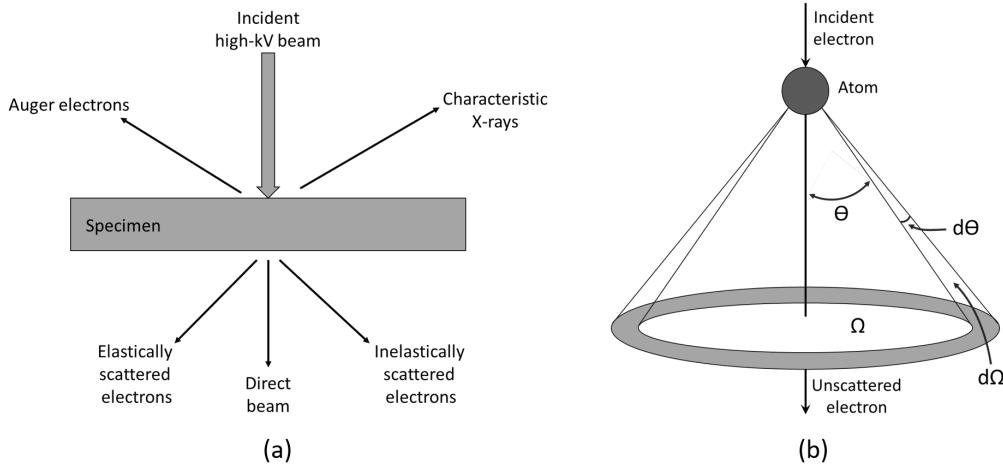
Figure 2.8: (a) When a high energy beam of electrons hits a sample it can generate a multitude of signals that can be used for various purposes. Most of these signals can be detected in different types of TEM. (b) Electron scattering by a single isolated atom. When an electron is scattered at an angle θ the solid angle is Ω. A small increase in the scattering angle $d\theta$ gives a small increase in the solid angle $d\Omega$. Figures adapted from [10].

However, $f(\theta)$ is only a measure of electron scattering from individual atoms. In order to describe electron scattering from a periodic crystal structure, the structure factor $F(\theta)$ must be introduced. $F(\theta)$ is a measurement of the amplitude that is scattered by a collection of atoms. For a unit cell of a crystal, the structure factor can be defined as a sum of $f(\theta)$ from all atoms in the unit cell, multiplied by a phase factor:

$$F(\theta) = \sum_j^{\infty} f_j e^{2\pi i (hx_j + ky_j + lz_j)} \tag{2.18}$$

Here, f_j is the atomic-scattering factor of atom j, $(x_j,\ y_j,\ z_j)$ are the atomic coordinates and $(h\,k\,l)$ are the Miller indices. This means that the scattering depends on the atomic-scattering factor corrected by a phase term related to the relative positions within the unit cell. For coherent scattering the intensity of the scattered beams follows $I_{hkl} = |F_{hkl}|^2$. This relationship is very useful when calculating extinction rules of a crystal structure, as will be shown in section 2.7.

All of these equations assume kinematic scattering, ie. that each electron is only scattered once. However, in reality, electrons in the beam and atoms in the crystal interact strongly due to Coulomb forces, causing multiple scattering events even for thin samples. This is called dynamic scattering, and this multiple interrelated scattering complicates calculations of the total scattering process a great deal. Because of dynamic scattering, the real scattering amplitude may differ from the theoretical kinematic one in an experimental setting.

2.6.2   TEM hardware

The TEM column can roughly be divided into five different components; the electron source, the condenser lens system, the objective lens system, the intermediate and projector lens system, and lastly, the detection and recording system. The schematic of a TEM column is presented in Figure 2.9. The TEM uses different lenses, deflectors, stigmators and apertures (APs) to manipulate the electron beam from its creation in the source, through the specimen and finally to the recording of the transmitted signal. The APs are basically thin plates with holes in them that can be used to prevent certain electrons from passing through. These can be used for many purposes, such as decreasing the beam intensity or selecting electrons diffracted at specific angles (ie. selecting a certain part of the real or reciprocal space along the beam path). The electromagnetic (EM) lenses can be described similarly to conventional optic lenses, but the physical principle is quite different. Whereas optical lenses have constant focusing power and thus have to be physically moved to change the bending of the beam, the EM lenses are thick and able to change strength while remaining fixed in position. The lenses are coils on which electric current is applied to produce a magnetic field in the bore along the optical axis. The strength of this magnetic field can be controlled by either increasing or decreasing the electrical current through the lens. When an electron with charge q moves through this magnetic field $\boldsymbol{B}$, it experiences a force $\boldsymbol{F}$, known as the Lorentz force, given by the equation

$$\boldsymbol{F} = q(\boldsymbol{E} + \boldsymbol{v} \times \boldsymbol{B}) \tag{2.19}$$

Here $\boldsymbol{v}$ is the velocity of the electron through the field, and $\boldsymbol{E}$ is the electric field, which is zero in the lens. Most electrons do not move exactly parallel to the magnetic field, and thus the Lorentz force causes them to move in a spiral through the lens. When the strength of the magnetic field is changed, so is the radius of the spiral trajectory. The spiral motion is usually neglected, as it is the radius of the trajectory that is the most important in terms of the focus of the lens. However this motion can cause the image to rotate depending on the chosen lens strength. A weak magnetic field will focus the incoming beams further away than a strong field.

EM lenses are not perfect, and they have aberration effects. Spherical aberration is caused by the lens behaving differently for off-axis rays or electrons of different energies, and is a limiting factor for the resolution of round EM lenses. This effect can be decreased by using highly complex multipole systems which greatly improves the resolution, so called corrected TEM. Limiting the beam by an AP so it stays close to the optical axis limits the spherical aberration, but this will also reduce the resolution and intensity. Additionally, the focusing or imaging performance can be reduced by an energy spread in the beam, either introduced in the source or by inelastic interaction. Astigmatism
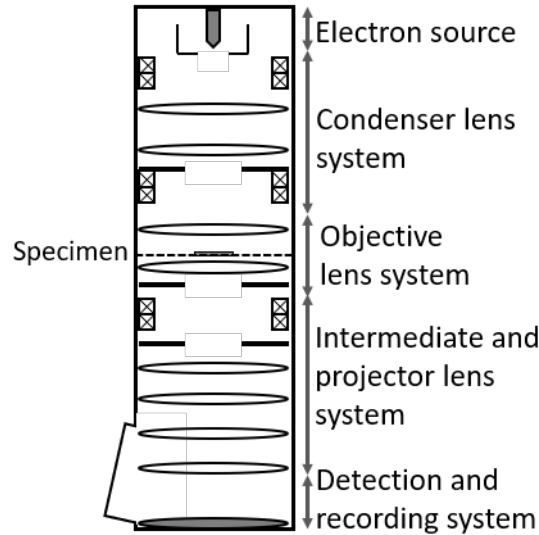
Figure 2.9: Schematic of a TEM column. The lenses are depicted as ellipses, the deflector pairs are illustrated by x-x boxes and the apertures are shown as thick lines with an opening. Figure adapted from [10]

occurs when there is a non-uniform magnetic field or there is contamination from the APs, causing distortion in the image. Astigmatism is fortunately easily corrected using stigmators, which are small octupoles that introduce a compensating field to balance the inhomogeneities causing the astigmatism. In Figure 2.9 they are visualize as sets of 4 crosses, the defector pairs, in each section of the optical column.

The electron source in the TEM can be one of two kinds: a thermionic source or a field-emission source. A thermionic electron source emits electrons when heated above a specific temperature. Most materials melt or vaporized when heated to high temperatures, so the source material must either have a very high melting temperature or emit electrons at a relatively low temperature. The thermionic source material used in modern TEMs is lanthanum hexaboride (LaB$_6$), because of its low emission temperature. A field-emission source, usually called a field-emission gun (FEG), is shaped as a sharp point and emits electrons when a large electric potential is applied between it and an anode. For field-emission to occur, the surface of the material must be free of contaminants, and thus either needs to operate in ultra-high vacuum (UHV) conditions or the tip must be heated to improve emission. The FEG source has a higher brightness, smaller virtual probe size, is more coherent and has a lower energy spread than the thermionic source. Compared to a thermoionic source a FEG achieves better lattice images and smaller probe sizes. In this project a FEG source is used. In order to achieve a beam of electrons, the chosen electron source is incorporated into a gun assembly which acts as a lens to focus the emitted electrons.

The condenser lens system controls the illumination hitting the specimen. A schematic of the ray diagram of the condenser system can be found in Figure 2.10(a). In the traditional TEM mode, the condenser lenses are used to illuminate the specimen with a parallel electron beam. The condenser system consists of two lenses, C1 and C2, as well as a condenser lense AP, a condenser stigmator and two sets of shift and tilt coils (deflectors). The C1 lens controls the spot size of the beam while the C2 lens controls the convergence of the beam at the specimen and thus controls the brightness of the beam. The condenser AP limits the angular spread of the electrons that pass through the C2 lens. A smaller condenser AP equals a more parallel electron beam on the specimen, but with

lower intensity. The first of the two deflectors is located below the electron gun to align the gun with the C1 lens, and the second deflector is located above the specimen to align the beam that comes out of the C2 lens with the specimen plane. In addition, there is a condenser stigmator in order to correct for any astigmatism introduced by the condenser lenses.
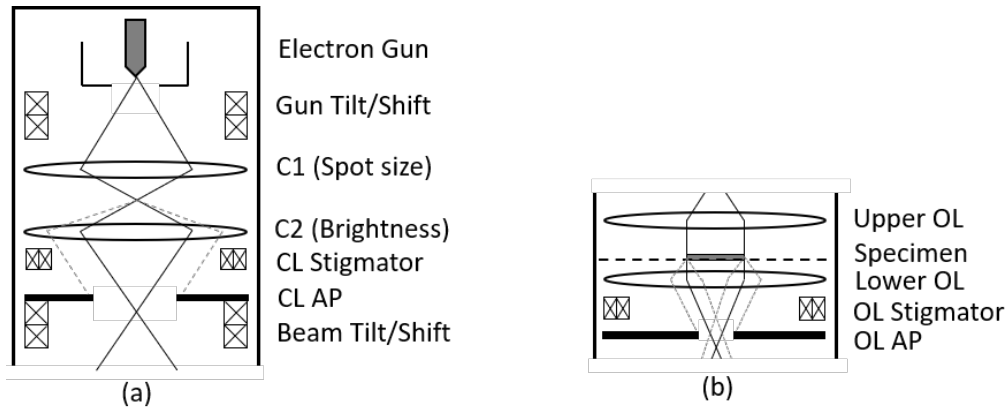
Figure 2.10: Ray diagram of (a) the condenser lens system and (b) the objective lens system. Here CL stands for condenser lens and OL stands for objective lens. Figures adapted from [10].

The objective lens system is perhaps the most important section of the TEM. It is made up of the objective lens, the specimen in its holder and the objective AP. A schematic of the ray diagram of the objective system can be seen in Figure 2.10(b). The lower objective lens is the strongest lens in the TEM, and it creates the first intermediate image of the sample. The quality of this image determines the resolution of the final image, and thus the objective lens oftentimes is the limiting factor for the resolution of the TEM. The specimen holder is a rod with a flat surface on the end which contains a hole in it where the up to 3 mm wide (in diameter) TEM specimen can be placed. The specimen sits in its holder inside the objective lens, which means that the magnetic field locally at the specimen is very high (1-2 T). The fact that the specimen sits inside the objective lens also limits the tilt range of the specimen, because the space is very limited. The objective AP is located in the back focal plane (BFP) of the objective lens, ie. in reciprocal space, and is used to select which scattered beam angles are used in the final image. This aperture is used to select a certain part of the reciprocal space and thereby form bright-field (BF) or dark-field (DF) images, see section 2.6.3.

The intermediate and projector lens system determines whether the microscope is in imaging or diffraction mode, see Figure 2.11. Both the objective and the projector lenses are held at a fixed strength, while the intermediate lenses are used to select either the BFP or the initial image plane of the objective lens as its object. The former creates a DP while the latter creates an image. By combining three lenses (objective, intermediate and projector lens) a variable magnification is obtained in both diffraction and imaging [36]. This system also contains the selected area AP which is located in the intermediate image plane of the objective lens. This AP is used in selected area electron diffraction (SAED), as it selects the area of the material that contributes to the DP. In addition, the intermediate and projector lens system includes image deflectors for the image shift and tilt, and intermediate and projector lens stigmators to correct for lens astigmatism.

Lastly, at the bottom of the TEM column there is a detection and recording system for displaying and recording the TEM data. Most TEMs have a viewing screen coated with a fluorescent material in order to be able to see the electrons. The material is usually doped in order to emit green light at around 550 nm, as this is in the middle of the visible spectrum and thus has the most optimized
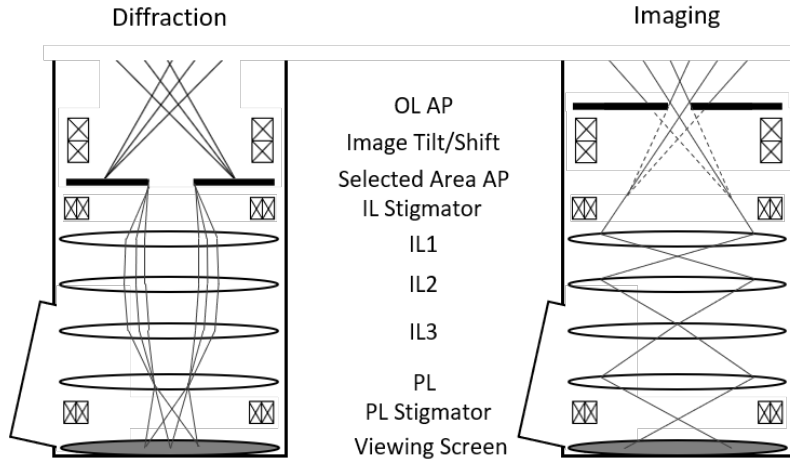
Figure 2.11: Schematic of ray diagrams for the intermediate and projection lens system. Left: TEM in SAED. Right: TEM in imaging mode. Figures adapted from [10]

visibility for human eyes. As for recording, this is done using a charge-coupled device (CCD) camera located under the viewing screen. The CCD works by having a grid of sensors that generate charge when hit by electrons. This charge is then stored and recorded as a digital signal.

2.6.3 Imaging

In normal imaging mode in the TEM, without any objective AP inserted, the image is a result of all electrons scattered by the sample. By introducing an objective AP centered in the optical axis, the image contrast can be increased as electrons scattered at large angles are excluded from the image. Using the smallest objective AP, a single diffraction peak can be selected, meaning that only regions that scatter electrons to that specific angle will be illuminated in the image. By choosing the central beam, the image that is formed is called a bright-field (BF) image (see Figure 2.12(a)). It is named as such because the regions where the electron passes through vacuum, or regions where there is little scattering, will appear bright in the image.

However, if a different diffraction peak is chosen with the objective AP, a dark-field (DF) image is obtained (see Figure 2.12(b) and (c)). Only the regions that scatter electrons to that particular peak will contribute to the image, making the rest of the image dark (hence the name). This is a very useful imaging technique for identifying regions with different crystal structures and/or orientations.

The objective AP can also select and let through several beams, which can then interfere. At high magnification and a large AP the interference pattern has fringes related to the atomic planes. This phase contrast is called HRTEM lattice imaging, and example images can be seen in section 2.7.
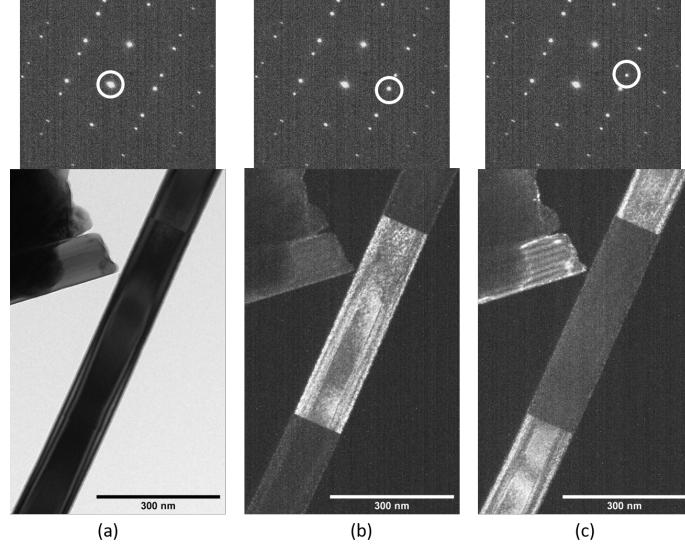
Figure 2.12: BF and DF images from a NW. The white circles indicate which peak is chosen with the objective AP. (a) BF image, (b) DF image, (c) DF image.

2.7 Diffraction pattern indexation

Indexing of DPs is based on formulas in section 2.1 regarding the relative position of the reflection. As mentioned in section 2.6.1, the scattered intensity of the diffracted electron beams is proportional to the square of the structure factor $F(\theta)$. Thus, the intensity scattered from a unit cell of the different crystal structures in the NW can be calculated by inserting the different atom positions from section 2.2 into equation (2.18).

For the ZB structure the structure factor becomes

$$F_{hkl}^{ZB} = \left\{ 1 + (-1)^{h+k} + (-1)^{h+l} + (-1)^{k+l} \right\} \left[f_a + f_b e^{\frac{\pi}{2} i (h+k+l)} \right] \tag{2.20}$$

which gives the following extinction rules:

$$|F_{hkl}^{ZB}|^2 = \begin{cases} 0, & \text{hkl mixed odd and even} \\ 16(f_a^2 + 2f_a f_b + f_b^2), & \text{h + k + l = 4n} \\ 16(f_a^2 + f_b^2), & \text{h + k + l = 2n +1} \\ 16(f_a^2 - 2f_a f_b + f_b^2), & \text{h + k + l = 4n + 2} \end{cases} \tag{2.21}$$

where n is an integer. As can be seen from (2.21), scattered peaks from planes that add up to 4n + 2, such as the $(0\,0\,2)$ plane, should have a low intensity if the scattering factor of the two atoms are similar, such as for Ga and As.

By inserting the atomic positions of the WZ crystal structure into the formula, the structure factor becomes

$$F_{hkl}^{WZ} = \left\{ e^{\frac{2\pi i}{3}(h+2k)} + e^{\frac{2\pi i}{3}(2h+k+\frac{3}{2}l)} \right\} \left[f_a + f_b e^{2\pi i u l} \right] \tag{2.22}$$

where u is a displacement along the $[0\,0\,0\,1]$ direction, as described in section 2.2. For an ideal WZ structure, $u = \frac{3}{8} = 0.735$ [34] (which is very close to the actual u for GaAs), and using this value we get the extinction rules:

$$|F_{hkl}^{WZ}|^2 = \begin{cases} 0, & \text{h} + 2\text{k} = 3\text{n, l} = \text{odd} \\ (f_a \pm f_b)^2, & \text{h} + 2\text{k} \neq 3\text{n, l} = 4\text{m} \\ (f_a^2 + f_b^2), & \text{h} + 2\text{k} \neq 3\text{n, l} = 4\text{m} + 2 \\ 3(f_a^2 \pm \sqrt{2}f_a f_b + f_b^2), & \text{h} + 2\text{k} \neq 3\text{n, l} = \text{odd} \\ 4(f_a \pm f_b)^2, & \text{h} + 2\text{k} = 3\text{n, l} = 4\text{m} \\ 4(f_a^2 + f_b^2), & \text{h} + 2\text{k} = 3\text{n, l} = 4\text{m} + 2 \end{cases} \tag{2.23}$$

where both n and m are integers. In the WZ structure, the extinction rules are more complex than for ZB. Still, the same conditions apply to this structure; if the scattering factor of the two atoms are similar, some peaks (e.g. the peak from the $(1\,0\,4)$ plane) should have low intensity. However, all of these calculations are based on the kinematic model, and this intensity difference is hard to see in actual DPs, as the electron scattering in practice likely is dynamic. For example, the intensity of the $(0\,0\,2)$ reflection in the ZB DP (Figure 2.14(c)) is relatively strong due to multiple scattering on different $[1\,1\,1]$-type planes. Similarly, the intensity of the $(0\,0\,0\,1)$ reflection in WZ (Figure 2.16(c)) which should be weak compared to the other reflections, is relatively strong in real patterns.

The extinction rules show which reflections are allowed in the DPs and which reflections are not. In order to index the allowed reflections in a given DP and determine the zone axis, the distances and angles between peaks can be measured and compared to theoretical values, calculated by using equations (2.2)-(2.5). The NWs in this thesis have a hexagonal cross section, and they have been imaged mainly through two zone axes, as shown in Figure 2.13. The first zone axis is through a face of the hexagonal cross section of the NW, and in the ZB structure this is the $[1\,\bar{1}\,0]_{ZB}$ direction.
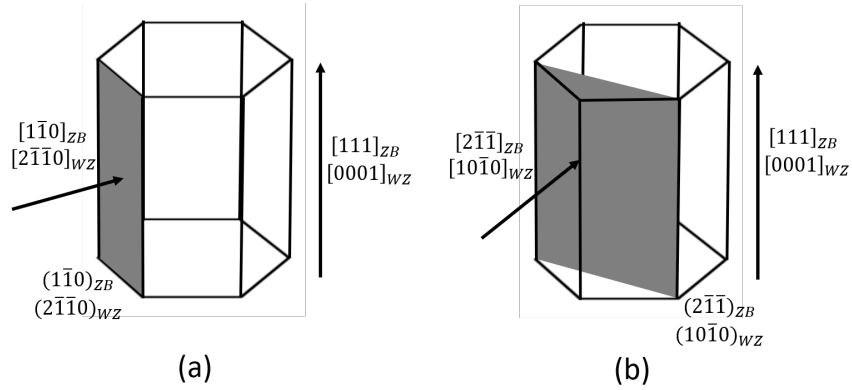
Figure 2.13: Illustrations of the two zone axes that have been used to image the NWs. The directions are indicated by arrows, and the normal planes are indicated in gray. (a) Zone axis going through the hexagonal face of the NW, corresponding to the $[1\,\bar{1}\,0]$ direction in the ZB structure and $[2\,\bar{1}\,\bar{1}\,0]$ direction in WZ. (b) Zone axis going through the hexagonal vertice of the NW, corresponding to the $[2\,\bar{1}\,\bar{1}]$ direction in the ZB structure and $[1\,0\,\bar{1}\,0]$ direction in WZ.

A model of the structure in this orientation and the corresponding indexed DP can be seen in Figure 2.14. The second zone axis is through a vertex of the hexagonal cross section of the NW, which is found by rotating the NW 30°about the growth direction $[1\,1\,1]_{ZB}$. This is the $[2\,\bar{1}\,\bar{1}]_{ZB}$

direction in the ZB structure. A model and indexation of this orientation can be found in Figure 2.15. For the WZ structure the zone axis through the hexagonal face of the NW is in the $[2\,\bar{1}\,\bar{1}\,0]_{WZ}$ direction. It can be seen in Figure 2.16, along with the DP indexation. Rotating this structure about the growth direction of the NW, $[0\,0\,0\,1]_{WZ}$, the zone axis through the hexagonal vertex aligns with the $[1\,0\,\bar{1}\,0]_{WZ}$ direction. This can be seen in Figure 2.17.
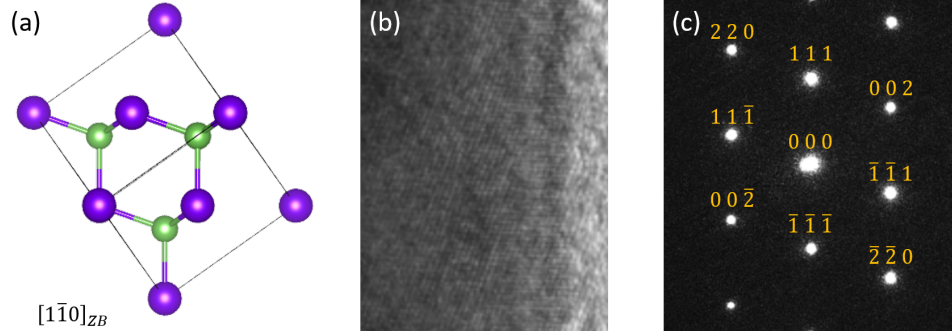
Figure 2.14: The ZB structure seen through the $[1\,\bar{1}\,0]$ zone axis for (a) a model of the ZB unit cell and (b) an HRTEM image of a GaAs NW, and (c) an indexed DP pattern for ZB in this orientation.
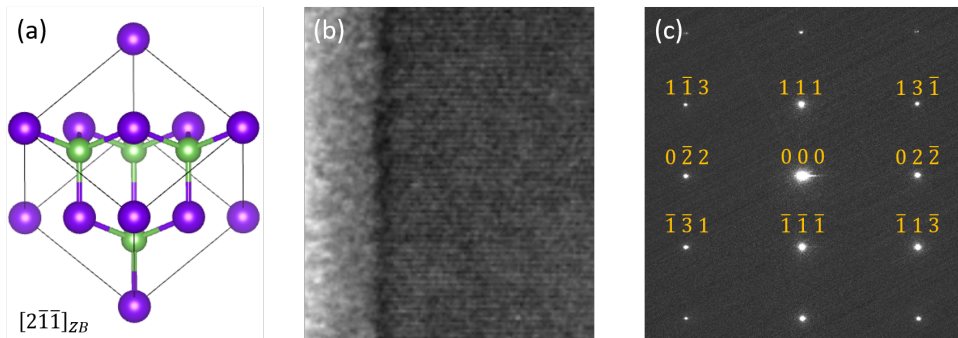
Figure 2.15: The ZB structure seen through the $[2\,\bar{1}\,\bar{1}]$ zone axis for (a) a model of the ZB unit cell and (b) an HRTEM image of a GaAs NW, and (c) an indexed DP pattern for ZB in this orientation.
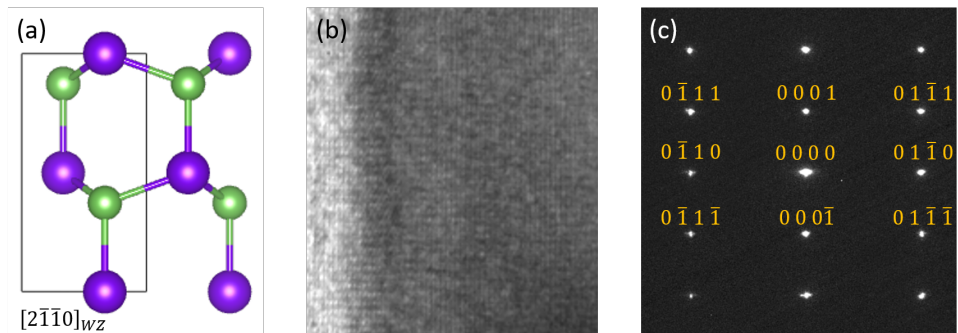
Figure 2.16: The WZ structure seen through the $[2\,\bar{1}\,\bar{1}\,0]$ zone axis for (a) a model of the WZ unit cell and (b) an HRTEM image of a GaAs NW, and (c) an indexed DP pattern for WZ in this orientation.
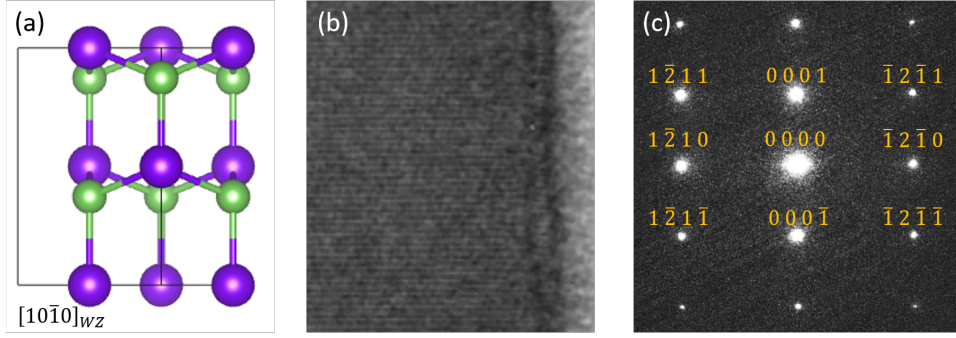
Figure 2.17: The WZ structure seen through the $[1\,0\,\bar{1}\,0]$ zone axis for (a) a model of the WZ unit cell and (b) an HRTEM image of a GaAs NW, and (c) an indexed DP pattern for WZ in this orientation.

Comparing the DPs of the $[2\,\bar{1}\,\bar{1}]_{ZB}$ orientation (Figure 2.15) and the $[1\,0\,\bar{1}\,0]_{WZ}$ orientation (Figure 2.17), they appear to look identical along these zone axes. This can be taken advantage of when measuring reflection positions and shifts over larger areas, as will be discussed in sections 2.9 and 2.10.

2.8   Scanning electron diffraction

In conventional TEM a bigger area, typically hundreds of nanometers, is illuminated by the parallel electron beam (Figure 2.18(a)). This beam can be local, ca. 100 nm in diameter, using a selected area AP in the image plane below the objective lens. The small convergence angle gives sharp spots. However in scanning electron diffraction (SED) (Figure 2.18(b)), the beam is focused into a small probe that only hits a very small point (0.5 - 2 nm) on the sample. With a static beam, this diffraction method is known as nanobeam diffraction (NBD), because of the size of the electron beam hitting the surface. This beam can then be scanned across the sample surface and produce a DP in each probe point. The DPs are collected by a detector as a 4D data set; a real space image with dimensions x and y, with an accompanying DP of dimensions k_x and k_y for each point in real space. In SED it is imperative that the beam is parallel to the optical axis in the whole scan, as incident angle variations will change the electron scattering process, and thus the DPs. This is achieved through scan coils located below the condenser lens. Since the beam is focused on one small spot, the beam is not completely parallel, it is convergent. In NBD the beam is nearly parallel with a relatively low convergence angle. Alternatively, a small probe can be formed by a beam with a large covergence angle and this is called convergent beam electron diffraction (CBED). The DP that results from this is a CBED pattern, and consists of disks rather than spots. Within these disks there can be intensity variations that are related to structural aspects such as crystal phase parameter, and specimen parameters such as specimen thickness. These patterns are more complicated and often requires dynamic treatment of the scattering. These aspects will not be discussed further here. What is relevant for this study, is that the smaller the convergence angle α, the smaller the radius of the diffraction disks.
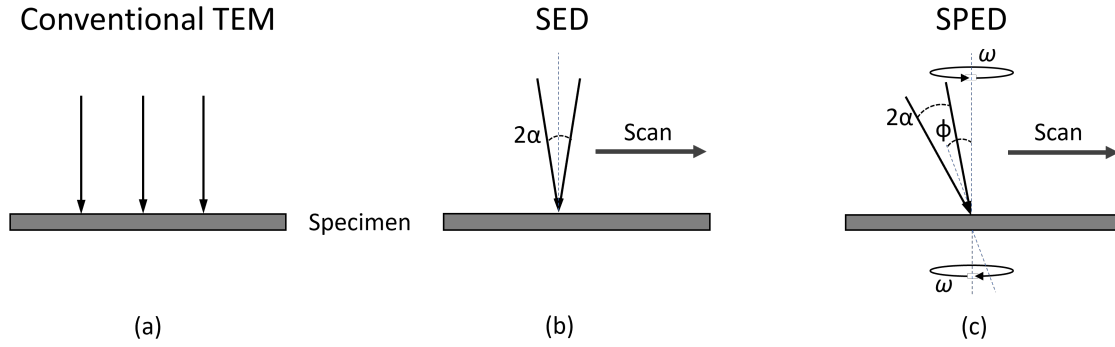
Figure 2.18: Illustration of beam illumination of a specimen in different modes. (a) In conventional TEM the specimen is illuminated by a parallel beam of electrons over a larger area. (b) In SED, the specimen is illuminated with a convergent beam with a convergence angle α, which is then scanned across the sample. (c) In SPED, the specimen is illuminated with a convergent beam which is then precessed at an angle ϕ. The beam is then scanned across the sample and precessed in each scan point.

2.8.1 Precession

An issue with SED is that electrons interact strongly with matter and the kinematic diffraction assumption is a limited first order description for the intensity distribution in DPs even for 100 nm thick GaAs NWs. In fact, less than 10 nm thickness is required in order to have a dominantly kinematic diffraction signal. Intensity variations due to dynamical diffraction effects complicate data interpretation, manual and by post-processing algorithms. By introducing precession to SED (Figure 2.18(b)), making it SPED (Figure 2.18(c)), kinematic-like DPs can be achieved for reflections with convergence angle smaller than the precession angle ϕ [17]. The convergent beam is precessed at a constant tilt angle ϕ known as precession angle, and constant angular frequency ω as the DP is recorded. As the electron beam is rocked in a hollow cone above the sample, the cone is de-rocked below the sample in order to create a stable DP, so that the intensity variations in the discs are averaged out. The intensity within each disc in the DP is thus effectively "integrated" over a variety of angles, including the Bragg condition. This can be understood by looking at the Ewald sphere. For a beam at an angle ϕ, the Ewald sphere creates a tilted circle in reciprocal space that intercept the reciprocal lattice points when the Bragg condition is fulfilled. Then, when the beam is precessed at this angle, the Ewald sphere is rotated around the optical axis and can intersect with more reciprocal lattice points (see Figure 2.19). The resulting DPs are not kinematic, but they show reduced dynamical effects compared to DPs taken without precession, as the dynamic effects are averaged out [16]. As can be seen in Figure 2.19, more of the reciprocal space is sampled (compared to Figure 2.7), and more spots are visible in the DP.
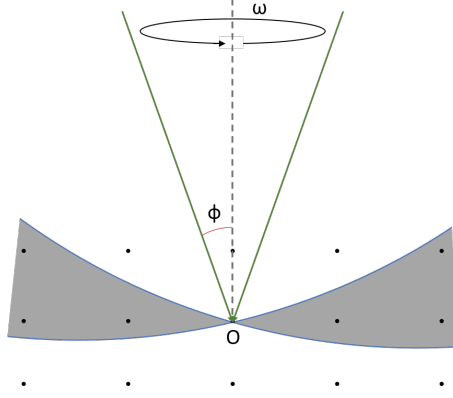
Figure 2.19: Schematic of the Ewald sphere, which intercepts certain reciprocal lattice points when the electron beam is tilted at an angle ϕ. When the beam is precessed, the Bragg condition is fulfilled for all lattice points inside the gray area. Relrods, as in Figure 2.7 are not included.

2.9 Strain

The crystal structure and its lattice parameters is important for the properties of a material. A way to change and control these parameters is to introduce strain into the structure. Strain, ε, is a dimensionless tensor, and is the measure of a fractional displacement of an atom in a crystal lattice. In three dimensions, the atomic displacement can be described by the following vector:

$$\boldsymbol{u}(\boldsymbol{r}) = \boldsymbol{r}(x, y, z) - \boldsymbol{r_0}(x, y, z) \tag{2.24}$$

where $\boldsymbol{r}(x, y, z)$ and $\boldsymbol{r_0}(x, y, z)$ are the position vector for the displaced atom and its ideal lattice position respectively, in Cartesian coordinates. The three-dimensional (3D) strain is then made up by 9 components [14]:

$$\varepsilon_{xx} = \frac{\partial u_x}{\partial x}, \quad \varepsilon_{yy} = \frac{\partial u_y}{\partial y}, \quad \varepsilon_{zz} = \frac{\partial u_z}{\partial z}$$

$$\varepsilon_{xy} = \varepsilon_{yx} = \frac{1}{2}\left(\frac{\partial u_x}{\partial y} + \frac{\partial u_y}{\partial x}\right), \quad \varepsilon_{xz} = \varepsilon_{zx} = \frac{1}{2}\left(\frac{\partial u_x}{\partial z} + \frac{\partial u_z}{\partial x}\right), \quad \varepsilon_{yz} = \varepsilon_{zy} = \frac{1}{2}\left(\frac{\partial u_y}{\partial z} + \frac{\partial u_z}{\partial y}\right) \tag{2.25}$$

The first three components are the normal strains, representing the fractional displacement length along the x, y and z direction. The other six are shear strains, which represent the shear angles measured in radians.

There are many different ways to measure the displacement of atoms, and thus strain, in a crystal lattice. Micro-Raman spectroscopy can be used to measure strain indirectly [37], as strain alters the frequencies of the Raman peaks. Diffraction peaks might broaden due to strain, as there is a variation in the d-spacings. By looking at this broadening in X-ray and neutron diffraction, average strain can be measured [38]. However, for high spatial resolution strain mapping (better than 10 nm), electron beam based methods are the most widely used, either in imaging or diffraction mode. With an electron microscopy image at atomic resolution, strain can be measured by either analysing each individual atomic position and displacement directly [6], or by analysing the Fourier

transform of the lattice [8]. These methods rely on images at very high resolution, which can both be complicated to obtain and only covers a small area of a material, as lattice images are required. Diffraction-based techniques, on the other hand, measure the spacing between atom planes in the crystal lattice from reciprocal space. These methods do not rely on high resolution imaging.

One such method, and the method utilised in this thesis, is based on nanobeam diffraction (mentioned in section 2.8). A DP is a 2D projection of the reciprocal lattice of a 3D real space crystal, with the relationship between reciprocal point vector and lattice spacing given by equation (2.7). As a consequence, the strain measured using DPs is also a 2D projection of the 3D strain. In order to calculate the strain, consider 2 orthogonal reciprocal lattice point vectors g_1 and g_2. Each vector is defined by an x and a y component perpendicular to the zone axis. They give the reciprocal point matrix G:

$$G = \begin{pmatrix} g_{1x} & g_{2x} \\ g_{1y} & g_{2y} \end{pmatrix} \tag{2.26}$$

The 2D deformation matrix (D) of the crystal region contributing to the DP can then be obtained by the G matrix of the DP and a G matrix from an unstrained reference region:

$$D = (G^T)^{-1} G_0^T - I \tag{2.27}$$

Here, T represents the matrix transpose, I is the identity matrix and G and G_0 are the reciprocal point matrices for the strained point and unstrained reference region respectively. In the case of small rotation and strain (i.e. less than 10°rotation and 4% strain [14]), the 2D strain tensor ε can be obtained by taking the symmetric part of D. The asymmetric part of D then represents the 2D rotation tensor ω:

$$\begin{aligned} \varepsilon &= \frac{1}{2}(D + D^T) = \begin{pmatrix} \varepsilon_{xx} & \varepsilon_{xy} \\ \varepsilon_{yx} & \varepsilon_{yy} \end{pmatrix} \\ \omega &= \frac{1}{2}(D - D^T) = \begin{pmatrix} cos\theta & -sin\theta \\ sin\theta & cos\theta \end{pmatrix} \end{aligned} \tag{2.28}$$

Here θ is the rotation angle of the strained lattice with respect to the unstrained lattice.

By using SED as discussed in section 2.8, a larger area can be scanned and strain can be calculated for each point with corresponding DP. Thus, we can obtain a map of the local strain in real space. In order to limit dynamical effects, it is also beneficial to utilise precession (see section 2.8.1) in combination with scanning. In fact, studies show that precession greatly improves the quality and robustness of electron diffraction strain analysis [19]. It also gives more flexibility with experimental conditions, particularly allowing for larger convergence angle and thus smaller probe size.

One of the reasons strain is such an important parameter is because of the effect strain has on the band gap of a crystalline material. For III-V semiconductor materials the the band gap becomes smaller if it is subject to positive strain (tension), while if the material is subject to a negative strain (compression), the band gap becomes larger [25]. This can be very useful for tuning the band gap in such semiconductor materials, but it is also important to avoid strain in areas where change in band gap is not desirable. Therefore, an effective method for characterisation of strain is important.

The NWs in this thesis are made up of GaAs with an insert of GaAsSb. This insert is created by exchanging some of the As atoms in a region for Sb atoms. As and Sb both belong to the same group in the periodic system, group V, and thus have very similar properties. However, the radius of the two atoms differ slightly. The atomic radius of As is $\sim 1.15\,\text{Å}$, which is smaller than that of Sb $\sim 1.45\,\text{Å}$ [39]. This has a consequence for the crystal lattice of the NW. Pure GaAs has a lattice constant of $\sim 5.65\,\text{Å}$, while pure GaSb has a lattice constant of $\sim 6.095\,\text{Å}$. When some of the As atoms are replaced with Sb atoms, the crystal lattice expands to accommodate the Sb atom. As this expansion is restricted by the GaAs in the lattice around, the resulting lattice parameters are somewhere between the one of GaAs and the one of GaSb, depending on how many As atoms have been replaced by Sb. This creates positive strain in the NW around the insert that can be measured using the method discussed in this section. Because of this known strain around the insert, the GaAsSb NWs are good model structures for testing algorithms, parameters and microscope settings for strain measurements.

2.10   S(P)ED based strain measurements

As discussed in the previous section (2.9), SPED can be used to analyse strain by measuring the reciprocal lattice point vectors and obtain the 2D displacement matrix. This is done by choosing two reflection peaks, preferably in two orthogonal directions from the center beam, recording their x and y components, and calculating the strain and rotation values for every DP in the stack. The strain values can then be plotted into 2D strain maps. These plots can show all the components of the strain and rotation; horizontal strain, vertical strain, shear strain and local rotation angle of the crystal structure.

A challenge with using this approach to find values for the strain in the crystal structure is that it requires an algorithm that can find the shift in position of the reflection peaks accurately enough for strain analysis. As mentioned in section 2.8, the beam used in SPED is a convergent beam, and the resulting DP consists of disks rather than spots. This complicates the determination of position shift, especially since the changes in peak positions due to strain typically are very small, and thus a high accuracy is needed. In this thesis, three different peak finding methods were utilised: center of mass, cross correlation and Gaussian fitting. All the methods determines the center of the reflection peak with a sub-pixel precision.

2.10.1   Center of mass method

The center of mass (CoM) of an object is defined as the average position of all weighted parts of the system, i.e. the point where sum of the relative weighted position vectors becomes zero. For physical objects, the positions are weighted according to their mass. However, the positions can be weighted based on a number of things, and for a DP peak it is based on intensity. In the DPs taken with SPED, the peaks appear as disks, and it is assumed that the center of these disks lies at the center of intensity. The equation for calculating CoM in one dimension is given as:

$$|R| = \frac{\sum_{i=0}^{n} m_i r_i}{\sum_{i=0}^{n} m_i} \tag{2.29}$$

where $|R|$ is the position of the CoM, r_i and m_i is the position and weight of each element i of the system respectively, and n is the number of elements.

In order to find the CoM of a reflection disk in the SPED DP, a square containing the peak is selected. The total sum of the intensities of each pixel is calculated, and the center of mass of each axis (x and y) is found separately, see Figure 2.20. The position of the center of mass of the same disk can then be calculated for each DP in the SPED data set, and by comparing these positions to the positions of a unstrained reference region the strain can be calculated.
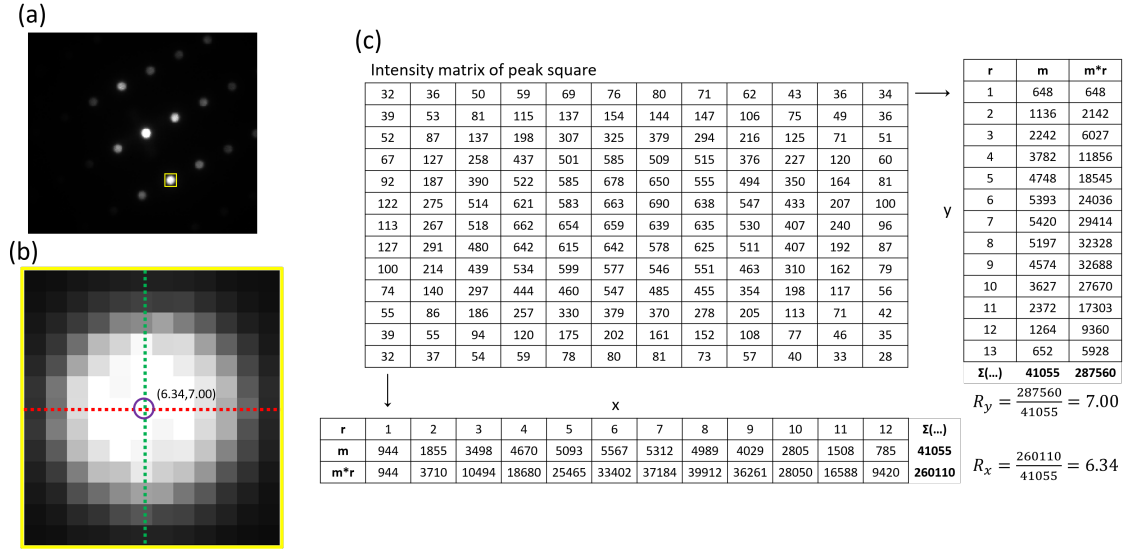
Figure 2.20: Example of the calculation of the CoM of a reflection peak. (a) The whole SPED DP with the selected square containing the peak whose position we want to determine indicated in yellow. (b) 12 x 13 square containing the reflection peak. The calculated CoM of the x-axis is indicated by a green line, the CoM of the y-axis is indicated by a red line, and the total CoM is indicated by a purple circle. (c) The calculations. Here, the intensities of the square containing the peak is given in a 12x13 matrix. The table at the bottom shows the horizontal position vector of each pixel, r_i, here given as pixel number, the summed intensity of each column of pixels, m_i, and their product, $m_i \cdot r_i$. At the end of each row is the sum of m_i and $m_i \cdot r_i$. These results are used to calculate R_x, the position of CoM along the x-axis, which is 6.34 pixels from the left-hand side. The table on the right shows the equivalent calculations for the rows of the matrix. The CoM for the image as a whole is 6.34 pixels from the left and 7.00 pixels from the top, as shown in (b).

2.10.2 Conventional cross-correlation

In signal processing, cross-correlation is used to assess how similar two different functions are [40]. This can be used in two dimensions to evaluate how similar two images are, but it can also be used to detect possible shifts between the two.

Consider two grayscale images with dimensions $m \times n$, and with pixel intensities described by the functions $f(x, y)$ and $h(x, y)$. The intensity of a pixel is a number between 0 (black) and 1 (white). To find the correlation coefficient between the two, the functions are first multiplied element-wise (i.e. pixel by pixel). The product of pixels that are white in both pictures will be 1, the product of pixels that are black in both pictures will be 0, and the product of a pixel that is black in one picture and white in the other will also be 0. All of these products are then summed into one

correlation coefficient c_{00}, as described by equation:

$$c_{00} = (f \star h) = \sum_{x=0}^{m-1} \sum_{y=0}^{n-1} f(x,y) \cdot h(x,y) \tag{2.30}$$

where $\star$ denotes the cross-correlation, and $m \times n$ are the dimensions of the images. The more dissimilar the two images are, the smaller the correlation coefficient will be. Consider now that one of the images is slightly shifted with respect to the other by a vector (i,j), so that the functions become $f(x,y)$ and $h(x+i, y+j)$. The correlation coefficient can be calculated once more, and it can be found whether this is larger, i.e. more correlated, or smaller, i.e. less correlated, than the correlation coefficient for the non-shifted images. By creating a correlation matrix with correlation coefficients for all possible shifts, the maximum correlation coefficient can be found. If the element in the center of the matrix is considered zero, then the indices of this coefficient will describe the shift of the image. In order to be able to compare the different correlation coefficients, they are often normalised as in equation 2.31 [41]:

$$c_{ij} = \frac{\sum_{x=0}^{m-1} \sum_{y=0}^{n-1} \left[f(x,y) - \bar{f} \right] \cdot \left[h(x+i, y+j) - \bar{h} \right]}{\sqrt{\sum_{x=0}^{m-1} \sum_{y=0}^{n-1} \left[f(x,y) - \bar{f} \right]^2} \cdot \sqrt{\sum_{x=0}^{m-1} \sum_{y=0}^{n-1} \left[h(x,y) - \bar{h} \right]^2}} \tag{2.31}$$

where $m \times n$ are the dimensions of the images, and $\bar{f}$ and $\bar{h}$ are the mean value of intensities of the images f and h.

The cross-correlation matrix can be computed iteratively, but this is a very computationally intense and slow process. Instead, it can be calculated by utilising the Fourier transforms of the images. The Fourier transform of the correlation matrix $C(i,j)$ becomes:

$$\mathcal{F}\{C(i,j)\}(u,v) = \mathcal{F}\{(f \star h)(i,j)\}(u,v) = \mathcal{F}^*\{f\}(u,v) \cdot \mathcal{F}\{h\}(u,v) \tag{2.32}$$

where $\mathcal{F}$ denotes the fourier transform, $*$ denotes the complex conjugate and (u,v) are the variables in Fourier space. This calculation is much simpler, as it is only a matter of multiplying the Fourier transforms of the two images together. Fast Fourier transforms (FFTs) are quite quick, and thus this is a much less time consuming and computationally intense method of calculating the cross-correlation. After this multiplication the cross-correlation matrix can be found by simply applying the inverse Fourier transform to the product. The resulting image will be the visual representation of the matrix, where the peak at maximum intensity represents the point where the two images are most alike.

Only using cross-correlation gives a pixel precision, however for this thesis sub-pixel precision is targeted. This can be achieved by upsampling the Fourier transform using a matrix multiplication implementation of a 2D discrete Fourier transform (DFT) and refining the initial peak location estimate, as discussed in [42]. This results in a precision down to a pixel divided by the upsampling factor used in the algorithm.

In order to use the cross correlation to detect the shift of a peak in a stack of SPED DPs, a square containing the peak is selected, just like the CoM method (section 2.10.1). A simulated square is then created, containing a disk with radius close to the experimental peak and center coinciding with the center of the square. The cross-correlation with sub-pixel precision is performed, and the maximum of the matrix is found by a simple locate maximum function. The position of this

maximum corresponds with the shift of the experimental diffraction peak from the center. An illustration of the method can be seen in Figure 2.21. The procedure is then performed for each DP in the stack, and compared with that of an unstrained reference region in order to calculate the strain.
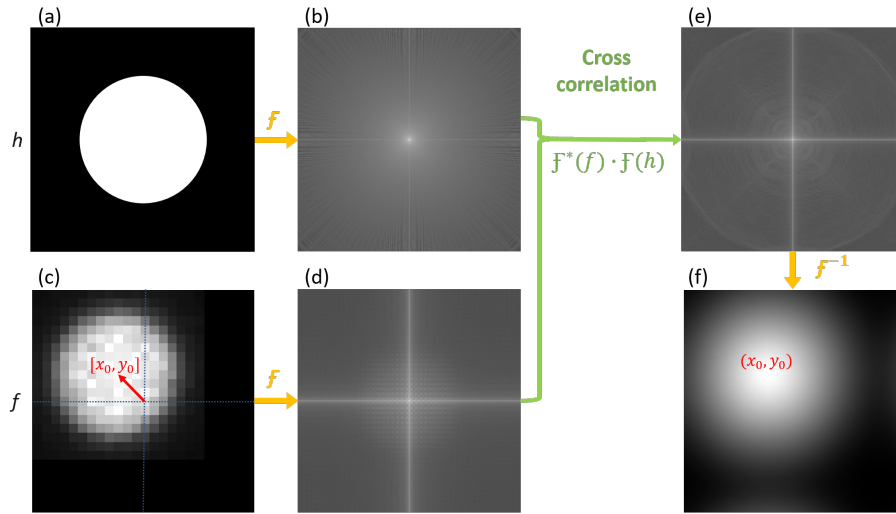
Figure 2.21: Example of use of the cross correlation method to find DP peak shift. (a) and (b) illustrates the simulated disk and its Fourier transform. (c) and (d) illustrate the experimental peak shifted by a vector $[x_0, y_0]$ (indicated by a red arrow, center of the square is indicated by blue dotted lines) and its Fourier transform. (e) is the result of the cross correlation of the two Fourier transforms, and when performing an inverse Fourier transform (f) the image shift can be found by locating the intensity maximum (indicated by red coordinates (x_0, y_0)).

2.10.3   Gaussian fitting

The Gaussian fitting method assumes, like the center of mass method, that the center of the diffraction disks lies at the center of intensity. In addition, this method assumes that the intensity profile of the disks follow a Gaussian curve.
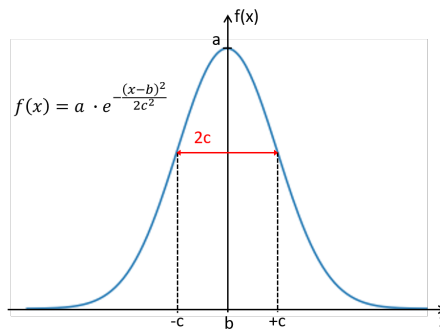
Figure 2.22: Illustration of the different parameters of the Gaussian curve.

A Gaussian curve is a symmetrical bell-shaped curve defined by the following function:

$$f(x) = a \cdot exp\left(-\frac{(x-b)^2}{2c^2}\right) \tag{2.33}$$

where a is the maximum value of the function (the peak value), the bell-curve is centered around $x = b$, and c controls the width of the peak. The parameters are illustrated in Figure 2.22. A method that is often used to fit functions to experimental data is the method of least squares. The Gaussian function is not linear, and thus a non-linear form of the method of least squares has to be utilised. The least squares method is based on the assumption that the best fitting function parameters minimises the sum of squared residuals. A residual is the difference between the actual value y_i and the function value $f(x_i)$ of a point x_i; $R_i = y_i - f(x_i)$. The problem is thus minimising the sum $\sum_i R_i^2$. The solution of a linear least squares problem is found by setting the gradient of the sum to zero and solving the resulting equations. However, non-linear least square problems cannot be solved directly, and require an iterative procedure starting from a suitable initial estimate and linearising the problem using a Taylor expansion. The problem then becomes a matter of finding suitable initial estimates for the least squares algorithm.

In order to use the Gaussian fitting method to detect the shift of a peak in a stack of SPED DPs, a square around the desired peak is selected, exactly as for the other two methods. The pixel with the highest intensity value is then found, and the intensity profiles in the x and y direction through this point are extracted. Then the initial estimates for the parameters of the Gaussian functions are estimated: a is estimated as the highest pixel intensity, b is estimated as the index of this pixel, and $2c$ is estimated to be the number of pixels with values above half the maximum, $\frac{a}{2}$. The non-linear method of least squares is then applied, and the position of the peak of the fitted Gaussian curve is returned with sub-pixel precision as the b parameter. The procedure is then performed for each DP in the stack and an unstrained reference area, and the strain can be calculated.
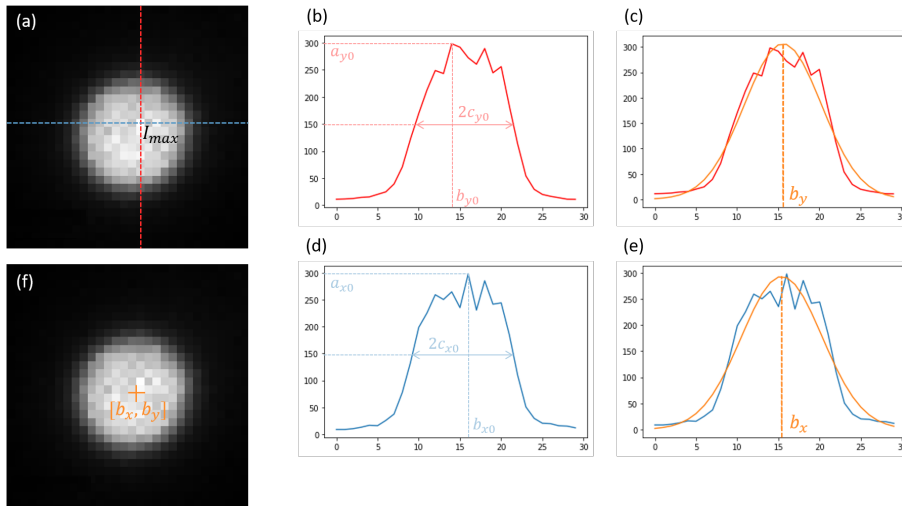
Figure 2.23: Illustration of use of the Gaussian fitting method to find the DP peak shift. (a) The pixel with the maximum intensity is found, and the profiles in the x (d) and y (b) direction is collected. Initial estimates of the parameters are found from the data, and curve fitting is performed. The b parameter of the fitted Gaussian curves in the x (e) and y (c) direction determines the position of the center of the diffraction peak, seen in (f).

3 Experimental

3.1 Material growth and substrate preparation

The NWs studied in this project are made of GaAs with axial heterostructures of GaAsSb. These were grown by Mazid Munshi on a Si(111) substrate by self-catalyzation. Further details can be found in papers by Munshi *et al.* [43] and Kauko *et al.* [44]. The TEM samples were then prepared by Tor Inge Thorsen by scraping the NWs from the substrate with a diamond scraper [45]. A TEM grid made of copper with a thin carbon film on it ($\sim 20\,$nm thick) was then humidified with isopropyl alcohol or ethanol and wiped over the scraped area. This made the loose NWs stick to the grid, with their most stable position being lying on one of the hexagonal facets. In order to be able to navigate the grid and study the same NW multiple times, a numbered TEM grid was used, as can be seen in Figure 3.1. The grid with NWs was then placed in a double tilt sample holder, with a alpha tilt limit of $\pm 35°$ and a beta tilt limit of $\pm 30°$. The sample remained in said sample holder during the whole study in order to be able to more easily locate specific NWs between microscopy sessions.
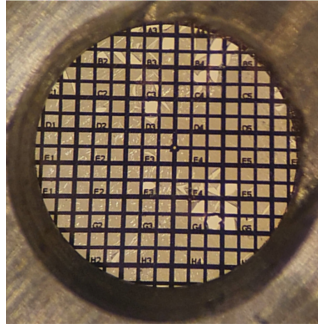
Figure 3.1: Image of the numbered $3\,$mm TEM grid used for imaging the NWs. The grid is made of copper, and covered with a thin carbon film in order to carry the NWs.

3.2 Conventional TEM

In order to characterise the structures and have comparisons for SPED data, conventional TEM was performed on the NWs. This was done on a JEOL JEM-2100F operated at a beam energy of $200\,$kV. The JEM-2100F has a tungsten FEG electron source. Images were acquired using a Gatan 2k UltraScan CCD mounted under the viewing screen, operated via the Gatan DigitalMicrograph software. The camera has a sensor of 2048x2048 $14\,\mu$m square pixels.

3.3 Scanning precession electron diffraction

The S(P)ED measurements in this project were also done with a JEOL JEM-2100F (see previous section 3.2) operated at $200\,$kV. The precession system DigiSTAR is provided by NanoMEGAS and uses their ASTAR acquisition software. The measurements with precession were taken with a precession angle of $0.5°$ in the ASTAR software (calibrated in [1] to actually be $0.582°$), and an exposure time of $10\,$ms. Due to some complications with the precession setup, certain data sets were acquired with Topspin PED Acquisition software, also provided by NanoMEGAS. The

S(P)ED data was captured using the Quantum Detectors Merlin software and a silicon MerlinEM direct electron detector with a sensor of 256x256 55 µm pixels. The size of the data sets varied in size, depending on the width of the NW and the length desired for strain measurements. The nominal probe size and step width of the S(P)ED measurements were 1 nm, but from calibration the actual step width was found to be 1.019 nm/pixel for the main NW and 1.684 nm/pixel for the second NW (Appendix A.4). All S(P)ED measurements were done in collaboration with postdoc Dipanwita Chatterjee.

3.4 Data processing and modelling

Models of crystal structures, such as Figure 2.4, have been made using the VESTA 3D visualization program [46]. Processing of the images from the conventional TEM was done using ImageJ [47]. Strain measurements, and other S(P)ED data handling was done using Python code with the open-source library pyXem v.0.13 [30]. Most processing has been done on a personal laptop with 16 GB RAM, and particularly intensive operations such as data conversion routines have been performed on a workstation with 128 GB RAM.

3.5 Experimental parameters

An objective of this thesis was to examine how different experimental parameters affect the strain mapping algorithms, and whether some parameters are more optimal than others. In order to do this, six different data sets were collected from the same NW. Their varied experimental parameters can be found in Table 2. The size of the scans were 200x1000 for scans 1-4, and 200-800 for scans 5 and 6. The length was reduced in order to make acquisition time shorter. It was found that due to bending in the NW, strain measurements were difficult for sections longer than 500 nm along the NW anyway. Other parameters, presented in section 3.3, were kept the same for all scans. The data sets from this NW were collected using the NanoMegas Scanner software.

Table 2: Varying experimental parameters for the different SPED scans taken from the main NW.

Scan	Region on zone	Pixel depth	Precession	Camera length[2]	Convergence angle[2]
Scan 1	Insert	12 bit	On	22.9 cm	0.077°
Scan 2	ZB just below insert	12 bit	On	22.9 cm	0.077°
Scan 3	ZB just below insert	6 bit	On	22.9 cm	0.077°
Scan 4	ZB just below insert	12 bit	Off	22.9 cm	0.077°
Scan 5	ZB just below insert	12 bit	On	37.2 cm	0.077°
Scan 6	ZB just below insert	12 bit	On	22.9 cm	0.244°

SPED measurements were also done on another NW in order to test how the algorithms work on a different structure, and also test whether the strain in different rotations are symmetric or asymmetric due to the 3D shape of the NW. This was done by doing SPED on a NW through the hexagonal face (in the $[1\,\overline{1}\,0]_{ZB}$ orientation) near 0° x-tilt of the sample holder, and rotated ca. +30° (at the $[2\,\overline{1}\,\overline{1}]_{ZB}$ zone) and -30° (near the $[2\,1\,1]_{ZB}$ zone) from this face around the length of the wire. Due to a beam tilt-shift impurity affecting the NanoMEGAS scanner alignment, these data sets were collected using the Topspin software [48]. This software collects the data with a pixel

---

[2]Convergence angle and camera length values are calibrated, see Appendix A.

depth of 24 bit, and exports it either as an 8 bit binary large object (BLO) file or a stack of tag image file format (TIFF) files. In order for the data to work with the strain mapping algorithms, the data sets were exported as stacks of 12 bit TIFF files. The data sets were taken with a camera length of 22.9 cm, convergence angle of 0.077°, and an exposure time of 10 ms. They were all taken with a nominal precession angle of 0.5° (calibrated in [1] to be 0.582°), except one data set at -30° tilt, which was done with a precession angle of 1°. This was done in an attempt to improve the field of view of the DPs, as they were a bit off-zone due to tilting limitations of the sample holder in the negative tilt.

4 Results

Overview BF images of the GaAsSb NWs studied in this thesis, as observed from initial TEM, can be seen in Figure 4.1. They were both chosen because of their alignment with the y-axis of the TEM goniometer, making tilting around the growth axis of the wire much easier. They both have a defined heterostructure, indicated by blue arrows in Figure 4.1. The size of the heterostructure insert regions, as well as the concentration of Sb in the regions differ for each individual NW (the length varies between ca. 100 nm-200 nm, the maximum fraction of Sb atoms was not measured during screening). The NW used for the main part of the strain mapping, seen in Figure 4.1(a), had a width of 144 nm (in the $[1\bar{1}0]_{ZB}$ orientation), a length of about 4 μm, and an GaAsSb insert region of about 130 nm in length. The second NW used as a control for the methods used on the main NW can be seen in Figure 4.1(b). It had a width of 106 nm, length of about 4 μm and an GaAsSb insert region of about 120 nm in length. The focus of this study has been to analyse the strain in these NWs with different algorithms and parameters, and thus the TEM and S(P)ED data collection has been done in a region around the strained GaAsSb insert (as can be seen in Figure 4.2(b) and (c))

(a)   (b)
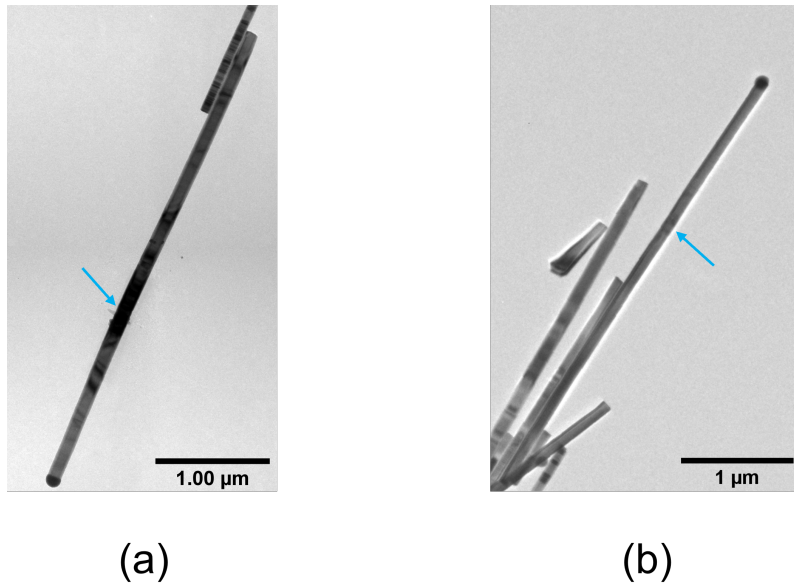
Figure 4.1: Overview TEM images of the example NWs studied in this thesis. The images show (a) the main NW, and (b) the second NW. They are both aligned along the holder y-axis so NWs can easily be rotated around long axis. The NWs both have a GaAsSb insert, indicated by blue arrows.

This chapter will start with a general characterisation of the main NW based on conventional TEM data. Next, the effect of the microscope and sample set-up will be presented, followed by the same for the scan settings. Then the results of the data processing and the three different methods will be presented, and finally the results from the second NW will be given.

4.1 General NW characterisation

The initial characterisation of the NW was done in the $[1\,\overline{1}\,0]_{ZB}/[2\,\overline{1}\,\overline{1}\,0]_{WZ}$ orientation. The reason for this is that in this orientation, the two crystal structures of GaAs are distinguishable from one another both when looking at the stacking sequence of atom planes in real space and looking at the DPs, as presented in section 2.7. This can also be seen when looking closer at the BF image of the NW in this orientation. In Figure 4.2(a), the BF of the NW, imaged in the $[1\,\overline{1}\,0]_{ZB}/[2\,\overline{1}\,\overline{1}\,0]_{WZ}$ orientation, is rotated in order to make results and discussion easier. This is the rotated view that will be used consistently through this thesis, with the GaAs droplet on the top of the image. The red square indicates the area around the GaAsSb insert that has been evaluated in this study. Figure 4.2(b) shows a close up of this area. There is a distinct change in contrast for the transition between the ZB and the WZ structure, marked with a yellow arrow. When looking at the same region with the NW tilted 30° to the $[2\,\overline{1}\,\overline{1}]_{ZB}/[1\,0\,\overline{1}\,0]_{WZ}$ orientation in Figure 4.2(c), the same transition (also indicated by a yellow arrow) ceases to be visible by image contrast. For this reason, most of the structural phase characterisation is done in the $[1\,\overline{1}\,0]_{ZB}/[2\,\overline{1}\,\overline{1}\,0]_{WZ}$ orientation. From the images of the NW, it can also be seen that the NW is not completely straight, but seems to bend with a kink at the insert.

(a)

(b)

(c)
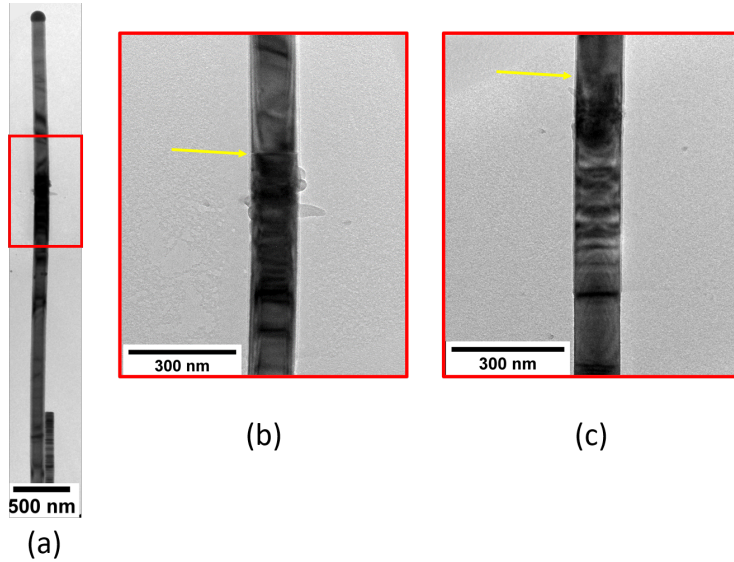
Figure 4.2: (a) BF image of the NW in the $[1\,\overline{1}\,0]_{ZB}/[2\,\overline{1}\,\overline{1}\,0]_{WZ}$ orientation, rotated in order make presentation of results and discussion easier. The area around the GaAsSb insert is marked by a red square. (b) Close up of the area around the insert in the $[1\,\overline{1}\,0]_{ZB}/[2\,\overline{1}\,\overline{1}\,0]_{WZ}$ orientation. Image contrast due to transition between ZB and WZ is indicated with a yellow arrow. (c) Close up of the same area in the $[2\,\overline{1}\,\overline{1}]_{ZB}/[1\,0\,\overline{1}\,0]_{WZ}$ orientation. The transition between ZB and WZ is indicated with a yellow arrow, but no contrast at the ZB-WZ interface is visible.

The DPs from the NW can be seen in Figure 4.3(b). The topmost DP matches the one for WZ in the $[2\,\overline{1}\,\overline{1}\,0]_{WZ}$ orientation, as discusssed in section 2.7. This is taken from the area above the GaAsSb insert, which is marked by a blue square in Figure 4.3(a). The middle DP is taken from this insert area, and coincides with the ZB pattern from the $[1\,\overline{1}\,0]_{ZB}$ orientation. This is also the case for the bottom DP, which is taken some way below the insert. A schematic of the different regions of this section of the NW can be seen in Figure 4.3(c).

This structure can also be seen if a collection of DF images are considered. In Figure 4.4, one BF
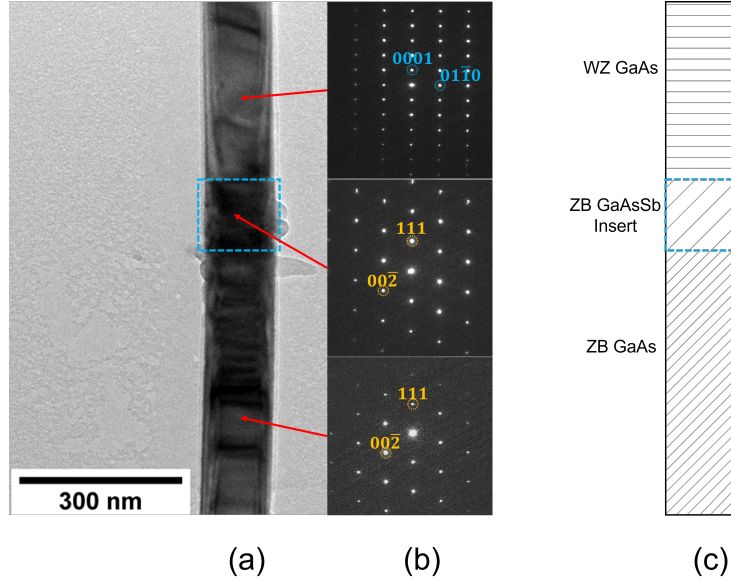
Figure 4.3: (a) BF image of the NW in the $[2\,\overline{1}\,\overline{1}]_{ZB}$ and $[1\,0\,\overline{1}\,0]_{WZ}$ orientation, with the GaAsSb insert region marked with a blue square. (b) Indexed DPs from the different regions in the NW, indicated with red arrows. WZ indices are given in blue and ZB indices are given in yellow. (c) Schematic of the different regions in the NW. Also here the insert is marked by a blue square.

and three DF images are shown. The contrast of these images are varying through the image due to dynamical effects. The DP for the images is taken at the transition between the WZ and the ZB regions, such that peaks from both structures contribute to the pattern. The BF image in Figure 4.4(a) is taken with the AP around the $(0\,0\,0)_{ZB}/(0\,0\,0\,0)_{WZ}$ peak, i.e. the direct beam. The electrons that contribute to this image are the ones that go straight through the sample without being scattered, and thus the carbon film the NW is laying on is bright, while the NW itself is dark. The first DF image in Figure 4.4(b) is taken with the AP around the $(0\,0\,0\,\overline{1})_{WZ}$ reflection. In this image, the insert is dark while the rest of the NW is illuminated, the WZ close to the insert being the brightest. In Figure 4.4(c), the DF is taken with the AP around the $(0\,1\,\overline{1}\,0)_{WZ}$ reflection. From this it can be seen that the whole NW above the insert contribute to this reflection, meaning that this whole region is probably of the WZ structure. In the lower part of the NW two planes, marked by a yellow arrow in the figure, can also be seen contributing to the DF image. These are probably stacking faults, that is planes with WZ stacking inside of a ZB structure, as presented in section 2.3. The last DF image, in Figure 4.4(d), is taken with the AP around the $(\overline{1}\,\overline{1}\,1)_{ZB}$ reflection. It can be seen from this image that the lower part of the NW, including the insert, is contributing to this DF image. We see that the region between the planes illuminated in (c) are missing, marked by a yellow arrow, furthering the theory about stacking faults in this area. The fact that the whole section is missing, not just the planes may be a result of a twinning in this area, also presented in section 2.3. Additionally, a line-like feature is visible in the WZ region of the NW, marked by another yellow arrow, which is another stacking fault. This time it is a ZB stacking in WZ (e.g. ...ABABABCABAB...).

The crystal structures of the NW can also be investigated using HRTEM. In Figure 4.5(a) a HRTEM image of the transition region between the insert, which is ZB structure, and the WZ region can be seen. From this image, the sharp transition line between the two phases can be seen more clearly, and there is not a sharp, single plane transition, but rather multiple planes.
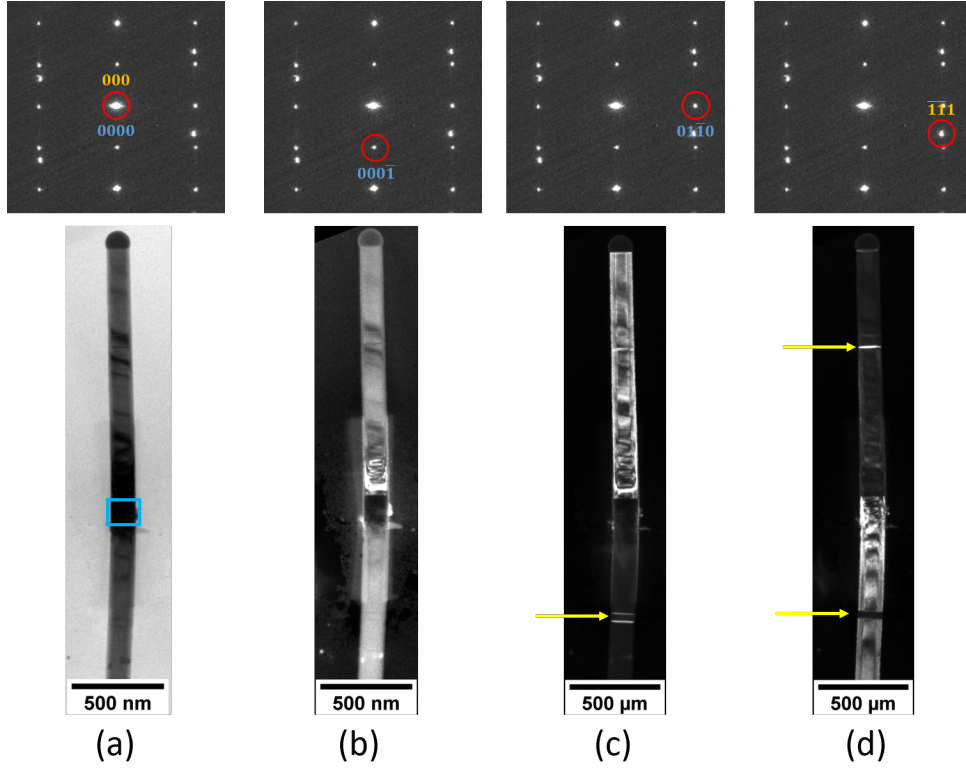
Figure 4.4: A series of BF/DF images of the NW. The aperture is represented by a red circle, and the index of the chosen reflection is given in either yellow for the three indices of the ZB structure, or blue for the four indices of the WZ structure. In (a) the insert is marked with a blue square, and stacking faults are marked with yellow arrows in (c) and (d).

By looking more closely at the transition, as can be seen in the yellow square in Figure 4.5(b), it can be seen that there is a twinning in the stacking between the ZB and the WZ. The different stacking sequences are indicated by yellow arrows. From the bottom up, the stacking sequence is ABCABCABC..., but at a certain point before the change into WZ it changes stacking to CBACBACBA..., which rotates the crystal structure about the growth direction. This can be seen as a change in the direction of the atomic columns. After the transition, the stacking sequence is ABABAB..., which is the stacking sequence for WZ. The length of the twinned stacking sequence is about 6 d_{111} stacking layers, which is a little under 2 nm. Looking more closely at the WZ section in the red square, the stacking sequence can be seen quite clearly to be ABABAB..., indicated by the red arrow. The stacking sequence of the ZB in the green square can be seen to be ABCABCABC..., direction of the atomic columns indicated by a green arrow. The FFTs of the WZ and ZB structures can be seen in Figure 4.5(c), which produce a similar pattern to the DPs from the same regions shown in Figure 4.3. Note that when the NW is tilted 30° to the $[2\,\overline{1}\,\overline{1}]_{ZB}/[1\,0\,\overline{1}\,0]_{WZ}$, the stacking faults, twin planes and phase boundaries have no contrast in BF, DF or HRTEM as the projected stacking order appear identical (as seen in section 2.7).

A gradual shift in the peak intensities of the DPs along the growth direction can be seen in the NW. This is due to the fact that the NW bends along its growth direction. Figure 4.6(a) shows an overview BF image of the NW in the $[1\,\overline{1}\,0]_{ZB}/[2\,\overline{1}\,\overline{1}\,0]_{WZ}$ orientation. The red square indicates the region where S(P)ED data has been gathered. The resulting navigation image can be seen in Figure 4.6(b), which was taken with the NW rotated 30° to be in the $[2\,\overline{1}\,\overline{1}]_{ZB}/[1\,0\,\overline{1}\,0]_{WZ}$ orientation.

The data is taken with the parameters given for scan 1 in Table 2, and is about 200 nm in width and 1000 nm in length. The DPs taken from different points along the growth direction of the NW can be seen in Figure 4.6(c). The peak intensities vary throughout, with the intensities shifting downward with the lower positions on the NW. This bending limits the scan length feasible for strain measurements, which rely on the same reflection peaks having a certain intensity throughout the whole scan.

(a) (b) (c)
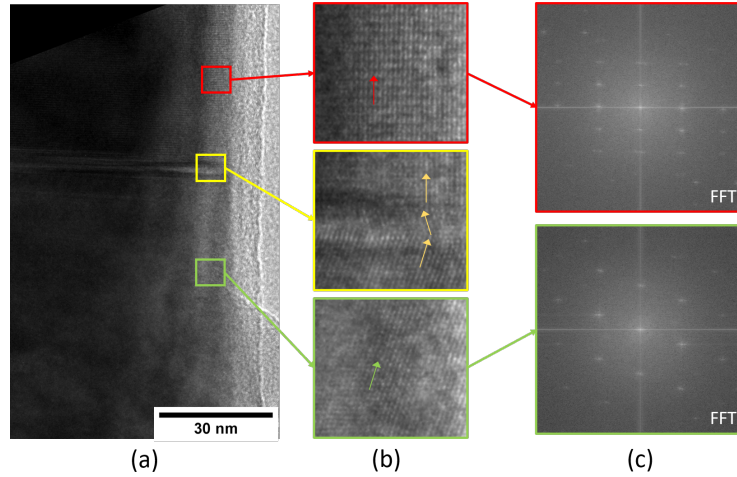
Figure 4.5: (a) TEM image of the transition region between the ZB insert and the WZ region of the NW at high magnification. (b) Close up of the different structures; WZ is in the red square, transition between WZ and ZB is in the yellow square, and ZB is in the green square. Stacking sequences are shown with arrows. (c) FFTs of the WZ and ZB region.

(a) (b) (c)
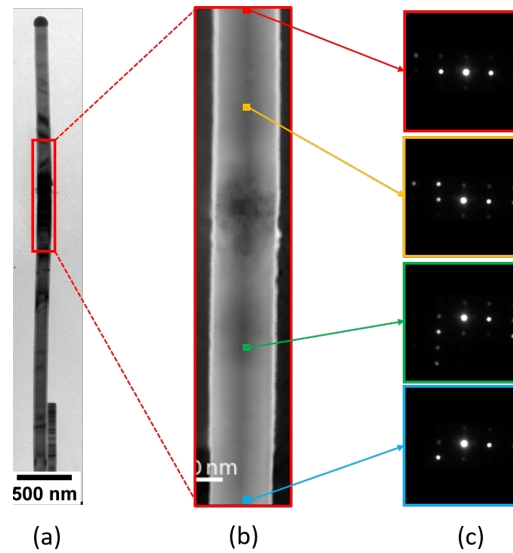
Figure 4.6: (a) BF image of the NW in the $[1\,\overline{1}\,0]_{ZB}/[2\,\overline{1}\,\overline{1}\,0]_{WZ}$ orientation, with red square indicating the scan area for SPED. (b) SPED scan (NW now rotated 30°), with parameters given in Table 2 for scan 1. (c) Separate PED patterns along the growth directions of the wire, showing the shift in peak intensities due to bending.

4.2 Strain maps

The aim of this thesis is to compare the performance of different strain measuring algorithms and how different experimental parameters affect these. The varying experimental parameters can be found in Table 2 in section 3.5. The S(P)ED data were taken around the GaAsSb insert of the NW at the $[2\,\bar{1}\,\bar{1}]_{ZB}/[1\,0\,\bar{1}\,0]_{WZ}$, (Figure 4.6(b)). This was done because the DPs for WZ and ZB looks the same in this orientation, and thus strain mapping in theory can be done for both structures at the same time. However, in this study mainly the strain behaviour in the ZB phase has been analysed. The original data scans were around $200\,\text{nm} \times 1000\,\text{nm}$, but due to bending along the growth direction, only regions of about 300-500 nm along the length of the NW could be mapped out. By using the pyXem packages for strain measurement, numerical values for the strain in the NW were found. The strain mapping routine produces four maps, two normal strains, ε_{xx} and ε_{yy}, the shear strain, ε_{xy}, and the in-plane rotation of the crystal lattice. The definitions of the directions can be seen in Figure 4.7(a,b), and the four constructed maps are shown in (c) for a baseline set up and the cross-correlation algorithm. The shear strain is given as a fraction of change in the distance between the reflection peaks, and the rotation is given as an angle in radians. The pyXem packages provides three different peak finding algorithms for the strain mapping routine, as presented in section 2.10; center of mass, Gaussian fitting, and conventional cross-correlation. All three methods calculate strain by comparing peak positions in an unstrained area with peak positions in the rest of the DP stack. The DP in the unstrained reference area is found by averaging the DPs in an area of 20x20 pixels in order to eliminate local DP variations. An area like this is marked on the virtual bright field (VBF) image of the data from scan 2 with a green square in Figure 4.7(b), and the resulting averaged DP can be seen in Figure 4.7(a).
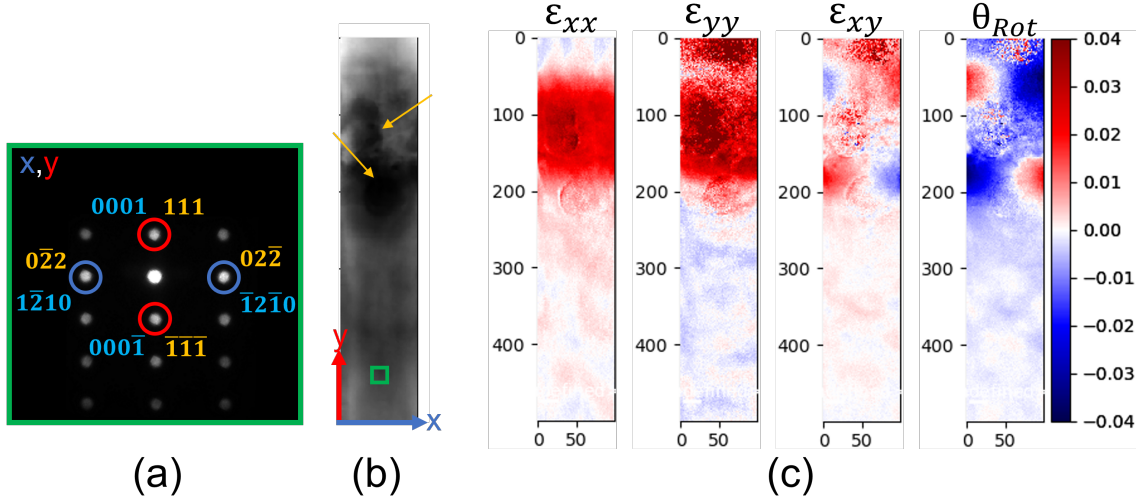
Figure 4.7: (a) Averaged DP from 20x20 pixels in the unstrained region in scan 2. x-peaks are marked with blue circles, y-peaks are marked with red circles. The indexation of each chosen peak is given in yellow for ZB indices, and blue for WZ indices. (b) VBF image of the region chosen for strain mapping around the insert in scan 2, with the unstrained region contributing to the averaged DP marked with a green square. Carbon contamination and beam damage is indicated by yellow arrows. (c) Strain maps from the same region using the cross-correlation method. This, especially ε_{yy}, will be used as a baseline for comparisons.

Two opposing reflections were chosen for both directions in the DP, instead of one, see Figure

4.7(a). This was done in order to make the strain measurements as robust against wobbling and other DP collection problems as possible. As bending in the NW caused the intensities of the DP reflections to shift, the closest orthogonal reflections were chosen for the strain measurements, to ensure that they were detectable in all DPs throughout the scan. The peaks chosen for the normal strain in the x-direction, ε_{xx}, were the $(0\,\overline{2}\,2)_{ZB}/(1\,\overline{2}\,1\,0)_{WZ}$ and $(0\,2\,\overline{2})_{ZB}/(\overline{1}\,2\,\overline{1}\,0)_{WZ}$ reflections. This direction coincides with the direction going across the width of the NW in real space, which will also be referred to as the x-direction. The peaks chosen for the normal strain in the y-direction, ε_{yy}, were the $(1\,1\,1)_{ZB}/(0\,0\,0\,1)_{WZ}$ and $(\overline{1}\,\overline{1}\,\overline{1})_{ZB}/(0\,0\,0\,\overline{1})_{WZ}$ reflections. This direction coincides with the growth direction of the NW in real space, and thus it will also be referred to as the y-direction.

In order to be able to compare the different scan parameters and their effect on the strain measurements, a baseline case needed to be established for comparison. The baseline data set was decided to be scan 2, with parameters given in Table 2. The baseline strain mapping routine was chosen to be the cross-correlation method, and the resulting strain maps from this baseline case can be seen in Figure 4.7(c). It is assumed that the normal strain in the x-direction will quickly be relaxed outside of the insert due to the small width of the NW, while the y-direction strain in GaAs will gradually relax because of the relative long length of the NW. Thus, for comparison purposes and ease of visualisation, comparisons will be done exclusively with the normal strain in the y-direction, ε_{yy}.

4.3 Illumination for strain mapping

The first set of experimental parameters that will be presented are the ones that affect the illumination of the sample. For this, two different parameters have been considered; whether the electron beam is precessed or not, and what convergence angle the beam has on the sample. The two parameters are shown in Figure 2.18(c), where ϕ is the precession angle, and α is the convergence angle. Precession of the beam takes about $10\,\mathrm{ms}$ per cycle, and thus the collection of large scans with many data points is a time consuming affair. If it were possible to get equally good data for strain mapping without precession, i.e. $\phi = 0°$, as with precession, data collection could save a lot of time. Strain routines were performed on the unprecessed data, scan 4 in Table 2, for a region of 100x500 pixels at and below the insert. The averaged DP of the unstrained region, VBF and the normal strain from the cross-correlation method in the y-direction for scan 4 can be seen in Figure 4.8.

A larger convergence angle leads to a bigger disk radius in the DP. This could possibly be beneficial, because it gives the strain routines more pixels to work with. It also reduces the amount of unused space in the DP, as more of the detector is illuminated. The baseline SPED data set was collected with a convergence angle $\alpha = 0.077°$. Strain routines were performed on the data with a convergence angle $\alpha = 0.244°$, scan 6 in Table 2, for a region of 100x400 pixels at and below the insert. The averaged DP of the unstrained region, VBF and the normal strain from the cross-correlation method in the y-direction for scan 6 can be seen in Figure 4.9.
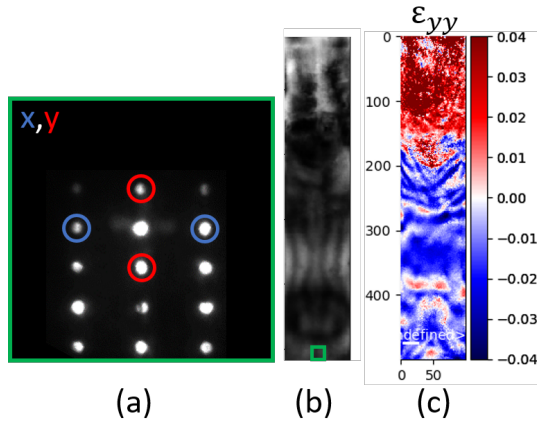
Figure 4.8: Strain mapping results from scan 4, which is taken with precession angle $\phi = 0°$. (a) Averaged DP from the unstrained reference area. (b) VBF of the area for strain mapping, with a green square indicating the area contributing to the DP in (a). (c) Map of the normal strain in the y-direction found by the cross-correlation method.
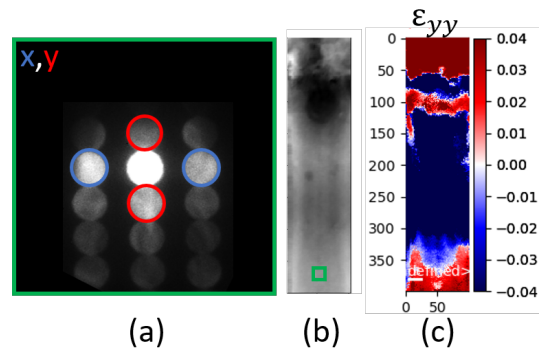
Figure 4.9: Strain mapping results from scan 6, which is taken with a larger convergence angle, $\alpha = 0.244°$. (a) Averaged DP from the unstrained reference area. (b) VBF of the area for strain mapping, with a green square indicating the area contributing to the DP in (a). (c) Map of the normal strain in the y-direction found by the cross-correlation method.

4.4 NW setup for strain mapping

The second kind of experimental parameter that will be presented is a parameter that deals with the setup of the NW itself. As presented in section 4.1, there is bending present in the NW, which affects the peak visibility in the SPED DPs. Because of this, it could be of import which NW region is aligned as on zone in the microscope for the resulting strain map. There are two requirements for the strain measuring routines to work properly. The first is that the region of interest, i.e. where it is desirable to measure strain, has to be on zone, or at least near. If this requirement is not met, the routines are not able to detect DP reflections, and the strain measurements become more unreliable. The second requirement is that an unstrained reference region, should be on zone. Further, if a strained region is used as reference, the strain values will be offset from their true value, as it is all measured with respect to this reference region. Therefore, it is valuable to know the importance of which region is on zone for the resulting strain map. In the baseline SPED data, a NW region below the insert was aligned to be on zone in the microscope, to be certain to have an unstrained region on zone. In the data for scan 1, the insert itself was aligned to be on zone in the microscope, in order to be certain that the region of interest was on zone. The strain routines were performed on the data for a region of 100x500 pixels around the insert. The averaged DP of the chosen unstrained region (marked by a green square), VBF and the normal strain from the cross-correlation method in the y-direction for scan 1 can be seen in Figure 4.10.
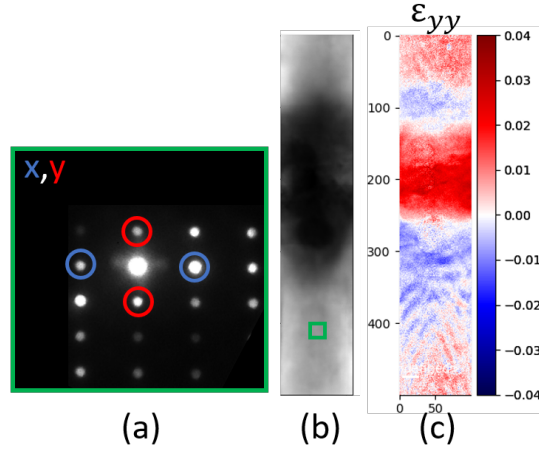
Figure 4.10: Strain mapping results from scan 1, which is taken with the insert region on zone. (a) Averaged DP from the unstrained reference area. (b) VBF of the area for strain mapping, with a green square indicating the area contributing to the reference DP in (a). (c) Map of the normal strain in the y-direction found by the cross-correlation method.

4.5   Post-specimen settings and acquisition for strain mapping

The final set of experimental parameters that will be presented are the parameters that have effect below the sample, i.e. post-specimen settings and parameters that affect the DP acquisition. Specifically two parameters have been considered; the camera length and the pixel depth of of the detector. The camera length is the effective distance between the specimen and the detector, and the longer this length is, the more magnified the DP appears on the detector. This means that each reflection disk is covering more pixels, giving the strain measuring routines more input data to work with. However, the more magnified the DP is, the lower the field of view is and fewer peaks are visible. Because of bending present in the NW, the choice of disks were limited to the reflections closest to the central beam anyway, and thus it was desirable to investigate whether a longer camera length would improve the strain measurements. The baseline SPED data set was collected with a camera length of 22.9 cm, while the data set from scan 5 in Table 2 was collected with a larger camera length of 37.2 cm. The strain routines were performed on the data for a region of 100x500 pixels at and below the insert. The averaged DP of the unstrained region, VBF and the normal strain from the cross-correlation method in the y-direction of scan 5 can be seen in Figure 4.12.

The pixel depth describes the range of values that each pixel of the DPs in the data set contains. A pixel with a depth of n can store a range of 2^n different values. The larger the pixel depth, the more values are stored per pixels, and the larger the data set becomes. Each scan point of the S(P)ED scans done in this thesis contains a DP of 256x256 pixels. A 200x1000 point scan done with a 12 bit pixel depth contains 200000 of these DPs, and has a size of 26 GB. This order of size quickly becomes difficult to handle and transfer for later data processing. The same scan done with a 6 bit pixel depth has a size of 13 GB, which is half the size. Thus, for practical reasons related to data handling, it is of interest to investigate whether the collection pixel depth has any effect on the strain measurements. If not, smaller pixel depth would be preferred, as it makes the data set size easier to handle. The baseline SPED data was collected with a pixel depth of 12 bit, while

scan 3 in Table 2 was collected with a pixel depth of 6 bit. The strain routines were performed on the data for a region of 100x500 pixels at and below the insert. The averaged DP of the unstrained region, VBF, and the normal strain from the cross-correlation method in the y-direction of scan 3 can be seen in Figure 4.11.
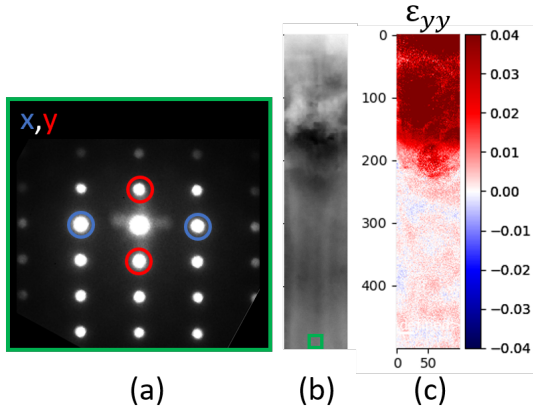

Figure 4.11: Strain mapping results from scan 3, which is taken with a smaller pixel depth of 6 bit. (a) Averaged DP from the unstrained reference area. (b) VBF of the area for strain mapping, with a green square indicating the area contributing to the DP in (a). (c) Map of the normal strain in the y-direction found by the cross-correlation method.
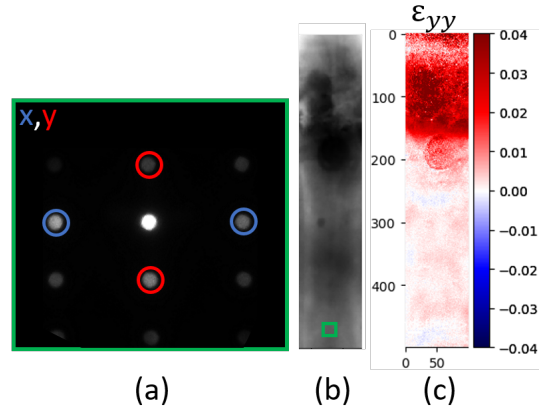
Figure 4.12: Strain mapping results from scan 5, which is taken with a larger camera length. (a) Averaged DP from the unstrained reference area. (b) VBF of the area for strain mapping, with a green square indicating the area contributing to the DP in (a). (c) Map of the normal strain in the y-direction found by the cross-correlation method.

4.6 Data processing for strain mapping

In addition to evaluating the effects of different experimental parameters, three different strain mapping routines have been applied to the data sets. The routines are based on, as discussed in section 2.10, the cross-correlation method (used as baseline), the center of mass method and the Gaussian fitting method. Three different parameters were chosen in addition to the baseline of scan 2, for comparison purposes of these three routines. In order to be able to compare the three methods, the strain routines have been applied to the same area of the NW. The Gaussian fitting method is based on the assumption that it is possible to fit a Gaussian curve to the intensity profile of a DP disk. Thus, if the signal-to-noise ratio is very low in a DP due to for example sample contamination, or if the peak intensity does not follow a bell-shaped curve, the routine does not produce any results. This is not the case for the other routines, which are more robust regarding signal quality and producing results. Thus, due to some sample contamination on the insert, indicated by yellow arrows in Figure4.7(b), the region for strain routine comparisons was limited by the area where the Gaussian fitting method was able to produce results. For most data sets, the regions were 300-350 pixels long, however the scan 3, 4 and 6 data sets were so unsuitable for the Gaussian fitting method that the routine could not produce any meaningful results at all. In the case where the Gaussian method did not produce any results, the two other routines have been compared. All the comparisons between the three routines will be discussed in section 5.6.

For the baseline case of scan 2, a region of 100x300 pixels just under the GaAsSb insert was

used. The VBF of this region can be seen in Figure 4.13(b). The same DP reflections (i.e. $(0\,2\,\bar{2})_{ZB}/(0\,\bar{2}\,2)_{ZB}$ and $(1\,1\,1)_{ZB}/(\bar{1}\,\bar{1}\,\bar{1})_{ZB}$) were used for all the three methods(see Figure 4.13(a)), and the resulting strain maps for the normal strain in the y-direction can be seen in Figure 4.13(c). Here, the abbreviations XC, CoM and Gaussian represents the cross-correlation method, center of mass method, and Gaussian fitting method respectively.
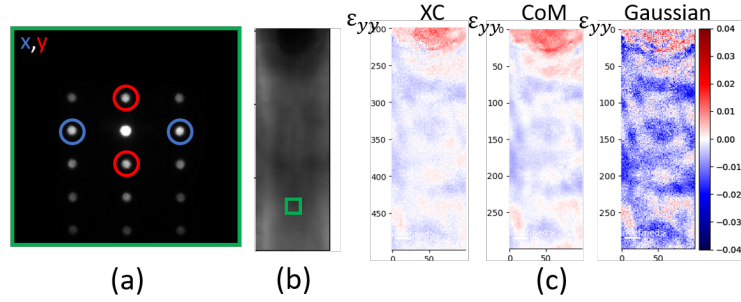
Figure 4.13: Comparison of the strain mapping routines performed on scan 2. (a) Averaged DP from the unstrained reference area. (b) VBF of the area for strain mapping, with a green square indicating the area contributing to the DP in (a). (c) The resulting strain maps (normal y-direction strain) for the three routines; cross-correlation, center of mass and Gaussian fitting.

In order to compare the strain mapping routines with regards to illumination of the sample, the strain mapping routines were performed on scan 4, with no precession. In this case, the Gaussian method did not produce any results, and thus only the cross-correlation method and the center of mass method can be compared. A region of 100x500 pixels was used for the strain mapping, and the results from the cross-correlation and the center of mass is presented in Figure 4.14. The third set of comparisons is for scan 1, where the setup of the NW is done so that the GaAsSb insert is on zone. The strain mapping routines were performed on a region of 100x300 pixels on and below the insert, and all three methods were able to create strain maps. They are presented in Figure 4.15. The final set of comparisons was done for scan 5, which had a longer camera length than the baseline data set (37.2 cm compared to the 22.9 cm of scan 2). A region of 100x350 pixels was used for the strain measurements, and the resulting strain maps are presented in Figure 4.16.
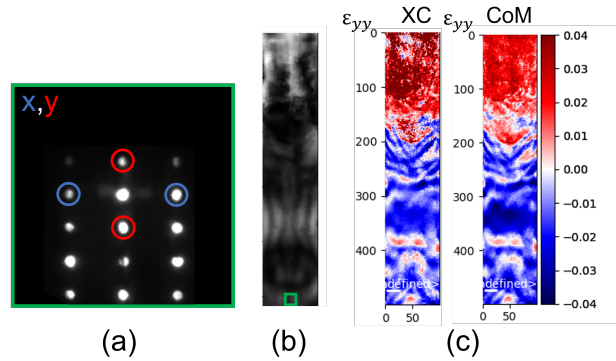
Figure 4.14: Comparison results for scan 4 with no precession. (a) Averaged DP from the unstrained reference area. (b) VBF of the area for strain mapping, with a green square indicating the area contributing to the DP in (a). (c) The strain maps (normal y-direction strain) for two of the routines; cross-correlation and center of mass.
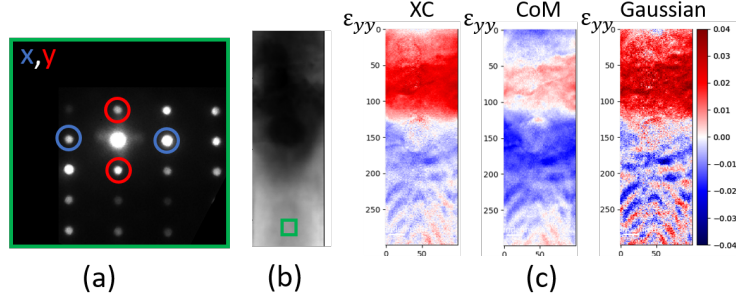
Figure 4.15: Comparison results for scan 1 with the GaAsSb insert on zone. (a) Averaged DP from the unstrained reference area. (b) VBF of the area for strain mapping, with a green square indicating the area contributing to the DP in (a). (c) The strain maps (normal y-direction strain) for the three routines; cross-correlation, center of mass and Gaussian fitting.
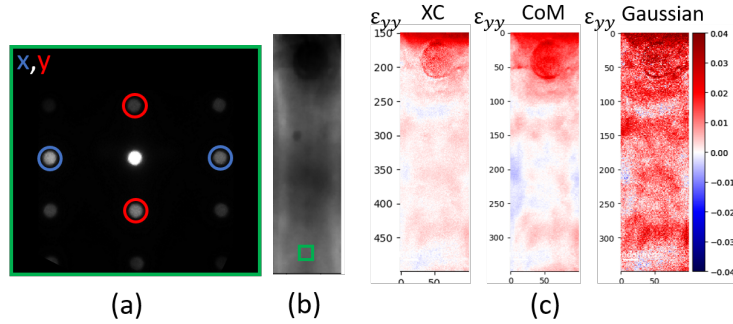
Figure 4.16: Comparison results for scan 5 with a longer camera length of 37.2 cm. (a) Averaged DP from the unstrained reference area. (b) VBF of the area for strain mapping, with a green square indicating the area contributing to the DP in (a). (c) The strain maps (normal y-direction strain) for the three routines; cross-correlation, center of mass and Gaussian fitting.

4.7 Second NW

Due to the growth process of the materials in this study (i.e. random growth so that each NW has a different local growth surrounding), no two NWs are exactly the same. There are variations in NW diameter and length, insert length, concentration of Sb in insert, amount of defects, growth sequences etc. This can be seen by comparing the two NWs in Figure 4.1. This means that they all are unique, and have a unique strain profile. Therefore, it was essential to do the analysis of various experimental parameters and method comparisons on the same NW. To put the findings in perspective, it is beneficial to study a second NW, in order to verify that the conclusions made based on one NW could be extrapolated to other NWs with the same heterostructure. An overview BF image of the second NW chosen for the study can be seen in Figure 4.1(b). This NW had a smaller diameter than the main NW (106 nm versus 144 nm), and had the same crystal phases as illustrated in Figure 4.3(c); GaAs ZB below the insert, ZB in the GaAsSb insert, and GaAs WZ above the insert. A BF image of the NW in the $[1\,\overline{1}\,0]_{ZB}/[2\,\overline{1}\,\overline{1}\,0]_{WZ}$ orientation can be seen in Figure 4.17(d), where the insert is marked by a blue square. An increased contrast can be seen due to strain in this area. The same crystal structures as the main NW can also be seen when looking at the DPs around the insert in this orientation in Figure 4.17(e), similar to Figure 4.3(b).

In addition to having a second NW as a verification, it was desirable to investigate whether the strain in different rotations are symmetric or asymmetric due to the 3D shape of the NW. The strain mapping routines only calculate the 2D projection of the strain, as introduced in section 2.9, and thus the NW tilt around the growth direction may show signs related to the overall 3D structure of the NW. Thus, SPED data was collected from the $[1\,\overline{1}\,0]_{ZB}/[2\,\overline{1}\,\overline{1}\,0]_{WZ}$ orientation of the wire, i.e. from the hexagonal face, and tilted $+30°$ and $-30°$ from this face to the hexagonal vertices. The BFs of the three rotations can be seen in Figure 4.17(a)-(c). In the $[1\,\overline{1}\,0]_{ZB}/[2\,\overline{1}\,\overline{1}\,0]_{WZ}$ orientation of Figure 4.17(b) and (d), many dark contrast lines can be seen in the WZ region above the insert. These are due to stacking faults, which there is a high density of in the upper part of the NW.
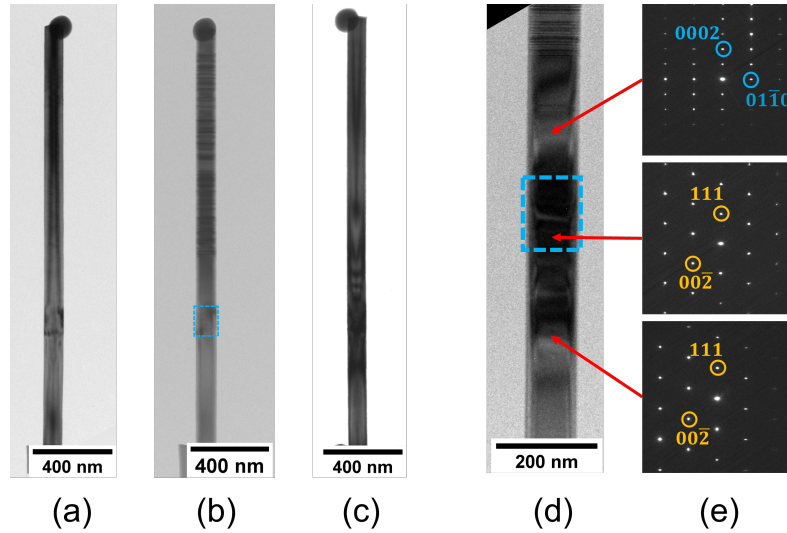
Figure 4.17: BF images from the second NW (a) tilted $+30°$ (b) tilted $0°$ and (c) tilted $-30°$ from the $[1\,\overline{1}\,0]_{ZB}/[2\,\overline{1}\,\overline{1}\,0]_{WZ}$ orientation. Insert marked with blue square in (b). (d) Closer BF of the region around the insert (marked by blue square) with $0°$ tilt, and (e) DPs along the NW indicating the different crystal phases. WZ indexation is written in blue, while ZB indexation is written in yellow.

The SPED data from the first and the second NW was taken almost two months apart. Due to a beam tilt issue with the microscope setup, the data from the second NW had to be taken with another software. The data from the main NW was collected using the NanoMEGAS ASTAR acquisition software, while the data from the second NW was collected using their Topspin PED Acquisition software. The softwares both use the same detector for data collection, but they operate with different storage procedures. In the ASTAR software, the collection bit depth is specified before the data is gathered, and the data is exported with the same format as it is collected. In the Topspin software, all data is collected as 24 bit data no matter the circumstances. When the data is later exported and saved, some unknown compression is done into either an 8 bit BLO file, or a stack of TIFF files with user specified pixel depth. The resulting DPs from this process turned out to be difficult for the strain mapping routines to interpret, and some additional data processing had to be performed. The data was exported as 12 bit TIFF files, each file containing one DP, which were collected and put together into a single Hierarchical Data Format 5 (HDF5) file. The data in this file was then converted to logarithmic scale, and background subtraction using difference of Gaussians (provided by pyXem) was performed, before the strain mapping routines could be applied. This data handling could affect the final strain analysis, although in this study it is assumed that it does not. An example DP from the BLO file format, and from the HDF5 file format before and after processing can be seen in Figure 4.18.
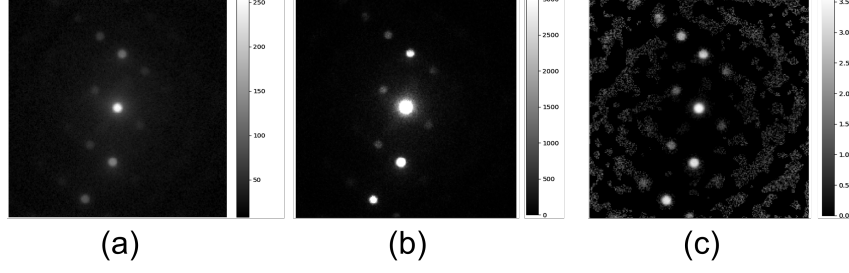
Figure 4.18: SPED data gathered from the second NW tilted +30° and viewed as (a) 8 bit BLO file, (b) 12 bit HDF5 file, and (c) HDF5 file with logarithmic scale and background subtraction.

For the SPED data acquisition, the NW was aligned on zone in the ZB area below the insert, and the experimental parameters were the same as for the baseline case for the main NW (see scan 2 in Table 2). However, as mentioned in section 3.5, due to tilt limitations of the specimen holder it was not possible to tilt the NW completely −30° to the $[2\,1\,1]_{ZB}$ orientation. In an attempt to extend the field of view of the DPs, this data set was taken with a precession angle of 1°, instead of the 0.5° precession angle of the two other scans.

The strain mapping routines were performed on data sets of about 40x300 data points, with a scan probe of about 1 nm and a step size of 1.684 nm/pixel. Also for this NW, the area for strain mapping comparison was limited by the Gaussian fitting method. For the 0° tilt at zone $[1\,\overline{1}\,0]$, the strain mapping was done for 40x255 pixels at and below the insert. In order for the directions in the DP to match up with the directions in the NW that was used for the ±30° tilt and the main NW, the peaks used for this tilt were the $(\overline{2}\,\overline{2}\,4)_{ZB}/(2\,2\,\overline{4})_{ZB}$ reflections as the x-direction and the $(1\,1\,1)_{ZB}/(\overline{1}\,\overline{1}\,\overline{1})_{ZB}$ reflections in the y-direction. The reflections are marked in the averaged DP used as the unstrained reference in Figure 4.19(a). For the Gaussian method, only the $(\overline{2}\,\overline{2}\,4)_{ZB}$ reflection was used in the x-direction, in order to make the routine run. As the analyses of this thesis is done with the normal strain in the y-direction, this should not affect the results. The VBF image of the scan can be seen in Figure 4.19(b), with the region contributing to the averaged unstrained DP marked by a green square. The resulting strain maps of the normal strain in the y-direction for three routines can be seen in Figure 4.19(c).
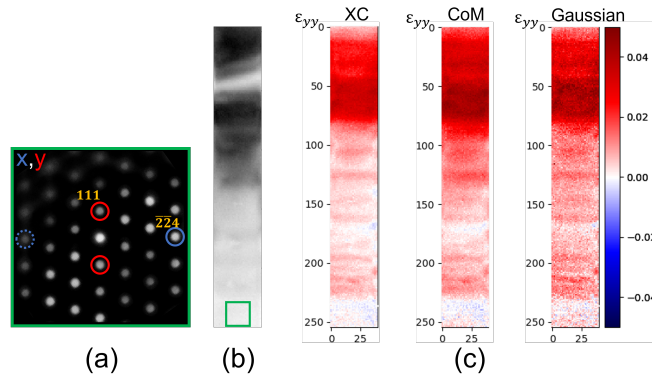
Figure 4.19: Comparison results for the NW tilted 0°, at zone $[1\,\overline{1}\,0]_{ZB}$. (a) DP averaged over the reference area. (b) VBF of the area for strain mapping, with a green square indicating the unstrained reference area. (c) ε_{yy} strain maps for the routines; cross-correlation, center of mass and Gaussian fitting.

For the +30° tilt at zone $[2\,\overline{1}\,\overline{1}]_{ZB}$, the strain mapping was done for 45x260 pixels at and below the insert. The same reflection peaks were used for this scan as the ones for the main NW, which are indexed in Figure 4.7(a). The results of the three strain mapping routines can be seen in Figure 4.20(c), together with the averaged DP in (a) and the VBF (b). For the −30° tilt scan near zone $[2\,1\,1]_{ZB}$, the strain mapping was done for 40x300 pixels around the insert. Due to the tilt being not completely −30°, the reflections in the x-direction were too weak for the Gaussian fitting method to work. Therefore, only the maps for the normal strain in the y-direction from the cross-correlation method and the center of mass method can be seen in Figure 4.21(c). The averaged DP from the unstrained region is shown in Figure 4.21(a), and the VBF with this region indicated by a green square is shown in (b).
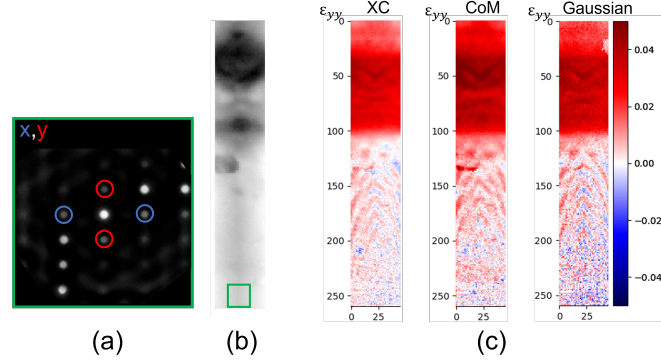
Figure 4.20: Comparison results for the NW tilted +30°, at zone $[2\,\overline{1}\,\overline{1}]_{ZB}$. (a) DP averaged over the reference area. (b) VBF of the area for strain mapping, with a green square indicating the unstrained reference area. (c) ε_{yy} strain maps for the routines; cross-correlation, center of mass and Gaussian fitting.
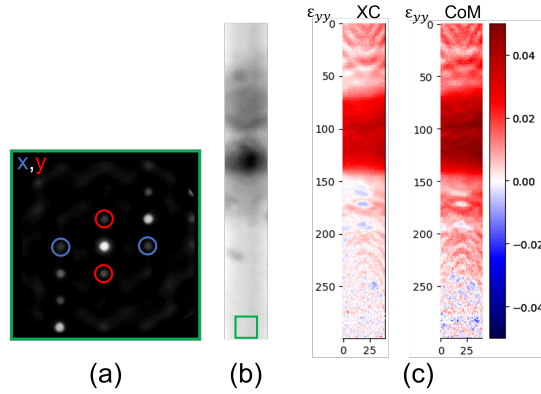
Figure 4.21: Comparison results for the NW tilted −30°, near zone $[2\,1\,1]_{ZB}$. (a) DP averaged over the reference area. (b) VBF of the area for strain mapping, with a green square indicating the unstrained reference area. (c) ε_{yy} strain maps for two of the routines; cross-correlation and center of mass.

5 Discussion

5.1 General NW characterisation

The GaAs/GaAsSb heterostructured NWs used in this study are well characterised and studied structures. The general phase structure of both the NWs was found to be ZB at and below the GaAsSb insert, and WZ above, with a Ga droplet on top of the wire. This is consistent with studies done on similar NWs [44, 1], and also consistent with characterisation of the main NW done before by Tor Inge Thorsen in his Master's thesis [45]. The main purpose of the detailed characterization by conventional TEM techniques of the NWs studied in this thesis, is to have a solid reference for interpreting the results of the strain analysis based on S(P)ED later. Difference in phases in different parts of the NW leads to different DPs in the $[1\,\overline{1}\,0]_{ZB}/[2\,\overline{1}\,\overline{1}\,0]_{WZ}$ orientation, as can be seen in Figure 4.3(b), which makes structural characterisation easier. This is well illustrated in the DF images of the NW (Figure 4.4). It is then possible to distinguish between features such as different crystal phases, phase boundaries, stacking faults and twin planes. Therefore, the phase and defect analysis by conventional TEM was done in this orientation. However, there is no visible distinction between the GaAsSb insert and the lower GaAs part on the NW, as both have ZB structure. In the DF image of the NW with the $(0\,0\,0\,\overline{1})_{WZ}$ reflection selected (Figure 4.4(b)), a dark area can be seen where the insert is located, but this is too unprecise to determine the exact extension of the insert into the ZB. It can therefore be difficult to determine exact length of the insert measured from the WZ-ZB interface. In this thesis, the size of the inserts has been found by a combination of analysing the detected strain in the NW and BF/DF TEM images of the insert region. In order to be more certain of the size of the insert, the presence of Sb atoms could have been measured, for example by EDX to determine the extension of the insert [49].

By looking at HRTEM images of the insert and the WZ-ZB interface, it can be seen that there is a twinned ZB region in this interface (Figure 4.5). It is assumed that the larger lattice constant of the GaAsSb insert will cause strain that perhaps will extend into the NW both above and below. However, it is uncertain what effect the twinned plane will have on this strain. It has been shown that twin planes in NW structures help relax lattice strain [50]. It is therefore difficult to tell what the strain profile will look like in the WZ phase, due to this twin region at the WZ-ZB interface, and whether it will extend significantly into the WZ region. The interface between the insert and the GaAs ZB phase, on the other hand, does not have such an abrupt transition that could relieve strain, because both regions are in the ZB structure. As the area that could be used for strain mapping was limited by bending in the NW, strain characterisation in the ZB phase was prioritised.

When the NW is rotated 30° to the $[2\,\overline{1}\,\overline{1}]_{ZB}/[1\,0\,\overline{1}\,0]_{WZ}$, the projected stacking order of the different phases appear identical, and all the different features look identical, including the DPs. For structural characterisation, this is not ideal. But, the main aim of this thesis is to explore ways to analyse the local strain in the NWs by diffraction data. In this case, it is perhaps beneficial that the different features cannot be distinguished, as the DPs look the same, and thus contain the same reflections, which is advantageous for the routines. Therefore, most S(P)ED data for strain measurements were collected in this orientation.

As mentioned, the main NW had already been studied by Thorsen in his Master's thesis. The use of numbered grids allows for repetitive study of the same nano-objects by different people in different microscopes. However, the accumulated electron beam dose in a small area and the fact that the NW was extensively imaged during this thesis, leads to a build up of carbon contamination

and some areas of electron beam damage on the NW insert. This had some effect on the S(P)ED data collected from the insert, mainly lowering the signal-to-noise ratio in certain areas. It was still desirable to analyse this specific NW, however, because the results could then be seen in context with the previous strain analysis done by Thorsen with a different detection method (as will be discussed in section 5.2). In addition, the beam damage on the carbon film functioned as a good marker for the insert, which was not visible in the $[2\,\overline{1}\,\overline{1}]_{ZB}$ orientation.

As established in results, and also in previous studies of this type of self-catalysed NW, each NW has an individual structure, with different diameter, length, Sb concentration in insert, length of insert, and amount of stacking faults [51]. A large part of this thesis has been investigating the effect of different experimental parameters on the strain mapping results, and how the different strain mapping routines compare when measuring strain in nm-scale heterostructures. In order to have comparable data, the screening of the various different experimental parameters were done on the very same NW, and most of the routine comparisons were done on this NW as well. The conclusions from this analysis were then investigated and confirmed using data from a second NW with slightly different characteristics such as length, diameter and strain contrast.

5.2   Strain maps

One of the motivations for investigating the most suited parameters and routines for strain mapping is the emergence of new detector technology. The strain in the main NW has been analysed once before, by Tor Inge Thorsen in his master's thesis [45]. His analysis only extended to the center of mass method (which was the only strain mapping routine integrated in pyXem at the time), and was done with data recorded by a Stingray optical camera. This camera has a size of 144x144 pixels, and was mounted outside the viewing window of the TEM taking images of the DPs on the fluorescent viewing screen. This indirect imaging give artifacts, such as glare and geometric distortions [52, 53]. Since then, a new silicon MerlinEM direct electron detector with a size of 256x256 pixels has been installed, which is located under the viewing screen and records DPs directly. This detector gives clearer data with higher resolution, and it was desirable to explore whether data taken with this detector produced more accurate strain maps. The routines from the pyXem library was also mainly developed using data from Stingray cameras, which further motivated the subject of this thesis. A set of example data and resulting strain maps from Thorsen's master's thesis, and the baseline data set from this thesis for comparison, can be seen in Figure 5.1. Both data sets are taken from the same NW in roughly the same place around the GaAsSb insert, and both are taken at a 30° tilt from the $[1\,\overline{1}\,0]_{ZB}/[2\,\overline{1}\,\overline{1}\,0]_{WZ}$ orientation. The Stingray data is taken with a precession angle $\phi \approx 0.64°$, convergence angle $\alpha \approx 0.074°$, and a camera length of ~19.65 cm.

Visually comparing the two sets of strain maps, it can be seen that the maps obtained from the data taken with MerlinEM detector have a much more distinctly visible insert and sharply defined features, both looking at the normal strain in the x- and y-direction. Both sets of strain maps have values fluctuating further away from the insert, but the strain maps obtained from the Stingray data fluctuate much more, and seems less stable. There may be many reasons for this. One reason is that the MerlinEM detector records the DPs directly from the electron beam of the microscope. This means that challenges related to the imaging of the fluorescent viewing screen such as electron afterglow and pattern distortion due to imaging angle are eliminated. Another reason may be that the resolution of the Stingray detector is lower, 144x144 pixels per DP, versus the resolution of the MerlinEM detector, which is 256x256 pixels per DP. This means that the strain measuring routines have more pixels per peak to work with, and thus could potentially determine the peak position more accurately. Additionally, the strain mapping routines used for the two data sets
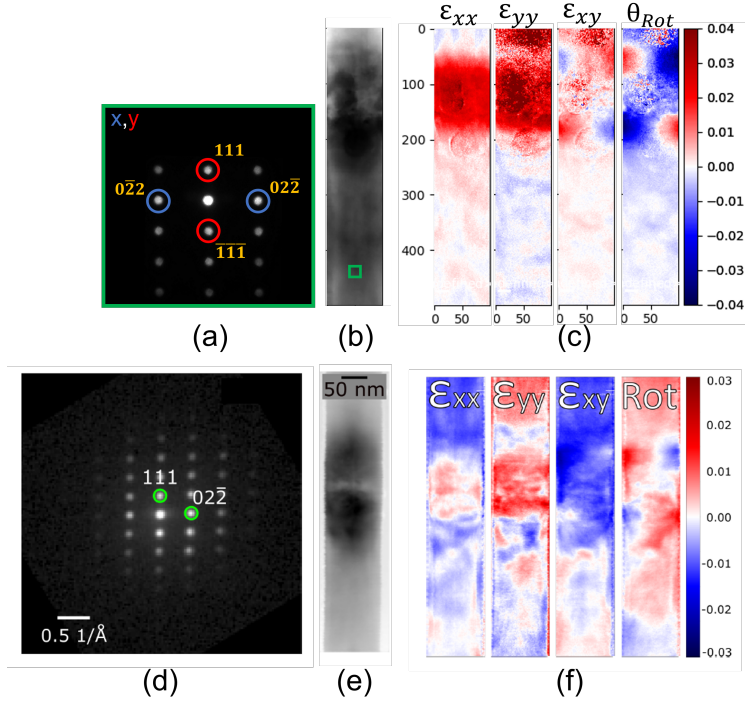
Figure 5.1: Comparisons between the MerlinEM detector, (a)-(c), and the Stingray camera. (d)-(f). Both data sets are taken from the $[2\,\overline{1}\,\overline{1}]_{ZB}$ orientation of the same NW. (a) Averaged reference DP from the MerlinEM detector, with x- and y-peaks indicated by circles. (b) VBF of the NW, with a green square indicating the reference region used for strain mapping. (c) Generated strain maps from the cross-correlation method. Data is from scan 2. (d) DP obtained with the Stingray optical camera. (e) VBF image of the strained area. (f) Strain maps from reflections marked in (a), with $(0\,2\,\overline{2})$ being the x-peak and $(1\,1\,1)$ being the y-peak.

are different. The center of mass method used with the Stingray data is sensitive to uneven peak illuminations, and thus might not be the best fit for the data. The differences between the strain mapping routines will be discussed further in section 5.6.

A comparison between the SPED data from the two different detection methods can be seen in Figure 5.2. The DPs are taken from the same NW in roughly the same places. The DP from the MerlinEM detector (Figure 5.2(a)) is taken at the $[2\,\overline{1}\,\overline{1}]_{ZB}$ orientation of the NW, while the DP from the Stingray camera is taken at the $[1\,\overline{1}\,0]_{ZB}$ orientation. From just visual inspection of the data, it can be seen that the MerlinEM detector has a much darker background than the Stingray camera, which shows significant noise between the disks. A line is drawn in the $[1\,1\,1]_{ZB}$-direction in both data sets, in order to do an as fair comparison of the data as possible. Comparing the two intensity profile along these lines, it is apparent that the MerlinEM detector has higher intensity in the reflection disks (200-1200 pixel intensity for the 5 peaks in the center of the DP) than the Stingray camera (125-175 pixel intensity for the same peaks). However, the noise levels are the same for the Stingray camera and the MerlinEM detector (25-50 pixel intensity). This leads to a much higher signal-to-noise ratio for the MerlinEM detector than the Stingray camera, which is consitent with similar comparison studies [52, 53]. This could give an explanation of why the strain routines give a better result using the new MerlinEM detector, compared to the Stingray camera.
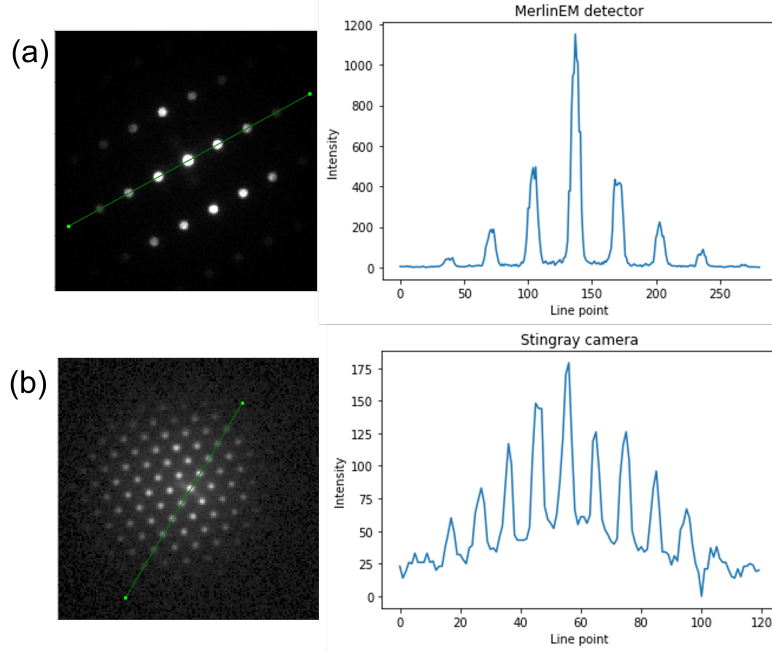
Figure 5.2: (a) DP collected with the MerlinEM detector. The intensity profile is plotted along the green line in the DP. (b) DP collected with the Stingray optical camers. The intensity profile is plotted along the green line in the DP.

In order to be able to say anything about the accuracy of the strain measurements in this thesis, some expectations of what the results should look like are provided. In the heterostructured NWs, the strain originates from the presence of Sb atoms in the GaAsSb insert, as presented in section 2.9. The theoretical lattice parameter for GaAs in the ZB phase is $5.563\,\text{Å}$, while the theoretical lattice parameter for GaSb is $6.095\,\text{Å}$. Therefore, positive strain, i.e. tension, is expected in and around the insert region. The growth direction, i.e. the y-direction, of the NW is the $[1\,1\,1]_{ZB}$ direction, and by using the equation for interplanar spacing in a cubic structure (eq. 2.2) d_{111} for both GaAs and GaSb can be calculated. For pure GaSb, this spacing is about $7.8\,\%$ larger than for GaAs. This means that if all the As atoms in the insert are replaced with Sb atoms, a strain of 0.078 should be expected. The fraction of Sb atoms in the insert is unknown, but a study done by Todorovic *et al.*[49] for similar NWs show that the concentration of Sb is linked with the length of the insert, and typically is less than $30\,\%$ for inserts under $100\,\text{nm}$. The NWs in this thesis have lengths of around $130\,\text{nm}$ and $120\,\text{nm}$, and thus an assumption of an Sb concentration of no more than $50\,\%$ should hold. As such, maximum strain values are assumed to be below 0.04.

The exact behaviour of the strain profile outside the insert is not known either. However, it is expected that the strain will relax far away from the insert, and thus provide an unstrained area. The strain measuring routines also operate under this assumption, as they use an assumed unstrained region as a comparative reference region for the strain calculations. Therefore, it is assumed that the strain values far away from the insert will be zero or close to zero. It will be seen in later sections (sections 5.3 and 5.7), that the strain might actually have a different physical behaviour than just a constant value around zero outside of the insert. However, this assumption is a starting point.

A challenge with evaluating the different experimental parameters and comparing the strain measuring routines is that there is limited information about the real value of strain in the structure. In

order to get more accurate assumptions about the behaviour of the strain profile in and around the insert, the concentration of Sb atoms could have been measured e.g. by EDX [49] or quantitative high-angle annular dark-field (HAADF) scanning transmission electron microscopy (STEM) [29]. The structure could then have been simulated in order to get more accurate information about the behaviour of the strain originating in the insert. This is a time consuming and extensive process, and was beyond the scope of this thesis.

From simply looking at the different strain maps it can be quite difficult to glean information about the actual numerical values of the strain and how it behaves throughout the NW. This becomes especially true when visually comparing similar colour maps directly. In order to make comparisons easier and based on numerical values, the analyses of the strain will be done by plotting the strain profile along a line in the y-direction of the NW, as can be seen by a blue line in Figure 5.3(a). In order to try and make the values more representative and counteract fluctuations in the data, the value of each point along the line will be an average of a number of points to the left and right of the y-direction line. For the main NW, the points along the line are averages of ten values. The plotted values along the line for the normal strain in the y-direction of the baseline case can be seen in Figure 5.3(b).
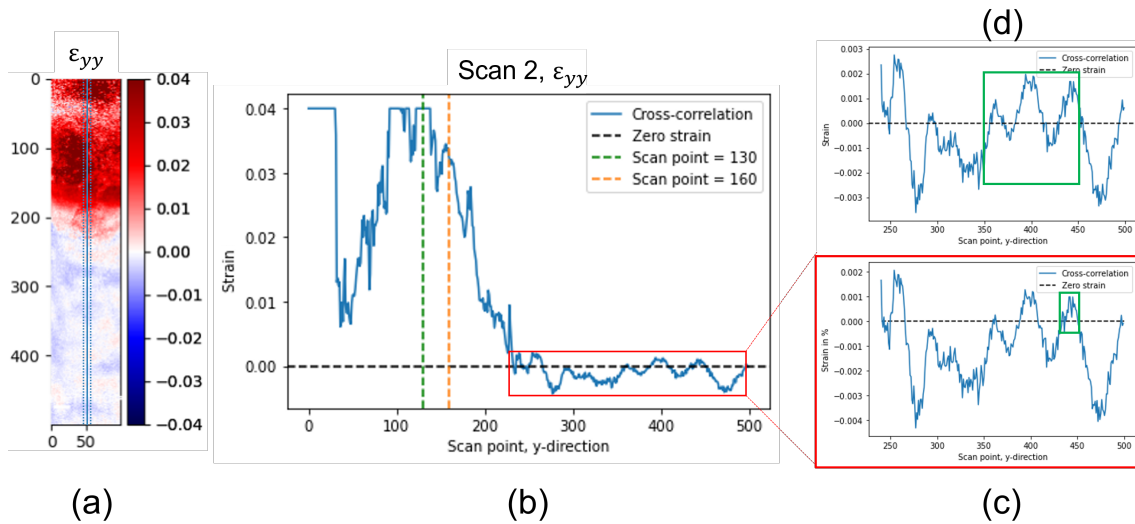
Figure 5.3: (a) Normal y-direction strain for the baseline case, scan 2, made with the cross-correlation method. The blue line indicates where the strain profile is plotted. (b) The plotted strain profile along the length of the NW. Zero strain is marked by a dashed black line. (c) Plot of the strain profile in scan points 240-500. A green square indicates the 20x20 pixel reference area. (d) Plot of the strain profile in scan points 240-500, with a reference area of 100x100 pixels. The reference area is indicated by a green square.

Because of the aforementioned assumption that the strain values will be below 0.04, strain values above 0.04 is assumed to be due to noise and not due to real values of the strain. This is supported when looking at the DPs in the points where the strain values exceed 0.04. In Figure 5.4(a), the SPED DP can be seen for scan point 130 along the line. This point is marked by a green dashed line in Figure 5.3(b), and the value of strain in this point is maxed out at 0.04. The intensities of the reflections in the DP in the corresponding scan point are very low, which makes the strain routine struggle to locate the reflection disks and it produces a much too high strain value. This low intensity can be explained by contamination of the NW sample from the convergent electron beam being placed in the same spot for a period of time. The more a NW is imaged, the more
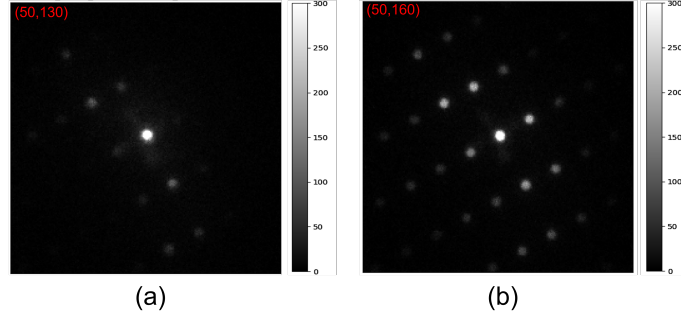
Figure 5.4: The DPs of two different points along the NW scan. (a) DP in point (50,130) in the scan. (b) DP in point (50,160). The SPED data is rotated roughly $-120°$ from the orientation of the NW in the SPED scan.

it degrades. The fact that this NW has been used for previous SPED data [45], as well as for several SPED data sets for this study, means that there is contamination build up in regions of interest, especially around the insert. The DP in Figure 5.4(b), which is taken at scan point 160 along the line, has significantly more intense reflections, and thus the routine can determine the disk positions more easily. The point is marked by an orange line in Figure 5.3(b). The value of the strain in this point is below 0.04, and fits much better with the assumptions made. Because of the presence of beam damage which negatively affects the DP peak intensities, and in order to get sensible plots, the strain values are cut-off at 0.04.

The assumptions made earlier also says that the strain values further away from the insert should go towards zero. Looking at the strain values from scan point 240 and onwards in Figure 5.3(c), the values further away from the insert are fluctuating between 0.002 and -0.004. Although there are values both above and below zero, there seems to be a negative bias, making the strain more negative than positive. The averaged DP used as a reference in the strain mapping routine is made with DPs from scan points 430-450, marked with a green square in Figure 5.3(c). These strain values are almost all located at a peak in the fluctuations, and might explain why the strain seems to have a negative bias in this region. This means that the choice of reference region for the strain mapping routines matter for the absolute values of the calculated strain. Choice of reference region for the strain mapping routines were done mostly for an arbitrary 20x20 pixel region away from the insert, based on visual inspection of the data only. In order to have more consistency in the results, some analysis could have been done before choice of reference region in order to make a similar decision for all the data sets. Both the position and the size of this reference region could affect the final results of the strain mapping. In Figure 5.3(d), the line plot of the same scan points as (c), but in this plot the reference area has been taken as a 100x100 pixel region, from 350-450 (marked by a green square). The strain profile is exactly the same, however all values are shifted slightly upward as the reference region now is not solely at one positive peak, but encapsulates both positive and negative strain values. This shows that although the choice of reference region does not have an impact on the relative strain values of a routine, it has an impact on the absolute strain values. This is something that should be taken into account when applying the strain mapping routines. In order to get consistent results, a larger reference region seems better.

5.3 Illumination for strain mapping

Comparing the resulting strain maps from the alternative experimental parameters for illumination of the sample in Figure 4.8 and 4.9 with the baseline case normal y-strain in Figure 5.1(c), it can be seen that the results are quite poor for both parameters. Firstly, considering the data set with 0° precession angle in Figure 4.8. The strain is positive where the insert is, as expected, but it quickly becomes negative outside of the insert, and fluctuates between quite negative values and zero. Looking at the averaged DP used as reference, the data might look fine, and like it should be able to produce good results. However, this is a summation of 400 DPs, and thus actually produces a more stable DP than is true for the data. When doing precession, the intensities within each disk in the DPs is effectively "integrated" over a variety of angles, and the whole DP becomes more "kinematic-like", as discussed in section 2.8.1. However, when the beam is not precessed, dynamical effects are much stronger, and this affects the intensities in the DP. Figure 5.5 shows four different DPs taken at different points in the NW. The red numbers indicate specific pixel positions in the scan. Different reflections are illuminated at different points, and even when they are illuminated, there are intensity variations throughout the disks. In some cases, this gives rise to strange, non-circular shapes, or dark lines going through the disks. This poses a big challenge for the strain mapping routine, as it is based on the assumption of circular disks that are visible in all DPs. Therefore, it can be concluded that the precession of the electron beam greatly improves the strain mapping.
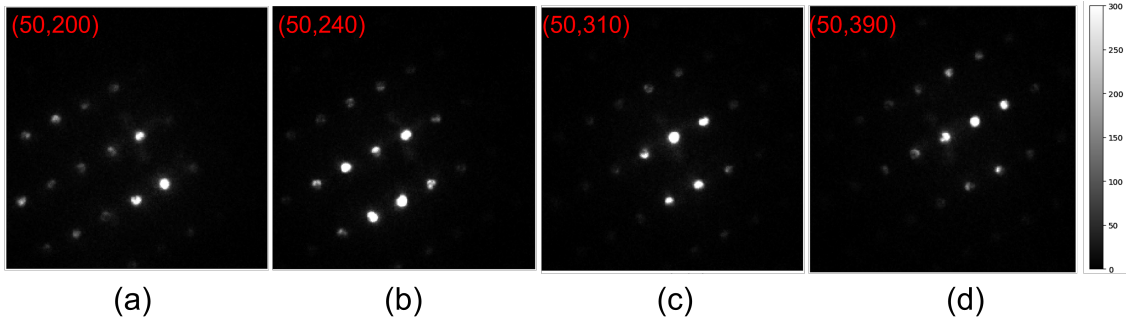
Figure 5.5: Examples of different DPs taken with a 0° precession angle at different points along the NW. Red numbers indicate the scan points in the x- and y- direction, (x,y).

Secondly, considering the data with larger convergence angle ($\alpha = 0.244$°). This map makes perhaps even less sense in accordance with the assumptions presented in section 5.2. The strain at the top of the segment is very positive, and it quickly becomes very negative, before it goes back up to very positive again. To explain this, the way the strain mapping routines work must be taken into account. The routines takes an input vector which describes the position of the DP disk, and creates a square that contains the disk. In order for the strain mapping algorithm to work, the disk must be distinguishable from the background and should have a defined shape. However, the larger convergence angle makes the reflection disks in the y-direction overlap. In order to guarantee that the whole disk is included in the square, a part of the direct beam has to be included as well. And since the direct beam has a much higher intensity than the other disks, it dominates the algorithms, and the resulting peak positions make no sense. This means that in order for the strain mapping routines to work, it is important that there is no overlap between the reflections, and they should preferably have some space between them to guarantee that only the position of one disk is evaluated at a time. The convergence angle was adjusted using a condenser AP, which gives a very course selection of convergence angles. This angle could have been adjusted

instead using the condenser mini lens, which gives a much finer adjustment, and could have given a larger disk size without overlap. However, after adjusting the mini lens, the whole microscope has to be realigned, which takes a lot of time. This study required several data sets with different experimental parameters to be collected, and therefore only the condenser AP was used to change the convergence angle. From these comparisons, it can be seen that the smallest convergence angle produces the better results for the strain mapping in the NW.

5.4   NW setup for strain mapping

The strain map from the alternative NW setup, with the insert region on zone, produces a pretty well defined y-direction strain map (Figure 5.6(a)). The insert is marked by a positive strain region, and as it moves away from the insert the strain is reduced. However, simply looking at the colour map of the strain, there seems to be some distinct values both below and above zero further away from the insert where there is expected to be less strain. There also seems to be some sort of rippling in the strain further away from the insert, with periodically spaced intensity variations following a parabolic shape. The plotted line profile along the y-direction of the strain map is presented in Figure 5.6(b). The maximum strain value is around 0.025, which fits the assumptions made of the maximum strain being below 0.04. The strain value is lower than for the other analyses, but when measuring from the lowest point below the insert to the maximum values of the insert, the difference is about equal 0.04. It also seems like the strain outliers caused by the contamination in the base line data are not present in this strain map. The reason for this could be that as the insert region is more on zone, the reflections in the DP are more intense, thus counteracting the noise introduced by the contamination. Another explanation could be that this data set is from scan 1, i.e. the first scan of the session. The longer time the electron beam is focused on a spot on the NW, the more contaminated the area becomes, and thus the smaller amount of noise may simply be because there is less contamination.

Something that is not consistent with the assumptions made about the strain profile in section 5.2, is the behaviour of the strain in the region below the insert (Figure 5.6(c)). Here, after the positive strain of the insert, the strain becomes negative, and then gradually becomes positive again. According to the assumptions, and when comparing to the other strain profiles, this strain should stabilise and fluctuate around a certain value. However, the strain seems to follow an upward trajectory, with the reference region (marked with a green square) located around zero strain. What causes this profile is uncertain, though it might be that as the insert region becomes more on zone, the reference area and the region where the expected strain is zero becomes more off zone. This could affect the strain mapping algorithms to detect a more positive strain than there really is.

As mentioned, there is some apparent rippling in the colour strain map in 5.6(a). By measuring, the ripples seem to have a periodicity of around 17 nm. Whether this is an actual behaviour of the strain in the NW, a consequence of the data collection process, or a consequence of the strain mapping algorithm is difficult to say. Visual inspection of the data does not find any grounds for this. However, the strain mapping routines calculate the strain with sub-pixel precision, and minor changes from DP to DP might be hard to see by manual inspection. Comparing with the strain maps performed with different experimental parameters for this NW, this data set seems to be the only one where the rippling is present. This suggests that maybe the effect has something to do with the data itself or the strain mapping routine, rather than actual strain in the NW. As will be seen in section 5.6, this rippling is present in all three strain mapping routine, suggesting that it might be an artefact in the data itself. However, as will be discussed in section 5.7, this

rippling effect is also present for both the +30° and −30° tilt in the strain maps for the second NW, meaning that maybe the rippling behaviour has some basis in physical strain in the NW after all. In any case, which region of the NW is on zone seems to have an effect on the detected strain profile, and thus should be chosen in regards to the region of interest.
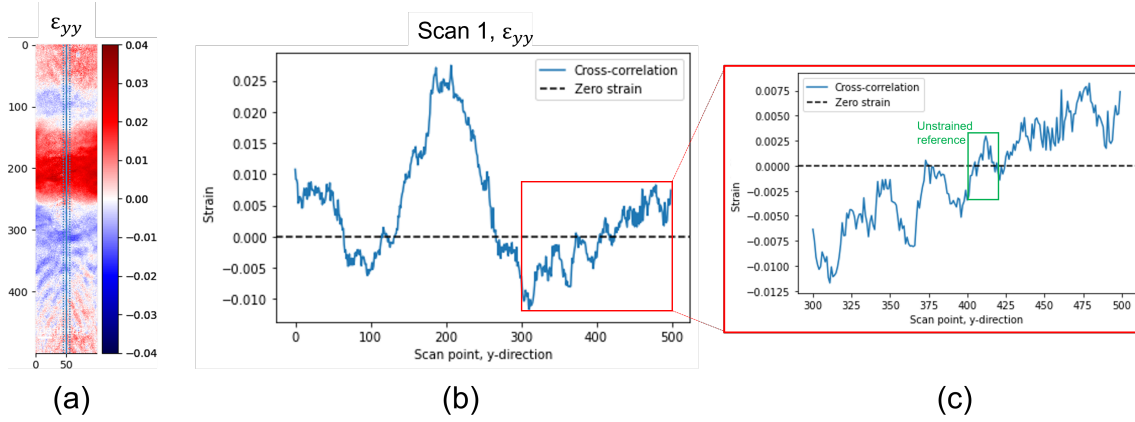
Figure 5.6: (a) Normal y-direction strain from the cross-correlation method applied on the data set with the insert on zone, scan 1. The blue line indicates where the strain profile is plotted. (b) The plotted strain profile along the length of the NW. Zero strain is marked by a dashed black line. (c) Plot of the strain profile in scan points 300-500. A green square indicates the 20x20 pixel reference area.

5.5 Post specimen settings and acquisition for strain mapping

Both strain maps from the data sets with the distinct experimental parameters related to post specimen settings and acquisition have similar strain maps to the baseline case. The strain map for the data set with 6 bit pixel depth, scan 3, can be seen in Figure 5.7(a). Just by visual inspection, this colour map is very similar to the one for the baseline case. The strain is positive in the insert region, and then tapers very quickly off to a strain that is fluctuating around/slightly above zero (between -0.001 and 0.005 strain). However, almost all of the values of the strain in the insert are maxed out at 0.04. This is especially clear when looking at the strain profile plotted along a line (Figure 5.7(b)). This goes against both the assumption that the strain in the insert is probably below 0.04, and the other strain maps, which only show this much strain in areas where the DP intensities are lowered by contamination. A possible reason for this can be found when considering the data. The SPED data is recorded using a MerlinEM direct electron detector, which records the total count of electrons hitting each pixel during the exposure time of the image. The total amount of electrons that a single pixel can detect for an image is decided by the pixel depth. With a pixel depth of 12 bit, the maximum amount of electrons each pixel can detect is equal to $2^{12} = 4096$. However, with a pixel depth of 6 bit, the maximum amount of electrons per pixel becomes $2^6 = 64$. When this limit is reached, the pixel cannot record any more electrons and it becomes oversaturated. With 4096 counts at its disposal, oversaturation is not really a problem. But, when the maximum count becomes 64, the limit is easily reached. Due to the precession of the beam, the image has to have an exposure time of minimum 10 ms, which is the time it takes for the beam to go through 360°. In that time, the pixels recording the reflections from the sample get oversaturated. This means that the peaks cut off at an intensity of 64 counts. The intensity profile plotted along a line in the DP, illustrating this point, can be seen in Figure 5.8. The strain

mapping routine is made to handle data sets of disks with highest intensity in the center, and thus it seems to struggle calculating proportional strain in the insert. Another problem with this oversaturation is that the background noise has the same intensity as for higher pixel depths, but the reflection peaks get cut off. This gives a lower signal-to-noise ratio, which makes the peaks harder to detect for the strain mapping algorithms.
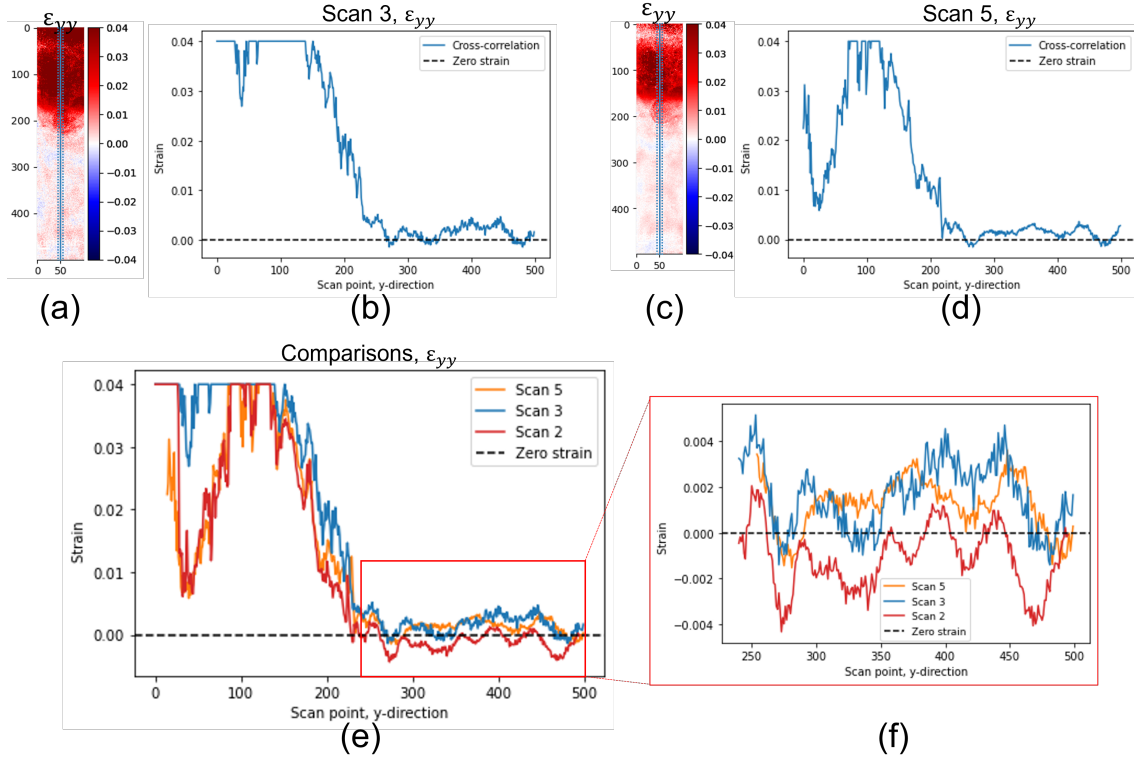

Figure 5.7: (a) Normal y-direction strain from the cross-correlation method applied on the data set with the smaller bit depth, scan 3. The blue line indicates where the strain profile is plotted. (b) The plotted strain profile along the length of the NW for scan 3. Zero strain is marked by a dashed black line. (c) Normal y-direction strain from the cross-correlation method applied on the data set with the longer camera length, scan 5. The blue line indicates where the strain profile is plotted. (d) The plotted strain profile along the length of the NW for scan 5. Zero strain is marked by a dashed black line. (e) Line profiles from the normal y-direction strain of the cross-correlation method for three different scans; 5 (orange), 3 (blue) and 2 (red). The three profiles have been lined up manually. (f) Same plot as (e), but only plotted from 240-500.

The strain map from the data set with longer camera length, scan 5 (Figure 5.7(c)), with $37.2 \, \text{cm}$ camera length versus $22.9 \, \text{cm}$ for the baseline case, is even more similar to the baseline case than the strain map for the smaller pixel depth. The strain is positive in the insert, and tapers off towards zero further away. When looking at the strain plotted in a line in Figure 5.7(d), it can be seen that the maximum values cut off at almost exactly the same place as for the baseline case, due to contamination on the NW. The variations in the region further away from the insert, where the strain is expected to be zero, the strain values are fluctuating between -0.001 and 0.004 strain. The larger camera length means that the DP has a higher magnification on the electron detector than for a lower camera length. The diameter of the reflection disks for the smaller camera length were 12 pixels, which means that each reflection disk contained $36\pi \approx 113$ pixels. For the longer

camera length, the diameter of the reflection disks were 18 pixels, which means that each reflection disk contained $81\pi \approx 254$ pixels. Thus the magnified DP due to longer camera length contained over twice as many pixels per DP reflection. Comparing the resulting strain maps with different camera lengths, however, shows that this does not make very much of a difference for the strain mapping results.
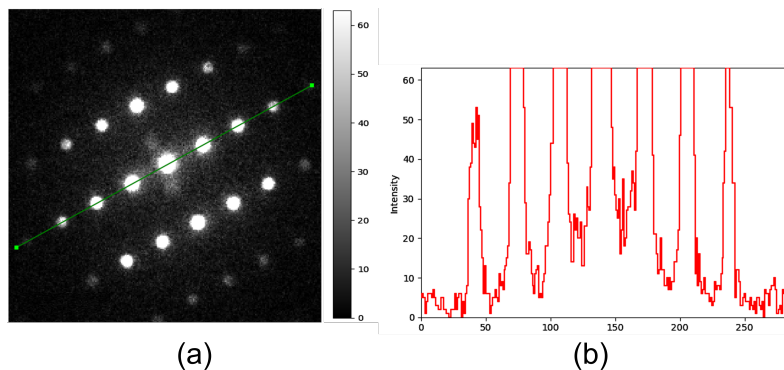
Figure 5.8: (a) SPED DP from scan 3 with 6 bit pixel depth. (b) Intensity profile is plotted along the green line in (a).

The similarities between the strain maps are especially apparent when plotting the line profiles of the strain maps from the data sets with longer camera length (scan 5), smaller pixel depth (scan 3) and the base line parameters (scan 2) in the same plot (Figure 5.7(e)). Because the scans are not taken at exactly the same places each time, the plots are offset manually in order to make them line up as well as possible. The profiles are very similar in the insert, however the strain for scan 3 has much higher values than the other two, as discussed earlier. The profiles for scan 5 and 2 are almost identical in the insert, and it seems that varying the camera length hardly influences the resulting strain maps. In the region where the strain is expected to be zero, shown closer in Figure 5.7(f), the values fluctuate within the same range of 0.005-0.006. A peculiar observation, especially for scan 3 and 2 but also for scan 5 to a degree, is that they seem to follow the same pattern, creating the same valleys and peaks in this region. Each map has been generated with different 20x20 pixel reference regions, and this similarity suggests that maybe this has something to do with the physical structure or strain of the NW, and is not just noise.

The peaks reflections used for strain measurements this study were the reflections closest to the direct beam. This was done because of bending in the NW made the closest reflections the only ones visible for a large area. However, for samples with little bending it would probably be beneficial to measure strain with peaks further out in the DP. For these reflections the distances from the central beam are greater, and thus the fractional shift in peak position due to strain will result in a larger absolute shift. Larger shifts are more easily detected by the strain mapping algorithms. When the DP is more magnified due to larger camera length, the field of view decreases and limits the choice of reflections that can be used for strain mapping. Therefore, even though change in camera length has little impact on the strain mapping results, it might be beneficial to use a smaller camera length. It should be considered, however, that the larger the angle of a reflection, the fewer electrons are scattered there, and going too far from the central beam might cause signal-to-noise problems.

5.6 Data processing for strain mapping

In addition to evaluating the effects of different experimental parameters, three different strain mapping routines have been applied to the data sets. In order to compare these routines with each other, strain mapping has been performed on the same regions in the same scans, with the same areas used as reference. The first set of strain maps for comparison are the strain maps made for the baseline case of scan 2. The results for the cross-correlation method has already been discussed in section 5.2, and were found to be pretty good. The strain profiles for the three methods are plotted (along the green lines in the colour maps) in Figure 5.9(a). Because it is desirable to compare the same regions for all three methods, only a region of about 100x300 pixels from the bottom of the insert and downwards is analysed. This is because the Gaussian method requires clear data with a high signal-to-noise ratio in all scan points. Due to the contamination on the insert discussed previously, this is not the case for the insert region. Therefore, the Gaussian method is unable to produce results for most of the insert region, and the comparisons has to be done below the insert. Because of this, in scan 2 it is difficult to comment on whether the maximum value of strain calculated by the routines fits the assumptions made in 5.2 about the strain being below 0.04. However, general comparisons and conclusions can be made on the behaviour of the strain calculated by the different routines in the area with assumed low values of strain.

The first thing that is apparent, even when looking at only the colour maps, is that the cross-correlation and center of mass method produce very similar results with strain that quickly goes down to zero further away from the insert. The Gaussian method, however, seems to produce much more negative results in this region, which can also be seen when looking at the plotted line profile. The cross-correlation (blue) and center of mass (red) plots follow each others behaviour very closely, only deviating slightly in values at a couple scan points. The Gaussian (orange) plot, on the other hand, fluctuates a lot from these values. Where the other two methods have a minimum strain value of -0.005 and fluctuate up to 0.002 in the region where the strain is assumed to be zero, the Gaussian method has a minimum strain value of -0.015 and fluctuates up to 0.003 in the same region. Although the variations in the Gaussian plot are more extreme, they seem to follow the same pattern as the plots for the other two routines. All three plots have valleys and peaks in the same scan points, which suggests that these variations are not introduced by the routines themselves, but actually based on changes present in the data. From the strain plots done for the base line case of scan 2, it looks like the cross-correlation and center of mass methods are most suited for the data.

The second set of strain maps for comparison are the strain maps made from the data of scan 4, which was collected without precession of the electron beam. As discussed in section 5.3, using unprecessed data creates unstable DPs with intensity variations inside the reflection disks. This poses a big challenge for the strain measuring routines, and the resulting maps become quite unreliable. Because of the large intensity variations in the data, the Gaussian method is unable to create strain maps at all, and thus only the cross-correlation and center of mass method can be compared for this data set. The region analysed is 100x500 pixels from the insert and downwards, and the plotted line profile for both methods is presented in Figure 5.9. The strain inside the insert is positive, and there is a clear divide between the insert and the rest of the NW. This is consistent with what has been observed for the other data sets. The strain values inside the insert are exceeding 0.04 for the cross-correlation method, but does not for the center of mass method. Thus, it can seem like the contamination that causes very positive values in the cross-correlation method does not have the same effect in the center of mass method. Other than this, the profiles are very similar, especially for the profile in the region further away from the insert where the strain is assumed to be zero. In this region, the values vary between -0.02 for the cross-correlation
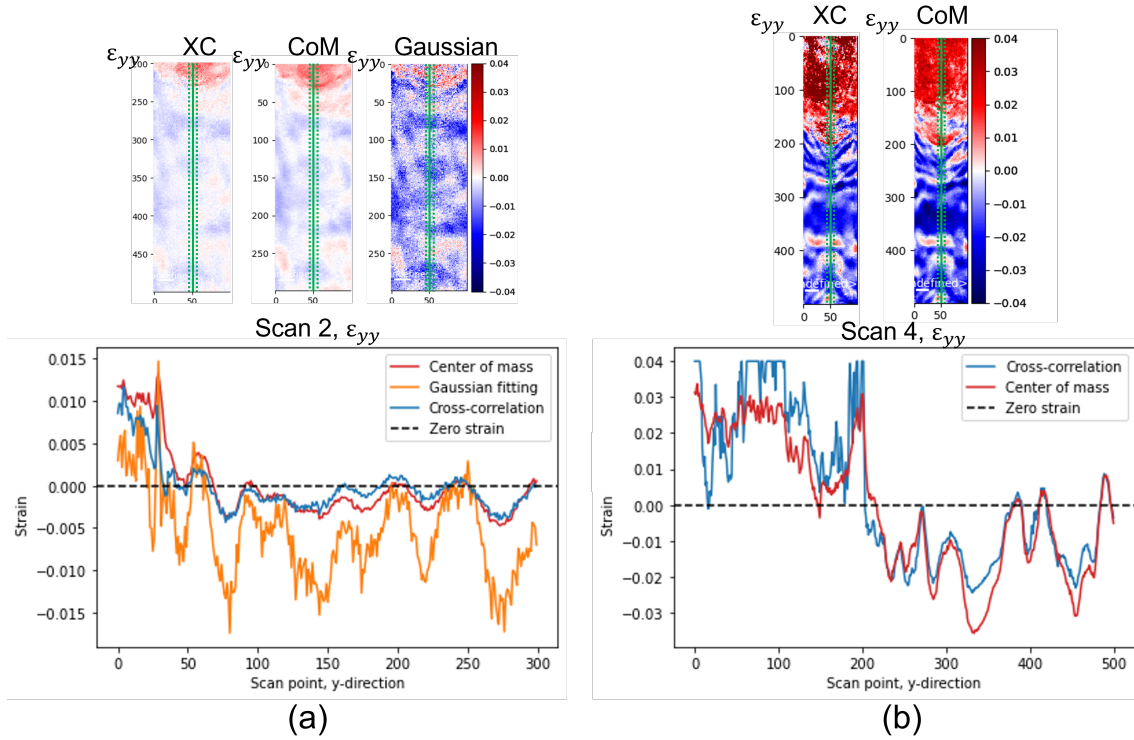
Figure 5.9: (a) Strain maps and plotted line profiles for all three strain mapping routines for the baseline case, scan 2. (b) Strain maps and plotted line profiles for the cross-correlation and the center of mass method for the unprecessed data set, scan 4.

and -0.03 for the center of mass, and 0.01 for both. This suggests that the data is not reliable, as the deviations from what is the assumed strain, i.e. zero, are almost as large as the positive strain values detected in the insert. However, again we observe that the two routines produce strain with very similar behaviour, which suggest that the variations are a consequence of variations in the data and not in the routines. From the comparisons of the strain maps for scan 4, it can seem like the center of mass method is less affected by contamination, but the data is too unreliable due to the intensity variations to draw conclusions from this data set alone.

The third set of strain maps for comparisons are the strain maps made from the data of scan 1, which was collected with the insert on zone. In order to get a comparable region for all three routines, the strain mapping routines were performed on a region of 100x300 pixels at the insert and below. For this scan, as discussed in section 5.3, the effects of the contamination were less severe, which meant that also the Gaussian method could be performed for the region containing the insert. Looking at the colour maps of the strain in Figure 5.10(a), it is clear that there is positive strain in the insert, which fits with the assumptions made. However, the values are varying between the routines. Looking at the line plots, it can be seen that the cross-correlation (blue) and Gaussian fitting (orange) methods have very similar strain values inside the insert. The peak value is around 0.03 for both of them, which fits well with the assumptions made about the strain. The center of mass method, on the other hand, barely has strain values above 0 in the insert, and the maximum values are below 0.01. Judging from strain maps from other parameters and routines, it seems like the cross-correlation and Gaussian fitting methods have more accurate values inside the insert.

As was discussed in section 5.3, the strain map from the cross-correlation method seemed to have some sort of rippling in the region further away from the insert. Looking at the colour maps from the other two in Figure 5.10(a), this rippling seems to be present for the other two methods as well. This suggests that it is an effect that is present in the data, and not an artefact of the strain mapping routines. Comparing the line plots of the strain from the three routines in this area, there is some discrepancy in the plots. The center of mass method follow about the same pattern as the cross-correlation method, but is shifted downwards to more negative strain. For scan points further away from the insert, the strain becomes more and more positive, until the cross-correlation and center of mass method line up like they have done for scan 2 and 4. The Gaussian method also follows roughly the same pattern, with peaks and valleys in the same places as cross-correlation and center of mass, but the values fluctuate a lot more, between positive strain of 0.005 and negative strain of around -0.015. In both the cross-correlation and center of mass method, the strain seems to go from negative values just below the insert, and then gradually increase further away. The variations in the Gaussian method, on the other hand, seem to fluctuate around the same values further away from the insert. The only noticeable change might be that the negative strain values in the valleys gradually gets more positive, from -0.015, to -0.01, to -0.005 further away from the insert, while the peaks stay at 0.005. It is difficult to determine a cause for the apparent increase in strain further away from the insert other than what was discussed in section 5.3. For this scan, it seems like the cross-correlation and Gaussian fitting methods give the most accurate strain value in the insert, while the cross-correlation and center of mass have the least fluctuations in the region further away from the insert.

The fourth set of strain maps for comparisons are the strain maps made from the data of scan 5 with longer camera length. The comparable region for the three strain mapping routines was 100x350 pixels, and extended a little further into the insert region than the comparisons for the baseline case. The strain colour maps as well as the line profile strain plots from scan 5 are presented in Figure 5.10(b). In section 5.5, it was concluded that the difference between the strain maps obtained with cross-correlation with varying camera lengths were not significant. Comparing the equivalent strain maps from the center of mass method, this also seems to be the case, although it is difficult to say without the strain profile in the insert for comparisons. The Gaussian fitting, method however, which seemed to have a negative bias in the region far away from the insert in scan 2, seems to have a positive bias in the same region for scan 5. This bias probably has to do with where the reference region is set, which has an effect on the strain values, as we have seen in section 5.2. In scan 2, the reference region contains scan points 230-250, which coincides with a peak in the strain line profile in Figure 5.9(a). In scan 5, the reference region contains scan points 310-330, which coincides with a valley in the strain line profile. The other two methods have values that fluctuate within a range of 0.006, and therefore this does not make much of a difference. However, the strain from the Gaussian method fluctuates within a range of 0.015-0.02. This means that the difference between having the reference coincide with a peak or a valley could shift the whole strain profile with half of the maximum strain expected in the insert.

When taking into account the comparisons of routines for the four different parameters, it can seem like the cross-correlation method is the one that works best with the S(P)ED data sets generated from the GaAsSb NW. The Gaussian method has large variations in strain in areas where it is assumed to be zero, and this can affect the total value of the strain by quite a lot. Therefore, even though it can seem like the Gaussian fitting method gives a good representation in areas with definite strain, it seems to struggle with areas where there is assumed little to no strain. In addition, the Gaussian fitting method is the strain mapping routine that is the most vulnerable to noise in the data (in this study from contamination on the insert), which greatly limits the area it can be used on. Thus, this is the least suitable routine for the data sets in this thesis. Better results
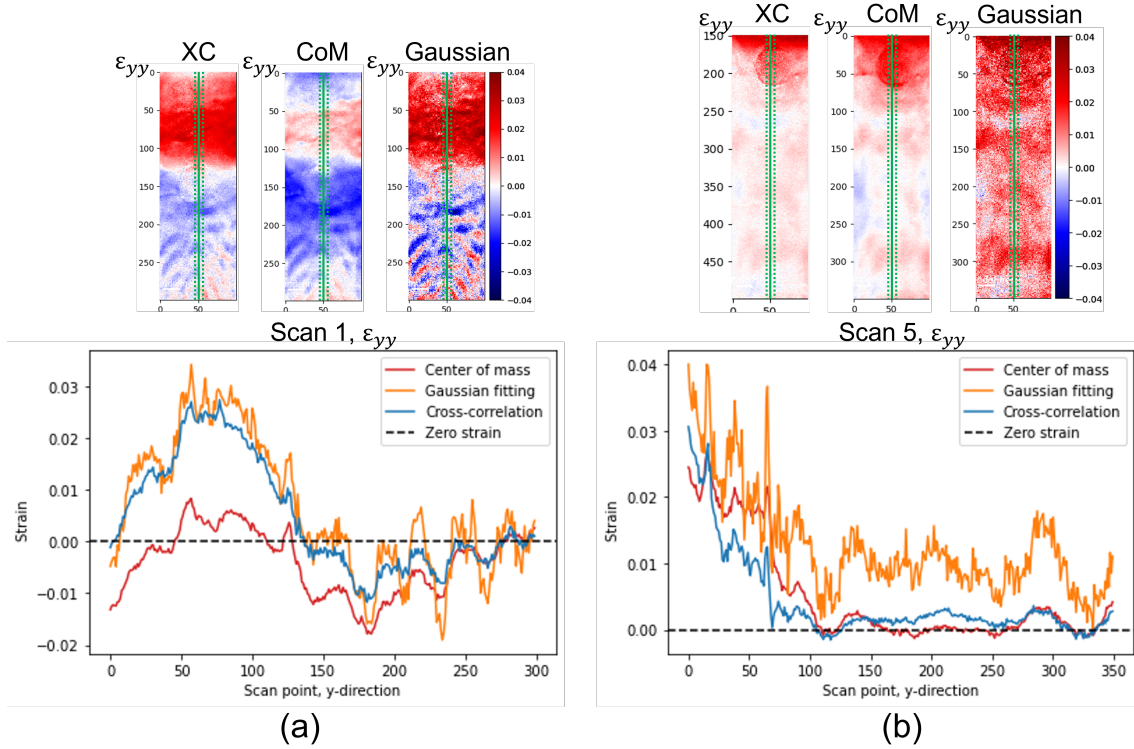
Figure 5.10: (a) Strain maps and plotted line profiles for all three strain mapping routines for the data set with the insert on zone, scan 1. (b) Strain maps and plotted line profiles for all three strain mapping routines for the data set with the longer camera length, scan 5.

for the Gaussian fitting method could perhaps be achieved if the data had been pre-processed, e.g. with background subtraction or other noise reduction methods, before strain mapping was performed. This was not explored with the data from scan 1-6, as the other two methods produced sensible results without it. The center of mass method seemed to produce pretty similar results to the cross-correlation method, and it could seem like this method was the least vulnerable to noise in the data due to contamination on the sample. However, it did not hold up as well when the insert was on zone, suggesting that it might be vulnerable to more off zone reference regions. As such, the cross-correlation method seems to be the routine that produced the most robust results matching the assumptions made. However, it should be noted that the cross-correlation tends to generate too high strain values when signal-to-noise ratio is low due to contamination.

5.7 Second NW

The data of the second NW was taken with the same experimental parameters as the baseline case (scan 2) for the main NW. As discussed in the previous sections, the data of scan 2 had the parameters that overall created the best strain maps according to the assumptions made. It is then interesting to see if these conclusions hold when considering another NW, i.e. how general the observations and conclusions are. From visual inspection of the colour maps in Figure 4.19-4.21, it seems like the strain mapping routines work equally well with these experimental parameters for a second NW. This suggests that the effects of the experimental parameters on the strain measurements are not NW specific, but can be generalised to other NWs with the same

heterostructure.

The strain analysis of the second NW was done for three different tilts in order to investigate what effect the 3D shape of the NW has on the strain. As mentioned in section 2.9, the strain is a 3D tensor. However, measuring the strain in 3D is a complicated process that requires very specific setups (e.g. for X-rays [54]). Collecting S(P)ED data is a much simpler process, but the data only gives a 2D projection of the reciprocal lattice structure, and thus only the 2D projection of the strain can be calculated. Strain tomography, i.e. collecting series of 2D projections and reconstructing the 3D tensor has been suggested as a solution to this [55], but it is a very involved process and will not be done in this thesis. As the NWs are 3D objects with a hexagonal cross-section, it is interesting to examine whether the chosen zone axis has an effect on the resulting strain map. The SPED data from the 0° rotation of the NW, i.e. the $[1\,\overline{1}\,0]_{ZB}$ orientation, corresponds to imaging the NW through the hexagonal face of the NW (see Figure 2.13(a)). Looking at the colour maps of the three different strain mapping routines in Figure 5.11(a), it can seem like they all produce pretty similar results. This is evident when looking at the line plots of the strain profiles in 5.11(b), in which we see that the lines behave almost identically. For the main NW, the strain plotted along the line was an average of 10 scan points, while for this NW only 4 scan points were used per point in the plot. This was because the NW is thinner, and also each scan point has a larger size than for the main NW, i.e. 1.684 nm/pixel (calibrations in Appendix A.4). The strain values are positive in the insert, and then go down towards zero further down, away from the insert. By looking at the colour maps, lines in the x-direction of more positive strain can be seen. These are features that can be seen in all three scans, which suggests that there is evidence for it in the data. Comparing the Gaussian fitting method for this NW with the profiles for the main NW, it can seem like the Gaussian fitting routine produces much more robust results for this NW. Using data from the second NW, the Gaussian fitting method produces a profile that matches the two other routines. For the main NW, on the other hand, the values fluctuated a lot more for the Gaussian fitting method than for the other two routines. For all the data sets from the second NW, data pre-processing was performed in the form of background subtraction. This was not done for the main NW. Looking at the results, it seems like the Gaussian method benefits greatly from this processing.

The maximum values of the strain in the insert are just above 0.04 for the center of mass method and the Gaussian fitting, while the cross-correlation method produces strain values of around 0.035. From this it seems like the concentration of Sb atoms in the insert of this NW is slightly higher than for the main NW. Which one of them that is closest to the actual strain value is hard to tell, but if the assumption is that the strain is below 0.04 as was stated in section 5.2, the cross-correlation produces most fitting values. Looking at the colour maps, the strain looks symmetric in this orientation.

Comparing the strain map for the 0° tilt with the strain map for the Nw tilted +30° to the $[2\,\overline{1}\,\overline{1}]_{ZB}$ orientation in Figure 5.12(a) (which corresponds to imaging the NW through the hexagonal vertex, see Figure 2.13(b)), it is obvious that the 3D shape of the NW has an impact on the measured strain. Where the strain colour maps for the 0° rotation has features that looks like horizontal lines, the colour maps for the y-direction strain in the +30° rotation has the same rippling features as was seen in the strain maps from scan 1 (Figure 5.10(a)). Because this effect is present for all three strain mapping routines, and both NW, this suggests that it actually might be a physical strain in the NW. As this is not visible in the strain maps for the second NW in the $[1\,\overline{1}\,0]_{ZB}$ orientation, it might be an effect that is only visible when collecting data with the zone axis through an hexagonal vertex of the NW. This makes sense, as when the NW is imaged through the $[1\,\overline{1}\,0]_{ZB}$ zone axis, the surface is flat and the projected NW has an even thickness for most of the projection. In
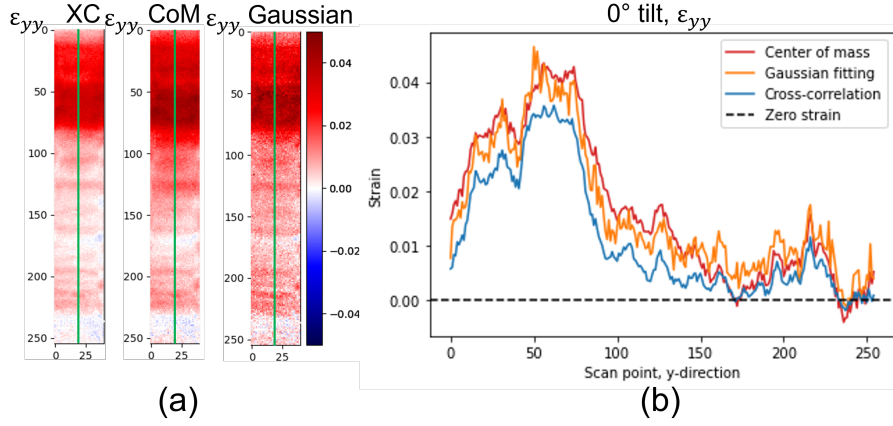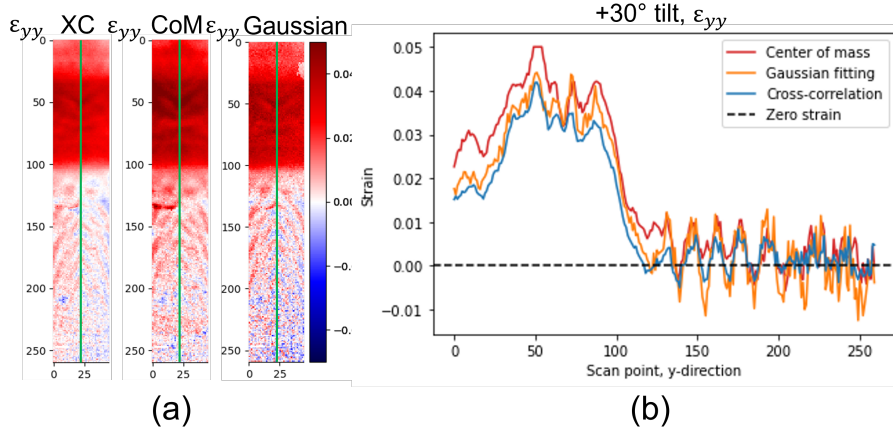
Figure 5.11: (a) Normal y-direction strain maps from all three strain mapping routines for the data set taken from the $[1\,\overline{1}\,0]_{ZB}$ orientation at 0° tilt. (b) Plotted line profiles for all three strain mapping routines along the green lines in (a). Red is center of mass, orange is Gaussian fitting, and blue is cross-correlation.

addition, the area used for strain mapping is selected such that the edges of the NW are not in the scan. This means almost the whole strain map from the $[1\,\overline{1}\,0]_{ZB}$ orientation is from the part of the NW with even thickness. However, when the NW is imaged through its the $[2\,\overline{1}\,\overline{1}]_{ZB}$ zone axis, the NW surfaces are declining from the middle, and it has the largest thickness in the middle on the NW projection. This might be what gives rise to the contours that look like rippling in the strain maps. It might also explain why the rippling is symmetric about a line down the middle of the NW, as the shape of the NW is symmetric about this line as well. The rippling in the strain could, however, be real strain variations, as it is consistent in all the analyses of the $[2\,\overline{1}\,\overline{1}]_{ZB}$ and $[2\,1\,1]_{ZB}$ orientations. For the $[1\,\overline{1}\,0]_{ZB}$ orientation, only the center of the NW is used, which means that there is little information on the strain at the hexagonal vertices, which may explain why this rippling effect is only visible for the ±30° tilts. Further, it can be seen that the ripples decrease to the facet average further away from the insert, which means that they cannot be explained as method artefacts. As such, it could be real strain in the NW, but more work and closer study would be needed in order to come to an accurate conclusion.

The behaviour the strain profiles for the three different routines, illustrated in the line plot in Figure 5.12, are also very similar for this data set. Again, it seems like the cross-correlation method produces the smallest strain value in the insert, which has a maximum value around 0.04, while the center of mass method has a maximum strain value of 0.05. The Gaussian method also has maximum strain values around 0.04, but produce a little higher strain values overall. The strain further away from the insert is oscillating around zero for all the values, with a periodicity that matches the ripples in the colour maps. Again, it can be seen that the Gaussian method produce results that have the highest peaks and the lowest valleys in the region further from the insert, ranging from -0.01 to +0.01, while the strain from the center of mass method ranges from -0.005 to 0.01, and the cross-correlation ranges from -0.005 to 0.005. However, their profiles are a lot more similar for the second NW than for the main NW, and it seems like the only differences between the three are the numerical values for the strain. Looking at the colour maps, there seems to be a higher value of strain on the left side of the map, causing a slight asymmetry in the strain.

Only the cross-correlation and center of mass method produced results for the third data set from the second NW. This was because limitations of the holder meant that the NW could not
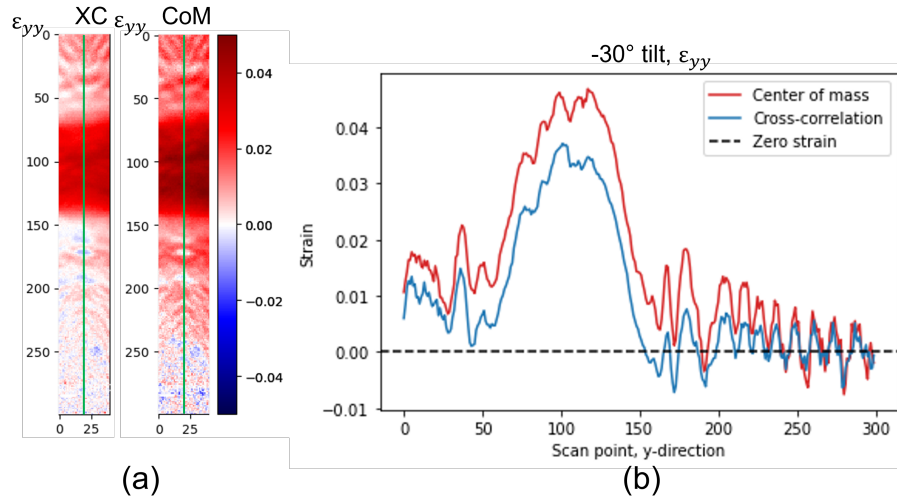
Figure 5.12: (a) Normal y-direction strain maps from all three strain mapping routines for the data set taken from the $[2\,\overline{1}\,\overline{1}]_{ZB}$ orientation at $+30°$ tilt. (b) Plotted line profiles for all three strain mapping routines along the green lines in (a). Red is center of mass, orange is Gaussian fitting, and blue is cross-correlation.

be completely tilted to the $[2\,1\,1]_{ZB}$ orientation, making the DPs slightly off zone. Even though the reflections in the y-direction (i.e. $(1\,1\,1)_{ZB}/(\overline{1}\,\overline{1}\,\overline{1})_{ZB}$) were clear and defined, the spots in the x-direction (i.e. $(0\,\overline{2}\,2)_{ZB}/(0\,2\,\overline{2})_{ZB}$) were not, which caused trouble for the Gaussian fitting methods. Since only the normal strain in the y-direction is used for analysis in this study, the undefined peaks in the x-direction should not affect the results of the two remaining routines too much.

The resulting strain maps from the $-30°$ NW tilt to near the $[2\,1\,1]_{ZB}$ (Figure 5.13(a)) are very similar to the strain maps for the $+30°$ NW tilt. The strain maps for the $-30°$ tilt extend into the WZ region as well, because the mapped region is not limited by the Gaussian method for comparison. The same rippling effects can be seen in the colour maps for both $\pm30°$ tilts, and for the $-30°$ tilt it can be seen that this rippling is present in the WZ as well as the ZB. When looking at the line plots for the two routines in Figure 5.13(b), they too have a very similar behaviour, much like for the other two data sets. Again, the cross-correlation seems to produce a smaller value of strain in the insert region than the center of mass method, while the values coincide further away from the insert. The same oscillations around zero with pretty much the same periodicity as for the $+30°$ NW tilt are found in the region further away from the NW. The same asymmetry with slightly more positive strain to one side can also be seen for this orientation, but this time with a slightly more positive right side. The $-30°$ NW tilt data set was taken with a precession angle of $1°$ instead of $0.5°$ in an attempt to increase the field of view in the DPs. Comparing the resulting strain maps with the ones created with a smaller precession angle, it does not look like the precession angle parameter above $0.5°$ is relevant for strain analysis as done here (i.e. using a limited region of the NW and the reflections closest to the direct beam).

All in all, it seems like the 3D shape of the NW (i.e. which zone axis is used, and how the NW is projected) does have an effect on the resulting strain maps. This especially applies to collecting data from zone axes where the NWs have a different projected geometry, such as the $[1\,\overline{1}\,0]_{ZB}$ zone axis, which is through the hexagonal face of the NW, and the $[2\,\overline{1}\,\overline{1}]_{ZB}$ zone axis, which is through the hexagonal vertex of the NW. Slight asymmetry is observed in strain maps generated from data collected from zone axes where the projected geometry is the same, but it is only slight, and thus it should not matter too much whether the NW is rotated $+$ or $-30°$ from the $[1\,\overline{1}\,0]_{ZB}$

Figure 5.13: (a) Normal y-direction strain maps from all the cross-correlation and the center of mass method. The data set is taken near the $[2\,1\,1]_{ZB}$ orientation at -30° tilt. (b) Plotted line profiles for both of the strain mapping routines along the green lines in (a). Red is center of mass and blue is cross-correlation.

zone axis. The conclusions made about the strain mapping routines for the main NW seems to hold when applied to a second NW. However, it seems that the Gaussian fitting method works better on this data set than the ones for the main NW. A reason for this may be that the second NW had not been subject for S(P)ED data collection before (i.e. has experienced a much lower electron beam dosage). This meant that there was less beam damage and contamination on the NW, which resulted in data sets with higher signal-to-noise ratios. In addition, data pre-processing such as background subtraction was applied to the data sets from the second NW before the strain mapping. This seemed to greatly improve the robustness of the Gaussian fitting method, and should be considered if that is the desired routine to be used.

6 Conclusion

The aim of this study was to compare different S(P)ED based strain measuring routines, for different experimental collection parameters, and identify which routine and parameters are most suited and accurate for strain measurements with nm-scale spatial resolution. This was done by gathering scanning diffraction data from a GaAs NW with an axially inserted heterostructure of GaAsSb. Both conventional TEM (for structural characterisation) and S(P)ED were performed. The NW had a hexagonal cross-section, with a growth direction along the $[1\,1\,1]_{ZB}/[0\,0\,0\,1]_{WZ}$ direction. The analysis was done both through the hexagonal face, i.e. along the $[1\,\overline{1}\,0]_{ZB}/[2\,\overline{1}\,\overline{1}\,0]_{WZ}$ zone axis, and tilted 30° around the growth direction, through the hexagonal vertex, i.e. along the $[2\,\overline{1}\,\overline{1}]_{ZB}/[1\,0\,\overline{1}\,0]_{WZ}$ zone axis. In order to determine crystal phases and structure, TEM techniques such as BF and DF imaging, SAED and HRTEM were used. This needs to be done at the $[1\,\overline{1}\,0]_{ZB}/[2\,\overline{1}\,\overline{1}\,0]_{WZ}$ orientation, as there the different crystal phases are distinguishable. The NW was found to be in the ZB crystal phase at and below the ZB GaAsSb insert, and in the WZ crystal phase above it, which confirms earlier studies. In addition, twinning of the ZB GaAs phase was observed. Out-of-plane bending of the NW is limiting the area for which strain analysis can be done. S(P)ED data was gathered mainly from the $[2\,\overline{1}\,\overline{1}]_{ZB}/[1\,0\,\overline{1}\,0]_{WZ}$ orientation of the NW, as the DPs in this orientation appears the same for both crystal phases present in the wire, and rectangular patterns makes assigning the x- and y-directions of the strain routines obvious. The experimental parameters such as convergence angle, pixel depth and whether precession was applied were found to affect the final strain map. Three different strain mapping routines from the Python library pyXem; cross-correlation, center of mass and Gaussian fitting, were then applied to the diffraction data, in order to test which parameters and routines produce the optimal results.

A comparison was done between the strain analysis done on the same NW in a previous thesis using a Stingray optical camera, and the strain analysis performed in this thesis using a MerlinEM direct electron detector. It was determined that the data gathered with the new direct electron detector had a superior signal-to-noise ratio and produced more stable strain mapping results. Care has to be taken in order not to saturate the DP reflections when collecting the diffraction data, for example by collecting data at too low bit depth (i.e. using 6 bit pixel depth instead of 12 bit), in order to create good strain maps. It was also established that the choice of averaged reference region used in the strain mapping routines had an impact on the specific numerical values of the strain, but not on the actual strain profile. Ideally the reference region should be relatively large (in order to have a good signal-to-noise ratio), with minimal variations. It should also be on zone, and thus taken as near the region of interest as it is probable to expect zero strain in order to reduce effects of bending.

It was found that data sets that had been gathered using precession and a convergence angle where the reflection disks of the DP did not overlap could produce sensible strain maps. Which region was put on zone when setting up the NW had a distinct impact on the resulting strain maps, and should be carefully considered, especially when the specimen is bending. Variations in the strain that looked like "ripples" with periodicity of around 17 nm were observed for different experimental settings with the insert aligned on the $[2\,\overline{1}\,\overline{1}]_{ZB}$ zone for all three routines. Although not previously been reported, these variations might actually be a physical effect of the NW being imaged through the hexagonal vertex (i.e. along the $[2\,\overline{1}\,\overline{1}]_{ZB}/[1\,0\,\overline{1}\,0]_{WZ}$ zone axis). The same rippling effect was observed in another studied NW. Variations in camera length was found to not have much significance for the strain mapping results for the three tested routines.

The comparisons between the three strain mapping routines for the NWs showed that the cross-correlation and center of mass method often produced similar results. However, the center of

mass method seems to be sensitive to which region is on zone, and the cross-correlation, although seeming more robust, often produces a lower strain value. The Gaussian method produced sensible strain behaviour inside the insert when it could be applied to the data, but showed much larger variations (i.e. low precision) in the regions assumed to be unstrained. All three methods showed similar strain profiles, with peaks and valleys in the plotted lines at the same positions along the NW. Hence, this suggests that all three pick up on the changes in the data, but with different precision. The Gaussian fitting method was also limited by the quality of the data. The diffraction data (i.e. the sharpness of the pattern) could be degraded by the presence of carbon build-up contamination or beam damage.

The strain mapping routines were verified on a second NW in order to confirm the conclusions made with the main NW are generic. The second NW was thin (106 nm in diameter), and had higher detected strain values. This second NW was used to investigate the influence of the 3D shape of the NW on the 2D projection of the strain. Because these data sets were collected with another software (Topspin instead of the ASTAR software), the data needed additional pre-processing; the data was converted to logarithmic scale and background subtraction was performed. This, in combination with the reduced thickness and minimal contamination on the second NW increasing the signal-to-noise ratio, greatly improved the strain results from the Gaussian fitting method. All three methods produced very similar strain maps. It was found that the 3D geometry of the NW did have an effect on the strain mapping, most notably differing in strain maps made from data along the $[1\,\overline{1}\,0]_{ZB}$ zone axis (through the hexagonal face of the NW) and along the $[2\,\overline{1}\,\overline{1}]_{ZB}$ zone axis (through the hexagonal vertex of the NW). In the strain maps from the $[1\,\overline{1}\,0]_{ZB}$ zone axis, the fluctuations in strain seemed to move in horizontal lines (i.e. perpendicular to the growth direction) and the strain was symmetric, while in the maps from the $[2\,\overline{1}\,\overline{1}]_{ZB}$ zone axis, the strain seemed to have the same parabolic rippling behaviour as found for the data with the insert on zone for the main NW, and seemed to be slightly asymmetric. Strain routines applied on data gathered from similar projected geometries, such as the $[2\,\overline{1}\,\overline{1}]_{ZB}$ and $[2\,1\,1]$ orientations (NW tilted + and -30° from the hexagonal face respectively), seemed to produce similar strain maps as well. Both showed a slight asymmetry in the data, but with more positive strain at opposite edges.

In conclusion, strain mapping based on SPED data collected with a direct electron detector and using open-source routines can be used for strain analysis on the nm-scale, and produce better results than with old detector technology (i.e. optical imaging of the fluorescent viewing screen). The possibility of collecting many, robust DPs using SPED is very useful when analysing strain in a structure. The fact that one data set can be used with several different strain mapping routines is very advantageous and makes S(P)ED data collection an valuable asset. However, it is important to gather the data with experimental parameters that are as optimal as possible for the intended use of the data set. When calculating strain in a NW, SPED data with small enough convergence angle to avoid disk overlap in the DP and sufficient pixel depth seem to produce the most accurate results. The cross-correlation method seems to produce the most robust strain results when sample contamination contribute to low signal-to-noise ratio, but for less noisy data improved by background subtraction the three different routines produced very similar results. The 3D geometry of the NW affects the measured 2D strain projection, and thus the orientation of the NW for strain analysis should be chosen with care.

7 Future work

7.1 Strain analysis with theoretical comparisons

The accuracy of the strain analyses computed by the routines in this study was judged based on assumptions on how the strain would behave in the heterostructured NWs. Specifically, an unstrained area was assumed and set as "ground-truth". These assumptions were made based on previous analysis by conventional TEM (section 4.1) and studies of similar NWs [49], and thus were not specific for the individual NW analysed. Using the unstrained area as indicator to evaluate the precession and accuracy of the developed strain analysis is an approach also used by others [9]. In order to make more definitive conclusions about the strain mapping results of the different routines and parameters, more information about the strain behaviour in the particular NW is required. The strain findings should be analysed by other methods, however for example lattice based analysis [8] can only be performed for a very limited area, and no biprisms were available to apply off-axis holography [29] to analyse a similarly large area as studied here. It could therefore be beneficial to do a study in which the theoretical strain of the structure is known using modelling, for example finite elements (FE). An initial FE model for comparison was made by Johnstone [55]. To do this for the GaAsSb NW it is needed to measure the fraction and profile of Sb in the GaAsSb insert, either by EDX (as done in [49]) or by HAADF STEM (as done in [29]). A theoretical model of the NW lattice structure behaviour around the insert region could then be calculated and the induced strain in the ZB GaAs modelled. This could also be done for the WZ GaAs side of the insert, but this would require that the elastic modulus for the WZ, which is only found in NWs, is known. From strain contrast in conventional TEM the extent of the strain area in WZ GaAs seems smaller than for ZB. Assuming the Sb profile in the insert is symmetric (which is not true [49]), this could indicate that elasticity modulus for WZ GaAs is larger then for the well known ZB GaAs phase. Having a known strain behaviour in the NW could improve analysis with respect to the accuracy of both the measured values of strain in the insert region, and the strain behaviour outside of the NW insert.

7.2 Other materials

In this thesis, the analysis of strain has been performed on heterostructured GaAsSb NWs. This was done because the NWs are intrinsically electron transparent due to their size, and therefore the strain levels would not be affected by thinning preparations done to achieve electron transparency. Furthermore, the heterostructures introduce a qualitatively known strain into the NWs. However, strain at the nm-scale is a property that is a crucial characteristic for many structures, and thus the developed analysis routines would be of interest to extend to other structures. An example of structures where analysis of strain could be useful are thin films. A thin film is limited in thickness, and thus has the potential to be analysed using S(P)ED. The 2D structure of the thin film could also potentially mean that bending is not as an acute problem as for NW, leading to potentially large areas of strain analysis. Preliminary data sets were gathered from an Al thin film with various precipitates. It is assumed that some of the precipitates would introduce strain into the Al lattice, which should be possible to analyse using the same routines and methods as for the NWs. The general strain mapping routines seemed to be working, and a preliminary set of strain maps from the center of mass method can be seen in Figure 7.1 for a 100x100 scan of the Al thin film. However, further systematic method development routines are required. For example, the fine details of the patterns such as contrast, signal-to-noise ratio or intensity variations within the

discs could be different than observed for the NWs. These signal characteristics affect the three strain algorithms in different ways than is demonstrated in the present study.
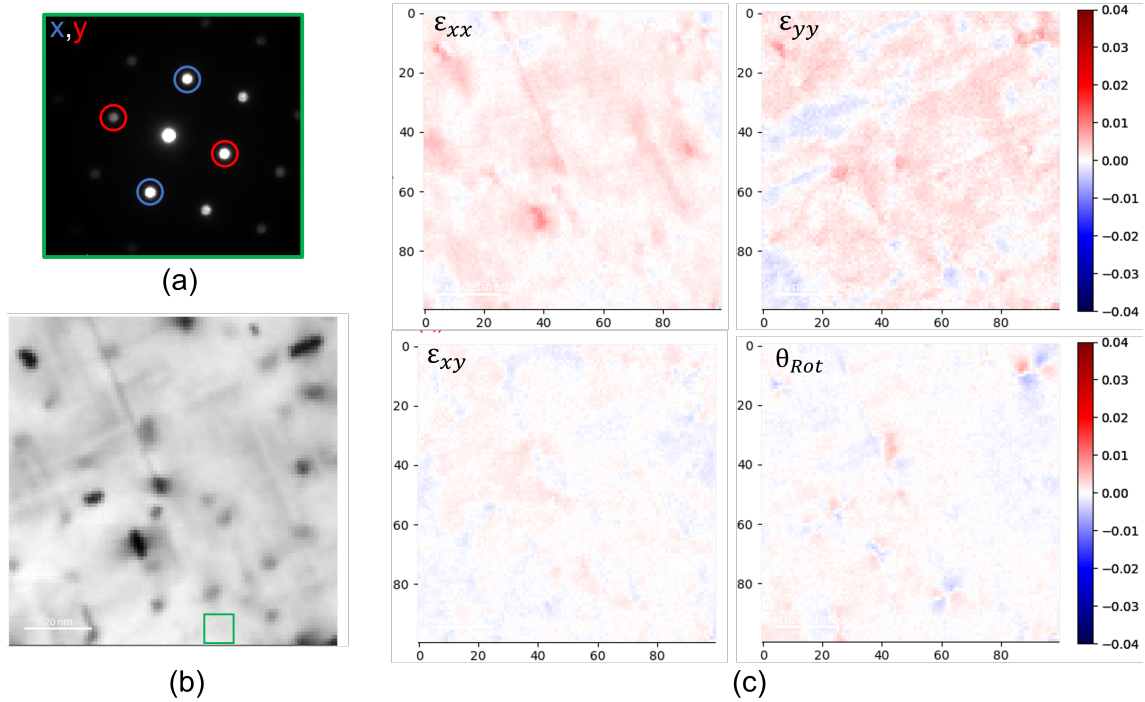
Figure 7.1: Preliminary strain mapping results done on SPED data from an Al thin film with precipitates. (a) Averaged SPED DP from the reference region, with reflections for x- and y-direction marked by blue and red circles. (b) VBF image of the sample, with reference region marked by a green square. (c) A set of strain maps from the center of mass method.

7.3   Determination of 3D strain

As mentioned in the thesis, the analysis of the strain in this study is of the 2D projection of the strain. This is because the DPs generated with S(P)ED are 2D projections themselves, and thus it is difficult to gather anything from the 3D structure from one data set. In order to calculate the 3D strain, SPED data would have to be collected in a tilt series for multiple angles. The 3D strain field could then be constructed using all the 2D strain maps for each angle. This is an extensive process, and would require much study. An initial demonstration of this has been done by D. Johnstone *et.al* [55], and it would be an interesting matter to investigate. That 3D strain mapping is one of the main targets within the field of TEM can be concluded from the research targets set in a big European consortium of leading TEM facilities where NTNU participates (Milestones and deliverables of work package 4 of ESTEEM3 [56])

Bibliography

[1] I. N. Prestholdt, *Semiconductor nanowire characterization based on scanning electron diffraction*. Project thesis, NTNU, 2020.

[2] G. Yeap *et al.*, "5nm CMOS Production Technology Platform featuring full-fledged EUV, and High Mobility Channel FinFETs with densest 0.021 μm SRAM cells for Mobile SoC and High Performance Computing Applications," in *2019 IEEE International Electron Devices Meeting (IEDM)*, 2019.

[3] S. Yang, C. Wang, H. Sahin, H. Chen, Y. Li, S.-S. Li, A. Suslu, F. M. Peeters, Q. Liu, J. Li, and S. Tongay, "Tuning the optical, magnetic, and electrical properties of ReSe$_2$ by nanoscale strain engineering," *Nano Letters*, vol. 15, pp. 1660–1666, 2015.

[4] M. Chu, Y. Sun, U. Aghoram, and S. E. Thompson, "Strain: A solution for higher carrier mobility in nanoscale MOSFETs," *Annual Review of Materials Research*, vol. 39, pp. 203–229, 2009.

[5] S. Kumar, R. Trotta, E. Zallo, J. D. Plumhof, P. Atkinson, A. Rastelli, and O. G. Schmidt, "Strain-induced tuning of the emission wavelength of high quality GaAs/AlGaAs quantum dots in the spectral range of the ^{87}Rb D$_2$ lines," *Applied Physics Letters*, vol. 99, 2011.

[6] R. Bierwolf, M. Hohenstein, F. Phillipp, O. Brandt, G. Crook, and K. Ploog, "Direct measurement of local lattice distortions in strained layer structures by HREM," *Ultramicroscopy*, vol. 49, pp. 273–285, 1993.

[7] P. L. Galindo, S. Kret, A. M. Sanchez, J.-Y. Laval, A. Yáñez, J. Pizarro, E. Guerrero, T. Ben, and S. I. Molina, "The peak pairs algorithm for strain mapping from HRTEM images," *Ultramicroscopy*, vol. 107, pp. 1186–1193, 2007.

[8] M. Hÿtch, E. Snoeck, and R. Kilaas, "Quantitative measurement of displacement and strain fields from HREM micrographs," *Ultramicroscopy*, vol. 74, pp. 131–146, 1998.

[9] A. Béché, J. Rouvière, J. Barnes, and D. Cooper, "Strain measurement at the nanoscale: Comparison between convergent beam electron diffraction, nano-beam electron diffraction, high resolution imaging and dark field electron holography," *Ultramicroscopy*, vol. 131, pp. 10–23, 2013.

[10] D. B. Williams and C. B. Carter, *Transmission electron microscopy*. Springer, 2009.

[11] L. Jones, S. Wenner, M. Nord, P. H. Ninive, O. M. Løvvik, R. Holmestad, and P. D. Nellist, "Optimising multi-frame ADF-STEM for high-precision atomic-resolution strain mapping," *Ultramicroscopy*, vol. 179, pp. 57–62, 2017.

[12] A. Béché, J. Rouvière, J. Barnes, and D. Cooper, "Dark field electron holography for strain measurement," *Ultramicroscopy*, vol. 111, pp. 227–238, 2011.

[13] P. Zhang, A. A. Istratov, E. R. Weber, C. Kisielowski, H. He, C. Nelson, and J. C. H. Spence, "Direct strain measurement in a 65 nm node strained silicon transistor by convergent-beam electron diffraction," *Applied Physics Letters*, vol. 89, 2006.

[14] J. M. Zuo and J. C. Spence, *Advanced Transmission Electron Microscopy: Imaging and Diffraction in Nanoscience*. Springer New York, 2016.

[15] V. B. Ozdol, C. Gammer, X. G. Jin, P. Ercius, C. Ophus, J. Ciston, and A. M. Minor, "Strain mapping at nanometer resolution using advanced nano-beam electron diffraction," *Applied Physics Letters*, vol. 106, 2015.

[16] W. Sinkler and L. D. Marks, "Characteristics of precession electron diffraction intensities from dynamical simulations," *Zeitschrift für Kristallographie - Crystalline Materials*, vol. 225, 2010.

[17] R. Vincent and P. Midgley, "Double conical beam-rocking system for measurement of integrated electron diffraction intensities," *Ultramicroscopy*, vol. 53, pp. 271 – 282, 1994.

[18] E. F. Rauch, J. Portillo, S. Nicolopoulos, D. Bultreys, S. Rouvimov, and P. Moeck, "Automated nanocrystal orientation and phase mapping in the transmission electron microscope on the basis of precession electron diffraction," *Zeitschrift für Kristallographie - Crystalline Materials*, vol. 225, pp. 103 – 109, 2010.

[19] J. L. Rouviere, A. Béché, Y. Martin, T. Denneulin, and D. Cooper, "Improved strain precision with high spatial resolution using nanobeam precession electron diffraction," *Applied Physics Letters*, vol. 103, 2013.

[20] Y. Zhang, J. Wu, M. Aagesen, and H. Liu, "III-V nanowires and nanowire optoelectronic devices," *Journal of Physics D: Applied Physics*, vol. 48, 2015.

[21] T. J. Kempa, R. W. Day, S.-K. Kim, H.-G. Park, and C. M. Lieber, "Semiconductor nanowires: a platform for exploring limits and concepts for nano-enabled solar cells," *Energy & Environmental Science*, vol. 6, pp. 719–733, 2013.

[22] P. Krogstrup, H. I. Jørgensen, M. Heiss, O. Demichel, J. V. Holm, M. Aagesen, J. Nygard, and A. F. i Morral, "Single-nanowire solar cells beyond the Shockley–Queisser limit," *Nature Photonics*, vol. 7, p. 306–310, 2013.

[23] H. Riel, L.-E. Wernersson, M. Hong, and J. A. del Alamo, "III-V compound semiconductor transistors - from planar to nanowire structures," *MRS Bulletin*, vol. 39, pp. 668–677, 2014.

[24] Z. Liu, W. Ma, and X. Ye, "Chapter 2 - shape control in the synthesis of colloidal semiconductor nanocrystals," in *Anisotropic Particle Assemblies* (N. Wu, D. Lee, and A. Striolo, eds.), pp. 37–54, Elsevier, 2018.

[25] C. P. Kuo, S. K. Vong, R. M. Cohen, and G. B. Stringfellow, "Effect of mismatch strain on band gap in III-V semiconductors," *Journal of Applied Physics*, vol. 57, pp. 5428–5432, 1985.

[26] L. Li, D. Pan, Y. Xue, X. Wang, M. Lin, D. Su, Q. Zhang, X. Yu, H. So, D. Wei, B. Sun, P. Tan, A. Pan, and J. Zhao, "Near full-composition-range high-quality $GaAs_{1-x}Sb_x$ nanowires grown by molecular-beam epitaxy," *Nano Letters*, vol. 17, pp. 622–630, 2017.

[27] H. J. Joyce, Q. Gao, H. Hoe Tan, C. Jagadish, Y. Kim, J. Zou, L. M. Smith, H. E. Jackson, J. M. Yarrison-Rice, P. Parkinson, and M. B. Johnston, "III–V semiconductor nanowires for optoelectronic device applications," *Progress in Quantum Electronics*, vol. 35, pp. 23 – 75, 2011.

[28] R. Teissier, D. Sicault, J. C. Harmand, G. Ungaro, G. Le Roux, and L. Largeau, "Temperature-dependent valence band offset and band-gap energies of pseudomorphic GaAsSb on GaAs," *Journal of Applied Physics*, vol. 89, pp. 5473–5477, 2001.

[29] T. Grieb, F. F. Krause, M. Schowalter, D. Zillmann, R. Sellin, K. Müller-Caspary, C. Mahr, T. Mehrtens, D. Bimberg, and A. Rosenauer, "Strain analysis from nano-beam electron diffraction: Influence of specimen tilt and beam convergence," *Ultramicroscopy*, vol. 190, pp. 45–57, 2018.

[30] D. N. Johnstone, P. Crout, M. Nord, J. Laulainen, S. Høgås, E. Opheim, B. Martineau, T. Bergh, C. Francis, S. Smeets, E. Prestat, A. Ross, S. Collins, I. Hjorth, Mohsen, T. Furnival, D. Jannis, E. Jacobsen, A. Herzing, T. Poon, H. W. Ånes, J. Morzy, T. Doherty, A. Iqbal, T. Ostasevicius, M. von Lany, and R. Tovey, "pyxem/pyxem: pyxem 0.13.0," Jan. 2021.

[31] C. Kittel, *Introduction to Solid State Physics*. John Wiley & Sons, Inc, 8 ed., 2005.

[32] F. C. Frank, "On miller-bravais indices and four-dimensional vectors," *Acta Crystallographica*, vol. 18, pp. 862 – 866, 1965.

[33] L. Kantorovich, *Quantum Theory of the Solid State: An Introduction*. Kluwer Academic, 2004.

[34] M. I. McMahon and R. J. Nelmes, "Observation of a wurtzite form of gallium arsenide," *Phys. Rev. Lett.*, vol. 95, 2005.

[35] P. Caroff, K. A. Dick, J. Johansson, M. E. Messing, K. Deppert, and L. Samuelson, "Controlled polytypic and twin-plane superlattices in III–V nanowires," *Nature Nanotechnology*, vol. 4, pp. 50–55, 2009.

[36] M. D. Graef, *Introduction to conventional transmission electron microscopy*. Cambridge University Press, 2003.

[37] V. Senez, A. Armigliato, I. De Wolf, G. Carnevale, R. Balboni, S. Frabboni, and A. Benedetti, "Strain determination in silicon microstructures by combined convergent beam electron diffraction, process simulation, and micro-raman spectroscopy," *Journal of Applied Physics*, vol. 94, pp. 5574–5583, 2003.

[38] B. Warren, *X-ray diffraction*. New York: Dover Publications, 1990.

[39] J. C. Slater, "Atomic radii in crystals," *The Journal of Chemical Physics*, vol. 41, pp. 3199–3204, 1964.

[40] E. Hecht, *Optics*. Pearson custom library, Pearson Education, 2013.

[41] P. E. Anuta, "Spatial registration of multispectral and multitemporal digital imagery using fast Fourier transform techniques," *IEEE Transactions on Geoscience Electronics*, vol. 8, 1970.

[42] M. Guizar-Sicairos, S. T. Thurman, and J. R. Fienup, "Efficient subpixel image registration algorithms," *Opt. Lett.*, vol. 33, pp. 156–158, Jan 2008.

[43] A. M. Munshi, D. L. Dheeraj, J. Todorovic, A. T. van Helvoort, H. Weman, and B. O. Fimland, "Crystal phase engineering in self-catalyzed GaAs and GaAs/GaAsSb nanowires grown on Si(111)," *Journal of Crystal Growth*, vol. 372, pp. 163 – 169, 2013.

[44] H. Kauko, B. O. Fimland, T. Grieb, M. Munshi, K. Müller, A. Rosenauer, and A. T. J. van Helvoort, "Near-surface depletion of antimony during the growth of GaAsSb and GaAs/GaAsSb nanowires," *Journal of Applied Physics*, vol. 116, 2014.

[45] T. I. Thorsen, *Heterostructured GaAs/GaAsSb nanowires characterized by scanning precession electron diffraction*. Master's thesis, NTNU, 2020.

[46] K. Momma and F. Izumi, "Vesta: A three-dimensional visualization system for electronic and structural analysis," *Journal of Applied Crystallography*, vol. 41, pp. 653–658, 2008.

[47] J. Schindelin, C. T. Rueden, M. C. Hiner, and K. W. Eliceiri, "The ImageJ ecosystem: An open platform for biomedical image analysis," *Molecular Reproduction and Development*, vol. 82, pp. 518–529, 2015.

[48] A. D. Darbal, R. D. Narayan, C. Vartuli, T. Aoki, J. Mardinly, S. Nicolopoulos, and J. K. Weiss, "Applications of automated high resolution strain mapping in TEM on the study of strain distribution in MOSFETs," *Microscopy and Microanalysis*, vol. 20, p. 1066–1067, 2014.

[49] J. Todorovic, H. Kauko, L. Ahtapodov, A. F. Moses, P. Olk, D. L. Dheeraj, B. O. Fimland, H. Weman, and A. T. J. van Helvoort, "The effects of Sb concentration variation on the optical properties of GaAsSb/GaAs heterostructured nanowires," *Semiconductor Science and Technology*, vol. 28, 2013.

[50] Z. Yuan and A. Nakano, "Self-replicating twins in nanowires," *Nano Letters*, vol. 13, pp. 4925–4930, 2013.

[51] J. Todorovic, *Correlated transmission electron microscopy and micro-photoluminescence studies of GaAs-based heterostructured semiconductor nanowires.* PhD thesis, NTNU, 2012.

[52] I. MacLaren, E. Frutos-Myro, D. McGrouther, S. McFadzean, J. K. Weiss, D. Cosart, J. Portillo, A. Robins, S. Nicolopoulos, E. Nebot del Busto, and R. Skogeby, "A comparison of a direct electron detector and a high-speed video camera for a scanning precession electron diffraction phase and orientation mapping," *Microscopy and Microanalysis*, vol. 26, p. 1110–1116, 2020.

[53] J. Jeong, N. Cautaerts, G. Dehm, and C. H. Liebscher, "Automated crystal orientation mapping by precession electron diffraction assisted four-dimensional scanning transmission electron microscopy (4D-STEM) using a scintillator based CMOS detector," 2021.

[54] M. O. Hill, I. Calvo-Almazan, M. Allain, M. V. Holt, A. Ulvestad, J. Treu, G. Koblmüller, C. Huang, X. Huang, H. Yan, E. Nazaretski, Y. S. Chu, G. B. Stephenson, V. Chamard, L. J. Lauhon, and S. O. Hruszkewycz, "Measuring three-dimensional strain and structural defects in a single InGaAs nanowire using coherent x-ray multiangle bragg projection ptychography," *Nano Letters*, vol. 18, pp. 811–819, 2018.

[55] D. N. Johnstone, A. T. J. van Helvoort, and P. A. Midgley, "Nanoscale strain tomography by scanning precession electron diffraction," *Microscopy and Microanalysis*, vol. 23, p. 1710–1711, 2017.

[56] European Network for Electron Microscopy, "ESTEEM3." https://www.esteem3.eu.

Appendix

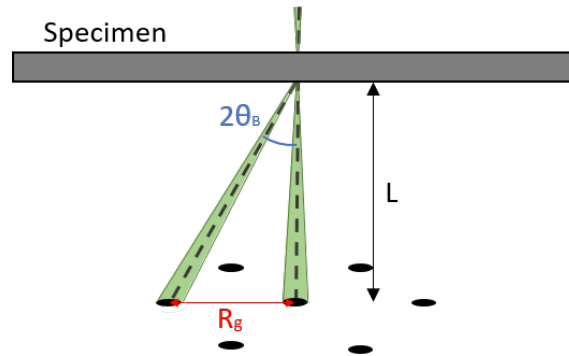## A SED/SPED calibration

A.1 Diffraction

The scale of the DPs taken at camera length 22.9 cm and 37.2 cm has been calculated by using the DP from the ZB region of the main NW oriented at the $[2\,\overline{1}\,\overline{1}]$ zone axis. The distance from the central beam to a 111 reflection was measured to be 32 pixels for a camera length of 22.9 cm, and 52 pixels for a camera length of 37.2 cm. The reciprocal distance between the peaks was found from equation 2.8 to be $0.3064\,\mathring{A}^{-1}$. This gives the calibration values of $0.009\,57\,\mathring{A}^{-1}$/pixel for the 22.9 cm camera length, and $0.005\,89\,\mathring{A}^{-1}$/pixel for the 37.2 cm camera length.

A.2 Camera length, L

Calculating the camera length is a matter of trigonometry. From Figure A1, it can be seen that $R_g = Ltan(2\theta_B)$. From Braggs law, equation 2.9, we know that $\lambda = 2dsin(\theta_B)$, and since θ_B is very small, we can approximate $2sin(\theta_b) \approx 2\theta_b \approx 2tan(\theta_B)$. Thus the equation to find the camera length, L, becomes

$$L = \frac{R_g d}{\lambda} \tag{A1}$$

R_g can be calculated by considering from the detector specifications, which says that one pixel equals 55 µm. d can be calculated from equation 2.2, and the wavelength λ for electrons accelerated by a voltage of 200 kV is about 2.508 pm. The SED/SPED was performed with given camera lengths in the instrument software of 12 cm and 20 cm. However, calculation from equation A1 finds the true camera lengths to be 22.9 cm and 37.2 cm respectively.

Figure A1: Figure of the measurements needed for camera length calibration.
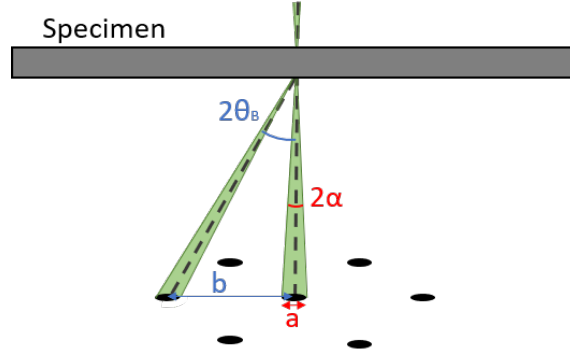
A.3 Convergence angle, α

The electron beam used in SED/SPED measurements is not parallel, but has a convergence angle α, as can be seen in Figure A2. The value of this angle can be found by measuring the diameter

a of the diffraction disks, the distance between them b, and using the equation

$$2\alpha = 2\theta_B \frac{a}{b} \tag{A2}$$

θ_B can be found from Braggs law (equation 2.9) for a given reflection. The data was taken with two differently sized condenser APs, with the smallest resulting in a condenser angle of $\alpha_1 = 0.07693°$, and the bigger one resulting in a condenser angle of $\alpha_2 = 0.2442°$.

Figure A2: When the electron beam is focused on the sample with a convergence angle α, it results in reflections with a diameter a and distance b between them.

A.4 Scan (nm/pixel)

The size of each pixel in the S(P)ED scan was calibrated for each NW separately by measuring the NW diameter in data gathered from conventional TEM, and then measuring the diameter in pixels in the corresponding S(P)ED scan. For the main NW with data sets scan 1-6, the diameter in the $[2\,\bar{1}\,\bar{1}]_{ZB}$ orientation was measured to be 131.4 nm in conventional TEM, and 129 pixels in the S(P)ED data for scan 2. Thus, the resulting scan calibration was calculated to be 1.019 nm/pixel. For the second NW, the diameter in the $[1\,\bar{1}\,0]_{ZB}$ was measured to be 106.1 nm in conventional TEM and 63 pixels in the S(P)ED data for the same orientation. Thus, the resulting scan calibration was calculated to be 1.684 nm/pixel.

B Jupyter Notebook

Strain mapping

Import pyxem and required libraries

```python
# For external figs
%matplotlib tk

# Div packages
import pyxem as pxm
import numpy as np
import hyperspy.api as hs
from matplotlib import pyplot as plt
from pathlib import Path


# For strain mapping
from pyxem.generators.subpixelrefinement_generator import↵
 ↪SubpixelrefinementGenerator
from pyxem.signals.tensor_field import *
from pyxem.generators.displacement_gradient_tensor_generator import *
```

Self-made functions for easier strain mapping and use of multiple reflection peaks

```python
#Choosing which subpixelgenerator method to use, either center of mass ('com')↵
 ↪or conventional cross correlation ('xc')
def SubPixGen(subpixgen,method,values):
    if method == 'com':
        return subpixgen.center_of_mass_method(values[0])
    elif method == 'xc':
        return subpixgen.conventional_xc(values[1][0],values[1][1],values[1][2])
    else:
        print('Put in either com or xc')
        return 0


#Subtracting two opposite y peaks to create one long y vector, countering drift↵
 ↪effects in the y-direction
def subtract_yvecs(peak_array):
    fdarray = np.asarray(peak_array)
    arr_dim = len(fdarray.shape)

    if arr_dim == 2:
        correct_array = np.asarray([fdarray[0],fdarray[1]-fdarray[2]])

    elif arr_dim == 4:
        i_length = len(fdarray)
```

```
            j_length = len(fdarray[0])
            correct_array = np.full((i_length,j_length,2,2),0.0)

            for i in range (i_length):
                    for j in range(j_length):
                        x,y_plus,y_minus = fdarray[i][j][0], fdarray[i][j][1],⌴
 ↪fdarray[i][j][2]

                        correct_array[i][j][0] = x
                        correct_array[i][j][1] = y_plus - y_minus

        else:
            print('You have to put in an array of the correct dimensions.')
            correct_array = [0,0]

        return correct_array



    #Combining opposite x and y peaks in order to counter drift effects
    def drift_correction(peak_array):
        fdarray = np.asarray(peak_array)
        arr_dim = len(fdarray.shape)

        if arr_dim == 2:
            correct_array = np.asarray([fdarray[0]-fdarray[1],fdarray[2]-fdarray[3]])

        elif arr_dim == 4:
            i_length = len(fdarray)
            j_length = len(fdarray[0])
            correct_array = np.full((i_length,j_length,2,2),0.0)

            for i in range (i_length):
                    for j in range(j_length):
                        x_plus,x_minus,y_plus,y_minus = fdarray[i][j][0],⌴
 ↪fdarray[i][j][1], fdarray[i][j][2], fdarray[i][j][3]
                        correct_array[i][j][0] = x_plus - x_minus
                        correct_array[i][j][1] = y_plus - y_minus
        else:
            print('You have to put in an array of the correct dimensions.')
            correct_array = [0,0]

        return correct_array
```

Load data

```
filename = './data/20210310/scan2_100x500(50-150_200-700).hspy'
```

```
s = hs.load(filename, lazy=False)
```

0.0.1 Preprocessing for Topspin data

Convert the data to log scale and perform background removal

```
[ ]: #Convert the data to log scale (in a figure you can convert to log scale by␣
     ↪pressing the 'l' key)
     s.data = np.where(s.data > 0, np.log(s.data),0)

     #Background removal
     s = s.subtract_diffraction_background('difference of␣
     ↪gaussians',min_sigma=3,max_sigma=10)
     s.compute()
     s.set_signal_type('electron_diffraction')
```

0.0.2 Vector Based strain mapping

Peaks found manually

```
[ ]: #Maunally located reference peaks for NW1 Scan 2 peak vectors, ref [40:60,430:
     ↪450]
     a1 = [-52.05,-32.92]
     a2 = [-23.44,-48.93]
     a3 = [5.973,-65.05]
     b1 = [-27.02,14.02]
     center = [0.952,-1.512]
     b3 = [30.55,-16.91]
     c1 = [-2.48,61.49]
     c2 = [26.04,46.03]
     c3 = [55.45,30.52]

     method_values = [18,[26,5,20]] #[com values, cross-correlation values], 26,0.35␣
     ↪for Gaussian fitting
```

```
[ ]: #Make position finding easier by setting diffraction calibration to 1
     s.set_diffraction_calibration(1)

     #Define which peaks will be used for the strain mapping
     x_plus = a2
     x_minus = c2
     y_plus = b1
     y_minus = b3
     method = 'xc' #Input either 'xc' or 'com', depending on what method you want to␣
     ↪use

     two_peaks = [x_plus,y_plus]
```

78

```
three_peaks = [x_plus,y_plus,y_minus]
peaks = [x_plus,x_minus,y_plus,y_minus]
```

Define, and manually find the reference peak positions from average DP from reference region

Create average DP of a reference region, e.g. 20x20 pixels:

```
[ ]: s_ref = s.inav[40:60,430:450]
     s_refm = s_ref.mean((0,1))
```

Plot DP and manually locate the peak positions

```
[ ]: s_refm.plot(vmax=500)
```

Find peak positions with sub-pixel precision in the reference region, using one of the three peak finding routines; Center of mass, cross-correlation or Gaussian fitting

```
[ ]: spg_ref = SubpixelrefinementGenerator(s_refm, np.asarray(peaks))

     #For center of mass or cross-correlation, use:
     vector_ref = SubPixGen(spg_ref,method,method_values)

     #For Gaussian fitting use:
     #vector_ref = spg_ref.fitting_gaussians_method(26, intensity_ratio=0.30)
```

Depending on the number of peaks chosen, use one of these to combine the ones that need combining:

```
[ ]: Vs_ref = drift_correction(vector_ref)   #Combining two peaks in both x and y.
     #Vs_ref = subtract_yvecs(vector_ref)    #Assuming you only have one x-peak,␣
     ↪commbining two y-peaks
     #Vs_ref = np.asarray(vector_ref)        #Assuming you only have one peak in x and␣
     ↪y, two peaks total
```

Choose region for strain mapping

```
[ ]: s1 = s.inav[0:45,0:300]
     s1.change_dtype('float64')
     s1
```

Determine peak positions to subpixel precision for the rest of the data, using one of the three methods; Center of mass, cross-correlation or Gaussian fitting

```
[ ]: spg = SubpixelrefinementGenerator(s1, np.asarray(peaks))

     #For center of mass or cross-correlation, use:
     peak_vectors = SubPixGen(spg,method,method_values)

     #For Gaussian fitting use:
```

```
#peak_vectors = spg.fitting_gaussians_method(26, intensity_ratio=0.30)
```

Depending on the number of peaks chosen, use one of these to combine the ones that need combining:

```
[ ]: Vs = drift_correction(peak_vectors)      #Combining two peaks in both x and y.
     #Vs = subtract_yvecs(peak_vectors)        #Assuming you only have one x-peak,␣
      ↪commbining two y-peaks
     #Vs = peak_vectors                        #Assuming you only have one peak in x and␣
      ↪y, two peaks total
```

Compare distorted and undistorted diffraction vectors to obtain a strain map

```
[ ]: D = get_DisplacementGradientMap(hs.signals.Signal2D(Vs), Vs_ref)

     strain_map = D.get_strain_maps()

     strain_map.plot(cmap='seismic',vmax=0.04,vmin=-0.04)
```

Save the strain map

```
[ ]: strain_map.save('./data/Strain_maps/NW1/Scan2_strain-map_xc)
```

C Abstract

Two-Dimensional Strain Mapping by Scanning Precession Electron Diffraction: Experimental Set-up and Data Analysis

Dipanwita Chatterjee[1], Ingeborg Nævra Prestholdt[1], P. Crout[2], Tor Inge Thorsen[1], P. A. Midgley[2] and Antonius T. J. van Helvoort[1]

[1] Department of Physics, Høgskoleringen, Norwegian University of Science and Technology, Trondheim, Norway

[2] Department of Materials Science and Metallurgy, University of Cambridge, 27 Charles Babbage Road, Cambridge, CB3 0FS, UK

Abstract:

Strain is important for tailoring the properties in functional and engineering materials. For strain analysis with high spatial resolution i.e., beyond that of standard X-ray and scanning electron microscopy-based techniques, transmission electron microscopy (TEM) is required. Several strain measurement techniques are available within the domain of TEM but scanning (precession) electron diffraction (SED/SPED) is generally seen to be one of the most convenient [1,2]. This is because it is an easy technique to set up at the microscope without any special hardware configuration. Once set up, the data acquisition is fast and robust analysis can be automated. S(P)ED based mapping can have both nm scale spatial resolution and a relatively large field of view, as opposed to the measurements made using lattice imaging methods. Precession improves the robustness of the technique and the accuracy of data analysis. In the recent years, two major developments to SED/SPED based techniques have emerged: i) improved electron detection (i.e., the use of the direct electron detectors) and ii) advances in post-processing methodologies. These two factors, together with the electron beam/probe set-up strongly influence the accuracy and precision of strain mapping at the nm-scale.

In this contribution, we investigate the influence of these factors on the resulting strain maps. We do this by systematically adjusting (i) the beam/probe configuration (for example, use of probe precession, beam convergence angle), (ii) the detection parameters (for example, pixel size and pixel depth) and (iii) the analysis algorithms (namely, cross-correlation, centre of mass method and Gaussian peak-fitting). A well-characterized GaAs nanowire with a GaAsSb insert has been used as a test object [3] for this purpose. The data processing has been carried out with the python-based open-source library pyxem [4] and we include the applied data processing routines.

Comparison of the constructed strain maps under varying set-ups shows that the three elements, mentioned above are interdependent. We do however find trends that aid us in identifying the optimum probe settings for achieving accurate strain maps. For all the analyses, the bending of the nanowire sample limits the area that can be investigated. Further, we find that the choice of the reference area is also important.

In this work, a best practice routine for strain mapping with S(P)ED including —both experimental design and data analysis have been developed and justified. The relevant codes are included to aid replication and further refinement. We have also applied this routine to other materials and specimen geometries including a strain hardened aluminium alloy to verify that its applicability is more generic. The results obtained in the work are insightful and pave the way for more standardized routines with an ultimate goal of developing a convenient and robust three-dimensional strain mapping workflow applicable to a range of functional and engineering materials systems.

References:

[1] Cooper, D; Denneulin, T; Bernier, N; Béché, A; Rouvière, J. Strain mapping of semiconductor specimens with nm-scale resolution in a transmission electron microscope. *Micron* **2016**, 80, 145-165

[2] Béché, A; Rouvière, J.L; Barnes, J.P; Cooper, D. Strain measurement at the nanoscale: Comparison between convergent beam electron diffraction, nano-beam electron diffraction, high resolution imaging and dark field electron holography. *Ultramicroscopy*, **2013**, 131, 10-23

[3] Dheeraj, D; Patriarche, G; Zhou, H; Hoang, T; Moses, A; Grønberg, S, Helvoort, A; Fimland, B; Weman, H. Growth and Characterization of Wurtzite GaAs Nanowires with Defect-Free Zinc Blende GaAsSb Inserts. *Nanoletters*, **2008**, 8, 4459-4463

[4] Johnstone, D; Crout, P; Nord, M; Laulainen, J; Høgås, S; Opheim, E; Martineau, B; Francis, C; Bergh, T; Prestat, E; Smeets, S; andrew-ross1; Collins, S; Hjorth, I; Mohsen; Furnival, T; Jannis, D; Cautaerts, N; Jacobsen, E; Herzing, A; Poon, T; Ånes, H; Morzy, J; Doherty, T; Iqbal,A; Tomas Ostasevicius, T; mvonlany; Tovey, R (2021). pyxem/pyxem: pyxem 0.13.0. Available at 10.5281/zenodo.4436723